

広島大学学位請求論文

Dynamics Study on Ultraviolet Photodissociation of Aliphatic Amines based on Ammonia Photochemistry

アンモニア光化学に基づく脂肪族アミンの光解離反応動力学研究

2019年

広島大学大学院理学研究科

化学専攻

鬼塚 侑樹

目次

主論文

Dynamics Study on Ultraviolet Photodissociation of Aliphatic Amines based on Ammonia Photochemistry

(アンモニア光化学に基づく脂肪族アミンの光解離動力学研究)

公表論文

- (1) Detection of the Excited-State NH_2 ($\tilde{\text{A}}^2\text{A}_1$) in the Ultraviolet Photodissociation of Methylamine
Yuuki Onitsuka, Katsuyoshi Yamasaki, Hiroki Goto, Hiroshi Kohguchi
J. Phys. Chem. A **120**, 8584 (2016).
- (2) Energy dependence of photodissociation dynamics of trimethylamine over the S_2 and S_1 excited states
Yuuki Onitsuka, Yuki Kadowaki, Atsuya Tamakubo, Katsuyoshi Yamasaki, Hiroshi Kohguchi
Chem. Phys. Lett. **716**, 28 (2019).

参考論文

- (1) Multiple Intersystem Crossing Pathways in Cinnamate-Based UV-B Sunscreens
Kaoru Yamazaki, Yasunori Miyazaki, Yu Harabuchi, Tetsuya Taketsugu, Satoshi Maeda, Yoshiya Inokuchi, Shin-nosuke Kinoshita, Masataka Sumida, Yuuki Onitsuka, Hiroshi Kohguchi, Masahiro Ehara, Takayuki Ebata
J. Phys. Chem. Lett. **7**, 4001 (2016).
- (2) Different photoisomerization routes found in the structural isomers of hydroxy methylcinnamate
Shin-nosuke Kinoshita, Yasunori Miyazaki, Masataka Sumida, Yuuki Onitsuka, Hiroshi Kohguchi, Yoshiya Inokuchi, Nobuyuki Akai, Takafumi Shiraogawa, Masahiro Ehara, Kaoru Yamazaki, Yu Harabuchi, Satoshi Maeda, Tetsuya Taketsugu, Takayuki Ebata
Phys. Chem. Chem. Phys. **20**, 17583 (2018).

主論文

Dynamics Study on Ultraviolet Photodissociation of
Aliphatic Amines based on Ammonia Photochemistry

Yuuki Onitsuka

Department of Chemistry, Graduate School of Science,
Hiroshima University

Acknowledgments

First of all, I am grateful immensely to my supervisor, Professor Hiroshi Kohguchi for enormous advice, guidance and continuous encouragement throughout my studies in the reaction physical chemistry group. He gave me fruitful opportunities to acquire the knowledge and technique not only for reaction dynamics study but also for an electronic circuit design and a machining operation. These knowledge and technique should become the property in my hereafter study. I wish to gratefully acknowledge Professor Katsuyoshi Yamasaki for fruitful advice and discussion. In addition, I would like to thank him also for providing me approval of using his high-sensitive fluorescence apparatus, resulting in a dramatic progress in my study.

I would like to express my gratitude to Professor Takayuki Ebata for pertinent comments and vigorous discussion. In the collaborative research with his laboratory, I could get precious chance of the participation in the big project over other institutions. I am thankful to Professor Misako Aida for her valuable comments and kindly encouragement.

I would like to express my appreciation to all staff of Craftwork Plaza in Hiroshima university for their tremendous assistance in the development and improvement of the experimental apparatus. Finally, I wish to offer my special thanks to all previous and present members of the reaction physical chemistry group for their advice, help, and kindness.

Contents

Chapter 1	General Introduction.....	1
1.1	Molecular and Electronic Structures of Amine	2
1.2	Ammonia Photochemistry	5
1.2.1	Rydberg/Valence Interaction	5
1.2.2	Predissociation.....	9
1.2.3	Electronic Branching.....	11
1.3	Photochemistry of CH ₃ -Substituted NH ₃ Derivatives.....	21
1.3.1	UV Absorption Spectra.....	21
1.3.3	Photochemistry of Trimethylamine	35
1.4	Goal and Outline	42
1.5	Reference.....	44
Chapter 2	Experimental Principle and Methods.....	47
2.1	Experimental Approaches.....	48
2.2	Experimental Principles	52
2.2.1	REMPI Spectroscopy	52
2.2.2	Emission Spectroscopy.....	56
2.2.3	Velocity-Map Imaging.....	59
2.2.4	Analysis of Scattering Distribution	61
2.3	Experimental Apparatus	65
2.3.1	VMI Experiment.....	65
2.3.2	Construction of DUV Laser.....	68
2.3.3	Fluorescence Experiment	70
2.4	Reference.....	72

Chapter 3	Photodissociation Dynamics of Methylamine	73
3.1	Introduction	74
3.2	Experimental Methods	78
3.3	Results	82
3.3.1	REMPI Spectra of the CH ₃ Photofragments	82
3.3.2	Vibrationally State-Resolved Ion-Images of the CH ₃ Products	84
3.3.3	Dispersed Fluorescence Spectra of NH ₂ (\tilde{A}^2A_1)	88
3.3.4	REMPI Spectra of the NH($X^3\Sigma^-$) Photofragments.....	91
3.3.5	Scattering Images of the NH($X^3\Sigma^-$) Products.....	94
3.4	Discussion	97
3.5	Conclusion.....	104
3.6	References	105
Chapter 4	Photodissociation Dynamics of Trimethylamine	107
4.1	Introduction	108
4.2	Experimental and Analysis Methods	113
4.3	Results	116
4.3.1	REMPI Spectra of the CH ₃ Photofragments	116
4.3.2	Dissociation Yields	119
4.3.3	State-Resolved Ion-Images of the CH ₃ Photofragments	121
4.4	Discussion	127
4.4.1	Electronic Dynamics and Dissociation Dynamics	127
4.4.2	Anisotropy of the Scattering Distributions.....	130
4.4.3	Branching of the Product Pathways	132
4.5	Conclusion.....	134
4.6	References	136
Chapter 5	General Conclusion	139

Appendix	Development of LIF Detection System	143
A.1	Introduction	144
A.2	Design of LIF Measurement Cell	150
A.3	Performance Evaluation	152
A.4	LIF Measurement in the CH ₃ NH ₂ Photodissociation	156
A.5	Extension toward Dispersed LIF Measurement	160
A.6	References	161

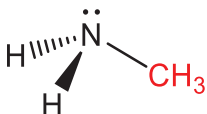
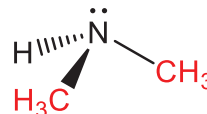
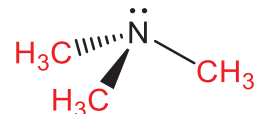
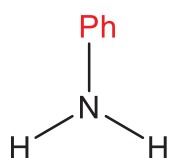
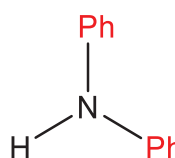
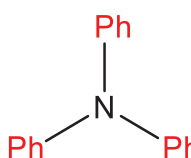
Chapter 1

General Introduction

1.1 Molecular and Electronic Structures of Amine

Amine is the compound that contains a nitrogen atom with lone pair electrons. Amine is a derivative of ammonia (NH_3), and has a $\text{NR}^1\text{R}^2\text{R}^3$ molecular structure, where R^n denotes a substituent. There are numerous amine molecules due to many varieties of R. Amine can be classified as to the kinds of the substituents (R). Aliphatic amine contains only H and alkyl substituents, while aromatic amine has aromatic ring(s) attached to the N atom. Besides these classes, the compounds with the carbonyl group, $\text{R}-\text{CO}-\text{NR}^1\text{R}^2$, are so-called amide. Aliphatic and aromatic amines are further organized into three sub-classes based on the number of R; primary- (R^1NH_2), secondary- ($\text{R}^1\text{R}^2\text{NH}$), and tertiary- ($\text{R}^1\text{R}^2\text{R}^3\text{N}$) amine. The simplest amine in each sub-class is listed in Table 1.1. Aliphatic and aromatic amines are individually characterized by the local molecular structure around the N atom. Aliphatic amine has a tetrahedral structure centered on the N atom due to sp^3 hybridization. Conversely, the structure around the N atom is often nearly planar owing to conjugation of the lone pair on the N atom with the π electrons on the aromatic ring.

Table 1.1 Molecular structure of the simplest aliphatic and aromatic amines in each sub-class. Ph denotes benzyl (C_6H_5) group.

Aliphatic amine		
Primary- (NH_2R^1)	Secondary- (NHR^1R^2)	Tertiary- ($NR^1R^2R^3$)
		
Methylamine CH_3NH_2	Dimethylamine $(CH_3)_2NH$	Trimethylamine $(CH_3)_3N$
Aromatic Amine		
		
Aniline $PhNH_2$	Diphenylamine Ph_2NH	Triphenylamine Ph_3N

Amine is ubiquitous as organic and biological building block and plays the essential role as a Lewis base or hydrogen-bonding donor. The basicity of amine depends on the electronic properties of the substituents; alkyl groups enhance the basicity, whereas aryl groups diminish it. The adjustable nucleophilicity by an appropriate selection of the substituent is useful for organic synthesis. Amine has a distinctive fishy-smell and is also contained substances putrefied by a microbe. Some amines cause a human illness; trimethylaminuria, which is called as fish-odor syndrome,¹ is a disorder where the body is unable to break down trimethylamine. On the other hand, many drugs are designated based

on amine in order to interfere with the action of natural amine neurotransmitters. For example, antihistamine which treats allergies consists of three amine frames.

The electronic structure of aliphatic amine is also similar, as well as the pyramidal molecular geometry. In spectroscopic terms, the first electronic-excited state of aliphatic amine is characterized by the electron promotion from the lone-pair orbital (n_N) to the $3s$ Rydberg orbital of the N atom, and then such excited state is termed $n_N 3s$ state. Reaction dynamics following a photoexcitation, such as photofragmentation and photoisomerization, can be generally understood by nuclear motions on the potential energy surface (PES), which arises from the electrostatic interactions between the electrons and nuclei in the electronic state of interest; therefore, the photochemistry of the aliphatic amine following excitation to the common $n_N 3s$ state has been traditionally expected to be similar to that of NH_3 . The photochemistry of NH_3 had been experimentally and theoretically explored as a benchmark system of amine photochemistry for the last several decades.²⁻¹⁶

1.2 Ammonia Photochemistry

1.2.1 Rydberg/Valence Interaction

Electronically excited states of molecules are classified roughly into Rydberg state and valence state. Molecular orbitals (MO) are expressed by linear combination of atomic orbitals on the basis of the molecular orbital method. The electronic state in which an electron is excited to the MO is called a valence state, such as $n_N\sigma_{N-H}^*$ state, where one of lone-pair electrons (n_N) is excited to anti-bonding orbital (σ_{N-H}^*) of NH_3 . On the other hand, Rydberg state is associated with the electron promotion to an atomic orbital (e.g. n_N3s state of NH_3 as mentioned above). Then, we can consider approximately that the electron in the $3s$ orbital moves around the NH_3^+ ion core, such as an electron of hydrogen atom, leading to the bound n_N3s PES. The photoexcited NH_3 in the n_N3s state, however, dissociates to $\text{NH}_2 + \text{H}$ products due to the adiabatic \tilde{A}^1A_2' PES caused by an interaction between the bound n_N3s Rydberg state and the repulsive $n_N\sigma_{N-H}^*$ valence state.

To understand the interaction, a *diabatic* potential and an *adiabatic* potential are introduced. We consider a two-level system for which the time-independent Schrödinger Equation is as follows:

$$\hat{H}\Psi(\mathbf{r}, \mathbf{R}) = E\Psi(\mathbf{r}, \mathbf{R}) \quad (1.1)$$

$$\hat{H} = \hat{T}_N + \hat{V} \quad (1.2)$$

$$\hat{V} = \begin{pmatrix} V_{11}(\mathbf{R}) & V_{12}(\mathbf{R}) \\ V_{21}(\mathbf{R}) & V_{22}(\mathbf{R}) \end{pmatrix}, \quad (1.3)$$

where $\Psi(\mathbf{r}, \mathbf{R})$ and E denote the eigenfunction and eigenvalue for the full-Hamiltonian operator (\hat{H}), respectively. The \hat{H} is composed of the nuclear kinetic energy term (\hat{T}_N) and the potential matrix (\hat{V}). Here, $\mathbf{R} = (\mathbf{R}_1, \mathbf{R}_2, \dots)$ and $\mathbf{r} = (\mathbf{r}_1, \mathbf{r}_2, \dots)$ is the coordinates of the nuclei and the electrons, respectively. We can express $\Psi(\mathbf{r}, \mathbf{R})$ as an expansion in the product of electronic basis functions ($\phi_i(\mathbf{r}, \mathbf{R})$) and coefficient $\chi_i(\mathbf{R})$ with respect to the i^{th} electronic state:

$$\Psi(\mathbf{r}, \mathbf{R}) = \sum_{i=1}^2 \chi_i(\mathbf{R}) \phi_i(\mathbf{r}; \mathbf{R}). \quad (1.4)$$

Note that $\chi_i(\mathbf{R})$ depends only upon the nuclear coordinates (\mathbf{R}), while $\phi_i(\mathbf{r}, \mathbf{R})$ depends upon the electronic coordinates (\mathbf{r}) and, parametrically, also upon the nuclear coordinates. Then, the matrix elements of \hat{V} in Eq. (1.3) is:

$$V_{ij} = \langle \phi_i(\mathbf{r}; \mathbf{R}) | \hat{H}_e | \phi_j(\mathbf{r}; \mathbf{R}) \rangle, \quad (1.5)$$

where \hat{H}_e is the electronic Hamiltonian operator which includes the electron kinetic energy and the electrostatic interaction terms. When the basis functions, $\phi_i(\mathbf{r}, \mathbf{R})$ and $\phi_j(\mathbf{r}, \mathbf{R})$, have same symmetry, the off-diagonal terms of \hat{V} is non-zero. Adiabatic potential, $\hat{U}(\mathbf{R})$, obtained by diagonalization of \hat{V} matrix:

$$\hat{U} = \begin{pmatrix} U_{11}(\mathbf{R}) & 0 \\ 0 & U_{22}(\mathbf{R}) \end{pmatrix}, \quad (1.6)$$

and then, the eigenfunction for the i^{th} state (ψ_i) is obtained simultaneously. The eigenvalues are:

$$U_{\pm}(\mathbf{R}) = U_{11 \text{ or } 22}(\mathbf{R}) = \frac{V_{11}(\mathbf{R}) + V_{22}(\mathbf{R})}{2} \pm \sqrt{\left(\frac{V_{11}(\mathbf{R}) - V_{22}(\mathbf{R})}{2}\right)^2 + V_{12}^2(\mathbf{R})}, \quad (1.7)$$

where $V_{12}(\mathbf{R})$ and $V_{21}(\mathbf{R})$ is identical each other because of the Hermitian operator \hat{H}_e .

Thus, the electronic Schrödinger Equation for the i^{th} state is driven:

$$\hat{H}_e \psi_i(\mathbf{r}; \mathbf{R}) = U_i(\mathbf{R}) \psi_i(\mathbf{r}; \mathbf{R}). \quad (1.8)$$

Eq. (1.3) is generally called diabatic expression, where the diagonal matrix elements and the off-diagonal ones are named diabatic potential energy and diabatic coupling, respectively. In contrast, Eq. (1.6) is adiabatic expression, and the diagonal terms are adiabatic potential energy. Figure 1.1 describes schematically the adiabatic potential energy curves (PECs) (red solid-line) and the diabatic ones (broken lines) as a function of the N—H bond length ($R_{\text{N-H}}$) of NH_3 . The electronic character is unchanged with respect to $R_{\text{N-H}}$ on the diabatic PECs, while the adiabatic $\tilde{A}^1 A_2''$ PEC exhibits predominantly 3s Rydberg character in the vertical Franck-Condon (FC) region, evolving into significant $\sigma_{\text{N-H}}^*$ valence character at elongated N—H bond distance ($R_{\text{N-H}}$).

Eq. (1.1) is transformed to the nuclear Schrödinger Equation for the i^{th} electronic state by using Eq. (1.4) and (1.7) within Born-Oppenheimer approximation:

$$\hat{H}_N \chi_i(\mathbf{R}) = [\hat{T}_N + U_i(\mathbf{R})] \chi_i(\mathbf{R}) = E \chi_i(\mathbf{R}). \quad (1.9)$$

Motion of the atomic nuclei during chemical reaction is equivalent to solve the nuclear Schrödinger Eq. (1.7) or the corresponding time-dependent equation:

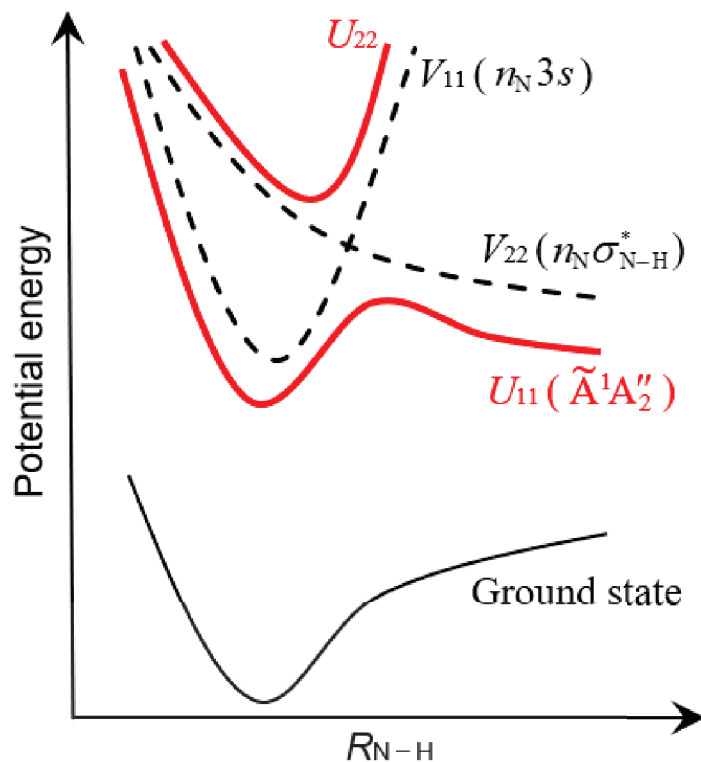


Figure 1.1 Schematic potential energy curves (PECs) of NH_3 as a function of the N–H bond length ($R_{\text{N-H}}$). The diabatic PECs of the $n_{\text{N}}3s$ and $n_{\text{N}}\sigma_{\text{N-H}}^*$ are described by black broken-lines, while the adiabatic PECs obtained by diagonalization of the diabatic potential matrix (\hat{V}) are shown by red solid-lines.

$$i \frac{\partial \chi(\mathbf{R}, t)}{\partial t} = \hat{H}_N \chi_i(\mathbf{R}, t); \quad (1.10)$$

therefore, chemical reaction dynamics is generally understood as nuclear motions on the PES. On the first excited $\tilde{A}^1 A_2''$ PES of NH_3 , a small reaction barrier arising from avoided crossing between two adiabatic potentials controls the reactivity for the N–H bond rupture, and causes predissociation.

1.2.2 Predissociation

Photodissociation dynamics following a photoexcitation is divided into two types: direct photodissociation and predissociation. Direct photodissociation occurs when a molecule is excited to a repulsive surface without any reaction barrier. A molecule photoexcited to a discrete level on a quasi-bound surface, which has a reaction barrier as in the \tilde{A}^1A_2'' PES of NH_3 , will dissociate if the photoexcited molecule has sufficient energy to overcome the barrier. This phenomenon is called predissociation. The lifetime of the predissociative excited state is longer than that in the direct photodissociation. The difference in the excited state-lifetime appears clearly in an absorption spectrum, because a spectral width ($\Delta\omega$) is related to a lifetime of a photoexcited state (Δt) with an uncertainty principle, $\Delta\omega \cdot \Delta t \sim 1$. Figure 1.2 shows the relation between the topology of the excited-state PEC and the corresponding absorption spectrum for HF (Figure 1.2(a))¹⁷ and NH_3 (Figure 1.2(b))¹⁸ which are typical molecules for direct dissociation and predissociation, respectively. The absorption spectrum of HF molecule shows a structureless band, while a vibronic structure is obviously visible in the absorption spectrum of the predissociative NH_3 molecule. The spectral peaks are assigned to the vibronic structure of the $\tilde{X}^1A_1'(v_2'' = 0) \rightarrow \tilde{A}^1A_2''(v_2')$ electronic transition, where v_2 denote a quantum number of the out-of-plane bending mode (v_2 , 874 cm^{-1}).⁵ We can prepare the predissociative molecule in a single vibronic level with narrow spectral width laser beam; therefore, these predissociative molecules are typical examples for state-selective photochemistry such as a

dependence of the photoproduct state-population on the photoinitiated states of parent molecule.

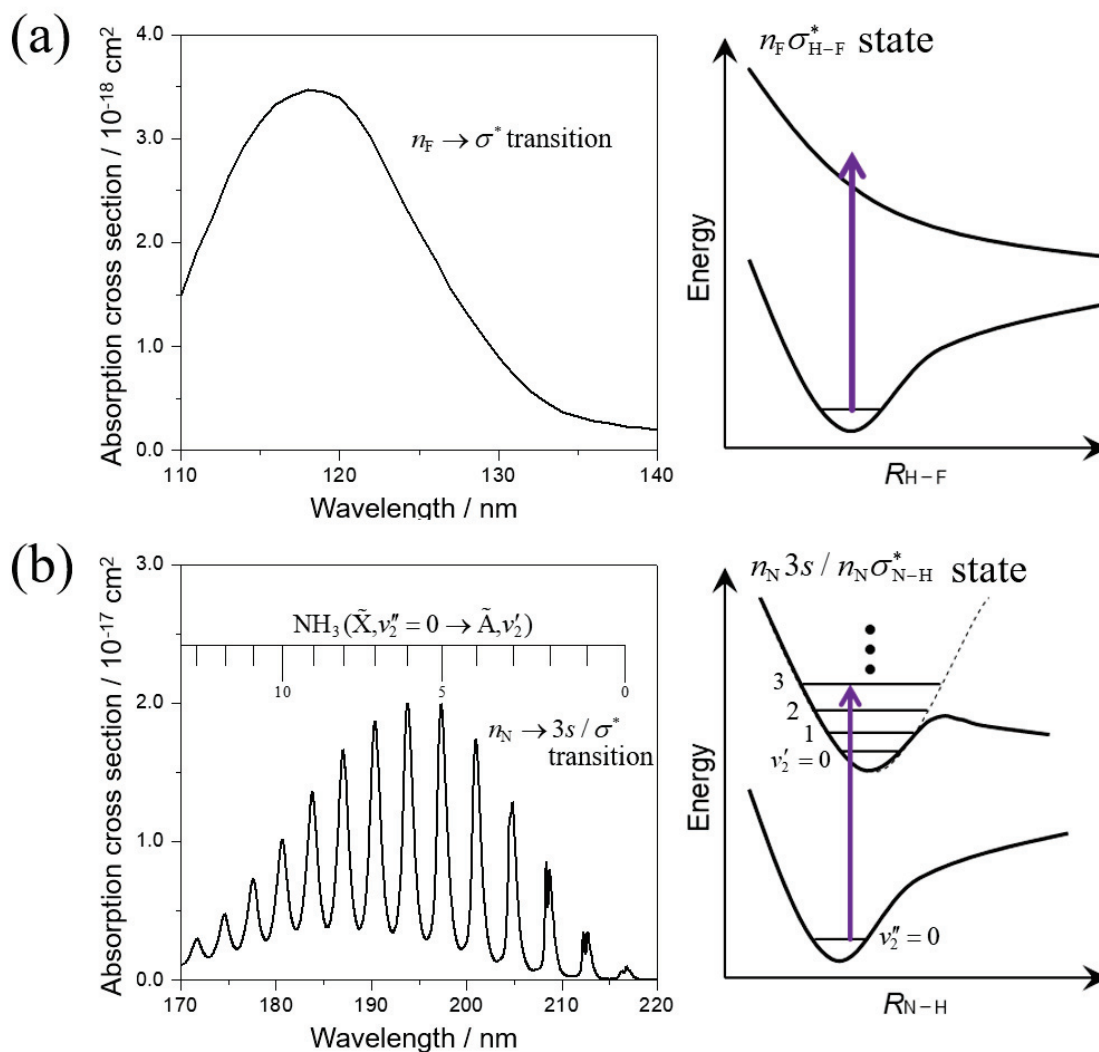


Figure 1.2 Absorption spectra of (a) the direct-dissociative HF molecule and (b) the predissociative NH₃ molecule taken from Refs. 17 and 18, respectively. The inserts display the schematic potential energy curves for each molecule. The spectrum of NH₃ shows clearly vibronic structures whose peaks are assigned to progression in the out-of-plane bending (ν_2) mode. ν_2' and ν_2'' denote quantum numbers of the ν_2 mode in the ground and excited electronic states, respectively.

The long progression in the ν_2 mode in the excited state of NH_3 is a consequence of the pyramidal \rightarrow planar geometrical rearrangement following the $\tilde{X}^1A'_1 \rightarrow \tilde{A}^1A''_2$ photoexcitation, since the NH_3 molecule is pyramidal (C_{3v}) in the $\tilde{X}^1A'_1$ (1A_1) ground state, and is planar (D_{3h}) in the $\tilde{A}^1A''_2$ excited state. The H atom elimination ($\text{NH}_3 + h\nu \rightarrow \text{H} + \text{NH}_2$) proceeds via the small reaction barrier at $R_{\text{N-H}} \approx 1.3 \text{ \AA}$, where the NH_3 electronic character changes drastically from the $3s$ Rydberg to the $\sigma_{\text{N-H}}^*$ valence nature (Figures 1.1 and 1.2(b)). The magnitude of the barrier increases with the out-of-plane bending angle.^{6,7} Ashfold *et al.* revealed experimentally that the predissociation following the vibronic photoexcitation at the $\nu'_2 = 1$ state is slower than that at the $\nu'_2 = 0$ state, and the rate constant increases again with the $\nu'_2 \geq 2$ states. In addition, the predissociation is much slower in deuterated ammonia (ND_3) than in NH_3 , indicating that the N–H (D) bond dissociation on the $\nu'_2 \leq 2$ levels occurs via the quantum tunneling through the barrier on the $\tilde{A}^1A''_2$ surface.

1.2.3 Electronic Branching

Conical Intersection

In addition to the reaction barrier which is located at slightly longer N–H bond ($R_{\text{N-H}} \approx 1.3 \text{ \AA}$) than the equilibrium bond length ($R_{\text{N-H}} \approx 1.0 \text{ \AA}$), the topology of the reaction PES along the N–H bond cleavage coordinate is further complicated by a conical intersection between the adiabatic $\tilde{A}^1A''_2$ and $\tilde{X}^1A'_1$ PESs. Conical intersections between two

adiabatic PESs arises for a polyatomic molecule composed of more than two atoms. When we consider a diatomic molecule which has only one geometric distortion (bond extension or compression), the variable $\mathbf{R} = (\mathbf{R}_1, \mathbf{R}_2, \dots)$ are replaced to a \mathbf{R}_1 in Eq (1.7), resulting in the one-dimensional adiabatic potentials:

$$U_{\pm}(\mathbf{R}_1) = U_{11 \text{ or } 22}(\mathbf{R}_1) = \frac{V_{11}(\mathbf{R}_1) + V_{22}(\mathbf{R}_1)}{2} \pm \sqrt{\left(\frac{V_{11}(\mathbf{R}_1) - V_{22}(\mathbf{R}_1)}{2}\right)^2 + V_{12}^2(\mathbf{R}_1)}. \quad (1.11)$$

Crossing between the two potentials, namely $U_{11}(\mathbf{R}_1) = U_{22}(\mathbf{R}_1)$ in Eq. (1.11), requires that the following simultaneous equations are fulfilled:

$$\begin{aligned} V_{11}(\mathbf{R}_1) - V_{22}(\mathbf{R}_1) &= 0 \\ V_{12}(\mathbf{R}_1) &= 0. \end{aligned} \quad (1.12)$$

The simultaneous equations with a single variable are unsolvable; therefore, the adiabatic-potentials with same symmetry for diatomic molecules cannot cross each other (this well-known result is the *non-crossing rule*).

A triatomic molecule has three (four for a linear molecule) internal degrees of freedom; therefore, the PESs are describe in three-dimensional space. Then, simultaneous Eqs. (1.12):

$$\begin{aligned} V_{11}(\mathbf{R}_1, \mathbf{R}_2, \mathbf{R}_3) - V_{22}(\mathbf{R}_1, \mathbf{R}_2, \mathbf{R}_3) &= 0 \\ V_{12}(\mathbf{R}_1, \mathbf{R}_2, \mathbf{R}_3) &= 0. \end{aligned} \quad (1.13)$$

These equations are solvable, and then two of $\{\mathbf{R}_1, \mathbf{R}_2, \mathbf{R}_3\}$ are given as restriction with regards to the crossing between the adiabatic PESs. When these solutions are $\mathbf{R}_1 = \mathbf{R}_{1c}$ and $\mathbf{R}_2 = \mathbf{R}_{2c}$, the PESs along both \mathbf{R}_1 and \mathbf{R}_2 coordinates cross at single point. One of these specific coordinates (\mathbf{R}_1 and \mathbf{R}_2) is the direction along which the nuclei move in order to bring the two adiabatic states close in energy; it is known as the *tuning* coordinate. Another coordinate is known as the coupling coordinate and corresponds to a motion that reduces the symmetry leading to the avoided crossing.

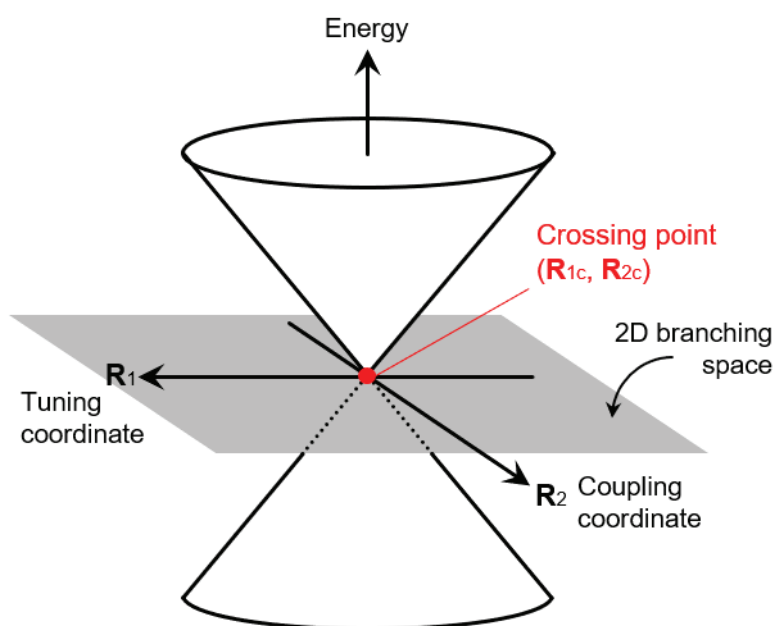


Figure 1.3 Schematic diagram of a conical intersection between two adiabatic PESs (illustrated as the upper and lower cones). Assuming that \mathbf{R}_1 and \mathbf{R}_2 are, respectively, the tuning and coupling coordinates, two adiabatic surfaces can cross only at the single point of $(\mathbf{R}_1, \mathbf{R}_2) = (\mathbf{R}_{1c}, \mathbf{R}_{2c})$ which is the solution of Eq. 1.13.

In case of polyatomic molecules, two of $3N-6$ coordinates, where N is the number of atoms, are also the tuning and coupling coordinates. Along the remaining $3N-8$ coordinates, there will be a $(3N-8)$ -dimensional seam of intersections between the adiabatic PESs because motions along these coordinates can take place without lifting the degeneracy of the two surfaces. The orthogonal tuning and coupling coordinates define what is known as the *branching space* of the intersection.¹⁹ The shape around the intersection region between the two diabats, when plotted in the branching space, is identical with the appearance of two cones facing each other, as illustrated in Figure 1.3, giving rise to the name “*conical intersection*”. Because conical intersections play important roles in chemical reactions, dynamics around conical intersections are subject of much ongoing research in systems ranging from small molecules to large ones such as nucleic acid bases, peptides and proteins.

The \tilde{A}^1A_2' and \tilde{X}^1A_1' PESs of NH_3 (or ND_3) are shown in Figures 1.4 (3-dimensional PESs¹²) and 1.5 (1-dimensional PECs⁷). The tuning and coupling coordinates correspond, respectively, to the N–H bond length ($R_{\text{N-H}}$) and the out-of-plane bending angle (α) which is defined as the angle between a N–H bond and the principle C_3 axis of NH_3 . In Figure 1.5, the adiabatic potential energy curves for the ground and excited electronic states of ND_3 plotted as a function of the N–D distance for various α : $\alpha = 90^\circ$ (planar geometry, solid line), $\alpha = 95^\circ$ (broken line), and $\alpha = 120^\circ$ (dotted line). At the planar ND_3 configuration ($\alpha = 90^\circ$), these diabats cross at $R_{\text{N-D}} \sim 2 \text{ \AA}$. When the planar geometry

is distorted, the adiabats avoid crossing, and then an energy gap between the two states arises. The magnitude of the gap depends considerably on the pyramidal angle. The \tilde{A}^1A_2'' and \tilde{X}^1A_1' PESs are adiabatically correlated to the $\text{NH}_2(\tilde{A}^2A_1) + \text{H}$ and $\text{NH}_2(\tilde{X}^2B_1) + \text{H}$ product pathways in the pyramidal geometry, respectively; therefore dynamics around the conical intersection determines the electronic state of the NH_2 products.

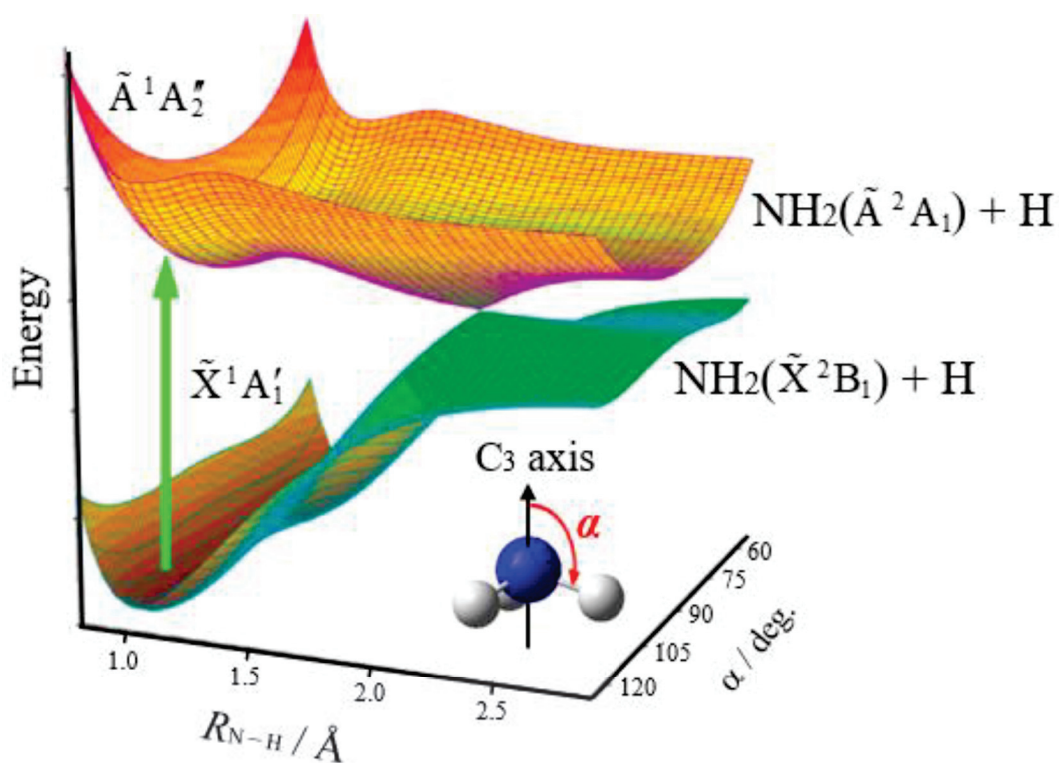


Figure 1.4 3-dimensional adiabatic \tilde{A}^1A_2'' and \tilde{X}^1A_1' PESs of NH_3 as a function of the N—H bond length ($R_{\text{N-H}}$) and the out-of-plane bending angle (α) (after Ref. 12). The unit of $R_{\text{N-H}}$ is revised, and the definition of α is inserted.

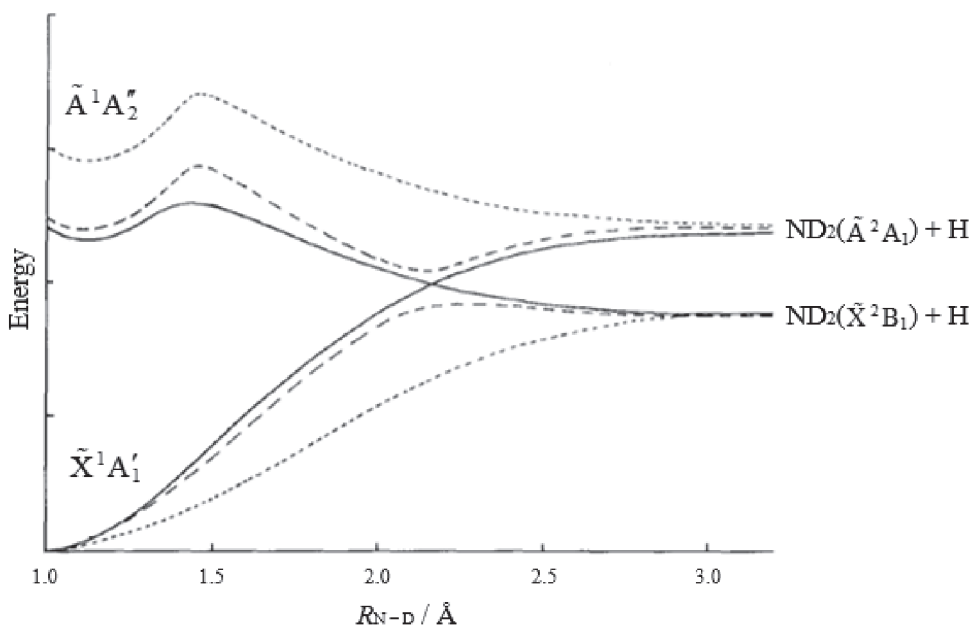


Figure 1.5 Schematic potential energy curves for the \tilde{A}^1A_2'' and \tilde{X}^1A_1' states of ND_3 plotted as a function of $R_{\text{N-D}}$ at various values of α : $\alpha = 90^\circ$ (planar configuration, solid line), 95° (broken line), and 120° (dotted line). The two curves cross only at $\alpha = 90^\circ$. The energy difference between two curves increases with deviation from $\alpha = 90^\circ$. (Adapted from Ref. 7.)

Non-Adiabatic Transition

The large difference in the masses of atomic nuclei and electrons enables their motions to be treated separately in many chemical reactions. Namely, nuclear motions are restricted to occur on a single PES. However, the timescales of electronic and nuclear motions become comparable around conical intersections where two PESs lie closely in energy, and then a *non-adiabatic* transition which is a transition between adiabatic PESs occurs with the nuclear motions. A concept of non-adiabatic transitions around conical intersections is frequently required to explain many photochemical reaction dynamics (e.g. branching mechanism in photodissociation and non-radiative decay in photoisomerization).

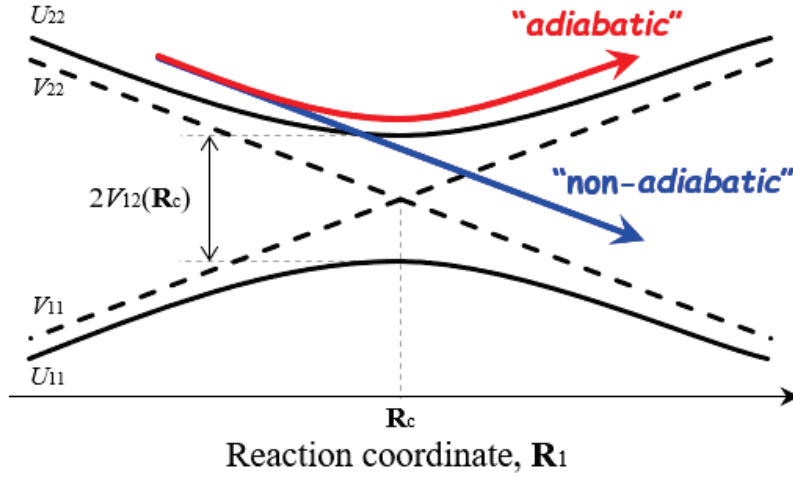


Figure 1.6 1-dimensional potential energy curves; adiabatic (U_{11} and U_{22}) and diabatic (V_{11} and V_{22}) potentials denote by solid and broken lines, respectively. The energy difference of two adiabats at \mathbf{R}_c is $2V_{12}(\mathbf{R}_c)$ obtained from Eq. (1.11). Two types of trajectory are illustrated by arrows; adiabatic (red) and non-adiabatic (blue).

1-dimensional adiabatic and diabatic potential curves around the crossing region for a diatomic molecule are shown in Figure 1.6, where red and blue arrows denote adiabatic and non-adiabatic trajectories, respectively. As mentioned above, two adiabats cannot cross, resulting in the avoided crossing. The energy gap between these adiabats at the special position ($\mathbf{R}_1 = \mathbf{R}_c$), where two diabatic curves cross ($V_{11}(\mathbf{R}_c) = V_{22}(\mathbf{R}_c)$ in Eq. (1.12)), is obtained to be $2V_{12}(\mathbf{R}_c)$ from Eq. (1.11). Massey parameter (ξ),²⁰ which is used as an indicator for adiabatic ($\xi \gg 1$) or non-adiabatic ($\xi \ll 1$) behavior of a molecule around the crossing region, is defined as:

$$\xi = \frac{2\pi V_{12}^2(\mathbf{R}_c)}{\hbar v |\Delta F|}. \quad (1.14)$$

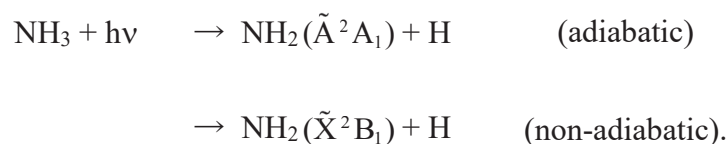
Here, v is the velocity along the reaction coordinate, \mathbf{R}_1 , and $V_{12}(\mathbf{R}_c)$ is the diabatic coupling term which is the off-diagonal element in the potential matrix (\hat{V}). ΔF is the

difference in the gradients of the two diabatic potential curves at the crossing point. The ξ is originally derived in the diabatic basis,²¹ but it can also be obtained in the adiabatic representation using a perturbative approach.²² The non-adiabatic transition probability (P_{NAT}) at \mathbf{R}_c can be estimated using the Landau-Zener formula given below in Eq. (1.15),²³

$$P = \exp(-2\pi\xi) = \exp\left(-\frac{2\pi V_{12}^2(\mathbf{R}_c)}{\hbar v |\Delta F|}\right). \quad (1.15)$$

When the coupling, $V_{12}(\mathbf{R}_c)$, is strong (namely the large energy gap of two adiabats), the system behaves adiabatically, leading to the small P_{NAT} (red arrows in Figure 1.6). The larger velocity, v , results in the non-adiabatic trajectory because of the large P_{NAT} (blue arrow).

The non-adiabatic transition around the conical intersection for the \tilde{A}^1A_2' and \tilde{X}^1A_1' PESs of NH_3 (Figures 1.4 and 1.5), causes the competition of adiabatic and non-adiabatic dissociation pathways to generate the electronically excited $\text{NH}_2(\tilde{A}^2A_1)$ and ground $\text{NH}_2(\tilde{X}^2B_1)$ fragment, respectively:



The conical intersection acts as a dissociation funnel, and the non-adiabatic transition around the conical intersection determines the branching ratio of the product pathways.⁸⁻

^{12,15} On the basis of the one-dimensional manner (Landau-Zener formula, Eq. (1.15)), the

non-adiabatic transition probability (P_{NAT}) is the largest with the planar NH_3 (\tilde{A}^1A_2'') geometry ($\alpha = 90^\circ$). When the photoexcited NH_3 (\tilde{A}^1A_2'') approaches the conical intersection with the planar configuration, the non-adiabatic pathway to produce the NH_2 (\tilde{X}^2B_1) radical is favorable. In their pioneering work, Ashfold *et al.*⁸⁻¹⁰ have studied the energy partitioning among the different photoinitiated vibronic-bands of NH_3 (2_0^v , $v' = 0-6$) using H atom photofragment translational spectroscopy. They found the dependence of the branching ratio between the adiabatic and non-adiabatic channels on the excitation energy, reaching values as large as $\sim 30\%$ following dissociation from the $v'_2 = 6$ level. In addition, the nascent NH_2 fragments are preferentially produced in rotationally excited states ($N \sim K_a$), and the degree of NH_2 rotational excitation shows alternation: those fragments produced after the excitations to $v'_2 = \text{even}$ states show a propensity for low rotational states, while those related to odd excitations show rotationally inverted distributions. The preferential a -axis rotation of NH_2 photoproducts and the rotational population-dependence on the photoinitiated out-of-plane bending mode of NH_3 are interpreted with dynamics around the conical intersection. The odd 2_0^1 and 2_0^3 wavefunctions show a node at planar configuration ($\alpha = 90^\circ$), preferring non-adiabatic channel. The a -axis rotational excitation originates from the rotational torque applied to the recoiling fragments imposed by out-of-plane motions of NH_3 . At non-planar ($\alpha \neq 90^\circ$) geometries, two \tilde{A}^1A_2'' and \tilde{X}^1A_1' adiabats cannot cross each other, leading to an avoided crossing as seen in Figure 1.5. The non-planar NH_3 travels through regions apart from the crossing point before dissociation to ground state

product. The non-adiabatic transition probability around the conical intersection is sensitive to the planarity of the dissociating NH_3 . NH_3 has been also regard as a benchmark molecule for studying influence of a nonadiabatic dynamics around a conical intersection on photochemical reaction dynamics.

1.3 Photochemistry of CH₃-Substituted NH₃ Derivatives

1.3.1 UV Absorption Spectra

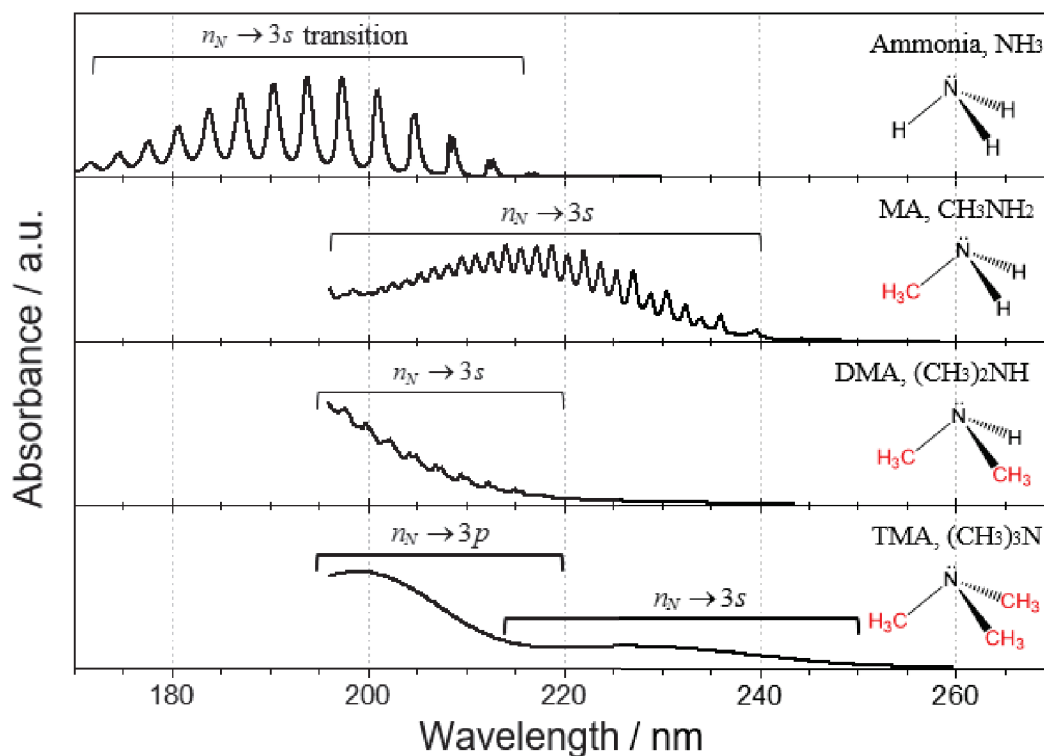


Figure 1.7 Ultraviolet absorption spectra of NH₃ and its derivatives: from the top, ammonia (NH₃), methylamine (MA, CH₃NH₂), dimethylamine (DMA, (CH₃)₂NH), and trimethylamine (TMA, (CH₃)₃N). The first absorption bands of these derivatives are assigned to $n_N \rightarrow 3s$ electronic transition by analogy with NH₃. The second absorption band of TMA peaked at 200 nm corresponds to $n_N \rightarrow 3p$ transition.

Methyl (CH₃) group is the simplest aliphatic substituent and is often regarded to an equivalent substituent with H atom in terms of photochemistry due to the absence of additional chromophores such as a benzyl or allyl group, and a hetero atom. Substitution(s) of H-atom to CH₃ groups in NH₃ molecule, however, is seen to provide a difference on photochemistry. UV absorption spectra of NH₃¹⁸ and its CH₃-substituted derivatives,

methylamine (CH_3NH_2),²⁴ dimethylamine (DMA, $(\text{CH}_3)_2\text{NH}$)²⁵ and trimethylamine (TMA, $\text{N}(\text{CH}_3)_3$),²⁵ are shown in Figures 1.7. The vibronic structure of these spectra fades systematically across the series from ammonia to TMA. The spectrum of TMA is structureless in reminiscent of direct dissociation because of the uncertainty principle for energy and time ($\Delta\omega \cdot \Delta t \sim 1$); therefore, the CH_3 -substitution clearly influences the PES structure of the electronically excited state.

The equilibrium structure of CH_3NH_2 , which is the simplest NH_3 -derivative, in the $\tilde{\text{X}}$ state is pyramidal about the N atom, while that in the $\tilde{\text{A}}$ state is planar (henceforth termed planar geometry).²⁶⁻²⁹ Kassab *et al.* found the metastable *cisoid* geometry in the $\tilde{\text{A}}$ state by *ab initio* calculation, where two N–H bonds and one of C–H bonds are in the same plane.²⁹ The equilibrium geometries in the electronically ground and excited states, and the *cisoid* geometry are shown in Figure 1.8. Morokuma *et al.* found theoretically a very small barrier (~ 0.2 kJ/mol) to rotation between the planar and *cisoid* geometry.^{27,28} The vibronic structure in the absorption spectrum, which is similar to that of NH_3 as seen in Figure 1.7, was assigned to two vibrations: the CH_3 rocking (ν_7 , 1008 cm^{-1}) and NH_2 wagging (ν_9 , 636 cm^{-1}) modes whose schematic motions are illustrated in Figure 1.8.²⁶ The spectral assignment is shown in Figure 1.9.

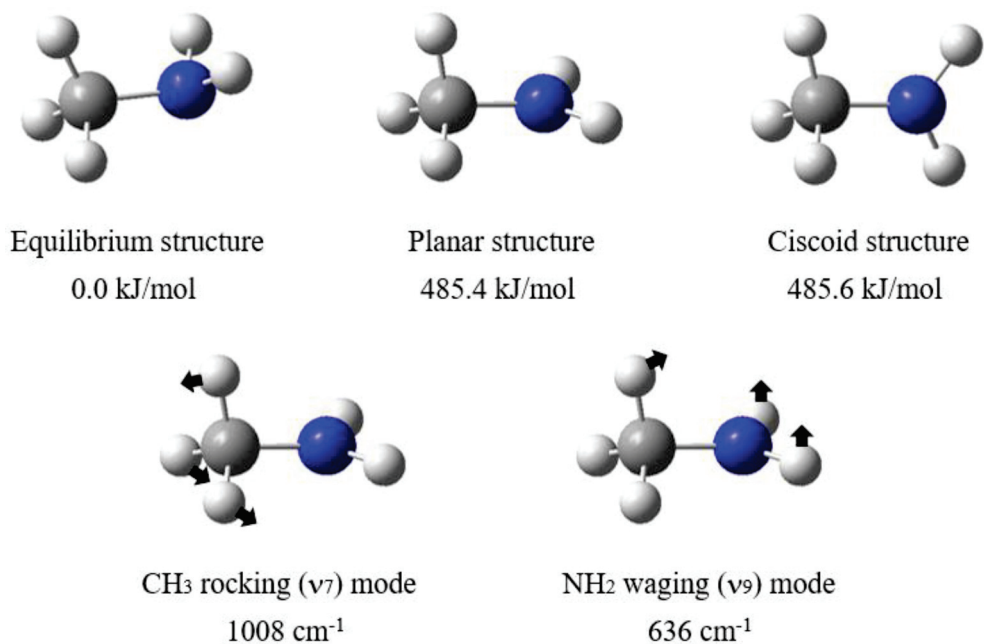


Figure 1.8 Geometries of CH₃NH₂ corresponding to ground state equilibrium, planar excited state equilibrium, and cisoid geometry. The geometrical parameters and the relative energies are quoted from Ref. 24. The normal mode descriptions for ν_7 and ν_9 vibrations are illustrated by the cartoons.

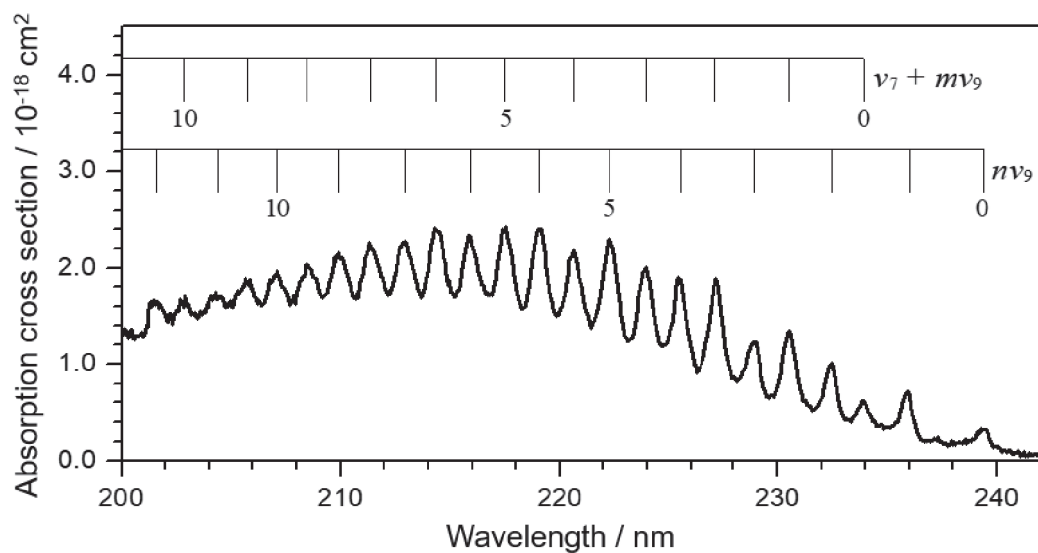


Figure 1.9 UV absorption spectrum of CH₃NH₂. Each peak is assigned to the NH₂ wagging (ν_9) progression band and its combination band with the CH₃ rocking mode (ν_7). m and n indicate quantum numbers of ν_9 mode. The schematic vibrational motions for the ν_7 and ν_9 modes are illustrated in Figure 1.8.

In dimethylamine (DMA, $(\text{CH}_3)_2\text{NH}$), the weakly appeared vibronic structure is unassigned due to the limited available data relating to the spectroscopy. Theoretical study by Kassab *et al.*, however, assigned the first absorption band to the $n_{\text{N}} \rightarrow 3s$ photoabsorption by analogy of NH_3 , and predicted a similar photochemistry to CH_3NH_2 following the $n_{\text{N}} \rightarrow 3s$ photoexcitation.³ Trimethylamine (TMA, $(\text{CH}_3)_3\text{N}$), which is tri-substituted NH_3 derivatives, shows the clear difference in the absorption band from the other three species as seen in Figure 1.7: the structureless first-absorption band and two unseparated broad bands. The first absorption band peaked at ~ 230 nm was assigned to the $n_{\text{N}} \rightarrow 3s$ electronic excitation as in the series from NH_3 to DMA, and the second one was attributed to the $n_{\text{N}} \rightarrow 3p$ photoexcitation. These two absorption bands overlap partially at ~ 215 nm, indicating that TMA has the energetically closer $n_{\text{N}}3p$ state to the $n_{\text{N}}3s$ than the other NH_3 derivatives. The common bands corresponding to $n_{\text{N}} \rightarrow 3s$ transition show a systematic red-shift except DMA. There is a tendency that the CH_3 -substitutions make the energy of the $n_{\text{N}}3s$ state low.

1.3.2 Photochemistry of Methylamine

CH_3NH_2 which is the simplest CH_3 -substituted NH_3 shows a partially structured absorption band associated with $n_{\text{N}} \rightarrow 3s$ transition, and has two types of σ -bond involving the nitrogen atom ($\text{N}-\text{H}$ and $\text{N}-\text{C}$). In 1963, Michael and Noyes found four major pathways (1)–(4) following the broad-band excitation in the 194–244 nm and determined the quantum yields for each pathways (1)–(4) to be 75 %, ~7.5 %, < 5 %, and < 10 %, respectively.³⁰



A subsequent study with photofragment translational spectroscopy detected photoproducts generated in these reaction channels (1)–(4), and concluded that the major channel is $\text{N}-\text{H}$ bond dissociation while the $\text{N}-\text{C}$ and $\text{C}-\text{H}$ bond dissociation channels are also significant.³¹ On the other hand, Ashfold *et al.*, through H-atom Rydberg-tagged high-resolution translational spectroscopy, had reached a conclusion that the $\text{C}-\text{H}$ bond breakage practically does not occur. Several theoretical studies for the $\text{N}-\text{H}$ and $\text{N}-\text{C}$ bond-dissociations showed many parallels with the $\text{N}-\text{H}$ bond dissociation of NH_3 .^{28,29} The small barriers along both reaction coordinates arising from an avoided crossing between $n_{\text{N}}3s$ state and $n_{\text{N}}\sigma_{\text{N}-\text{H or N}-\text{C}}^*$ state are located near FC region, and both the $n_{\text{N}}\sigma_{\text{N}-\text{H}}^*$ and

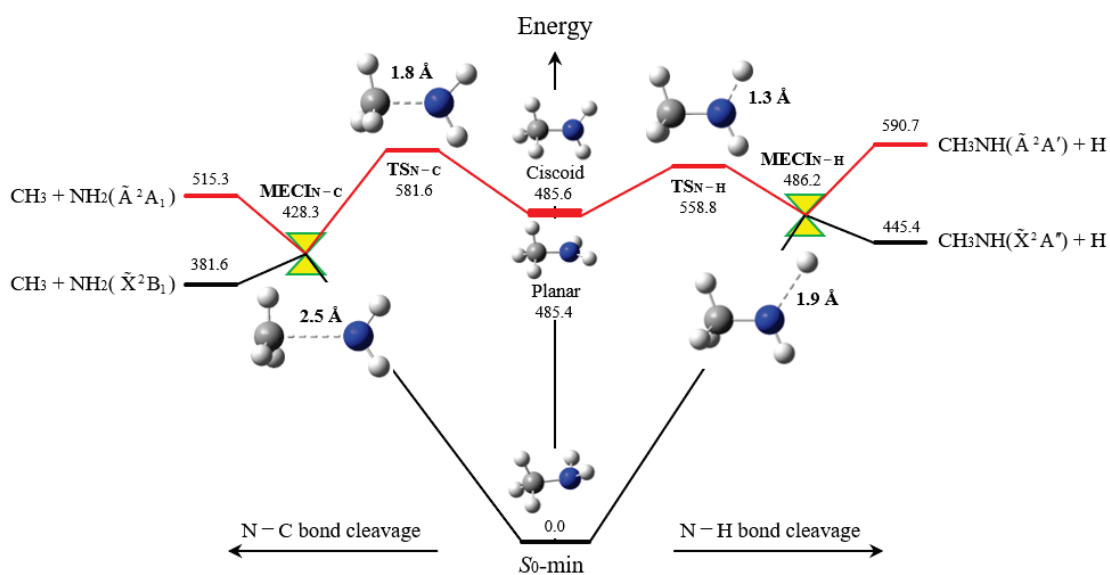


Figure 1.10 Local minimums, transition states (TS), and minimum energy conical intersection (MECI) between the methylamine S_1 and S_0 states along N – H (right) and N – C (left) bond dissociation coordinates. The molecular geometries and the corresponding energies are cited from Ref.24. The geometries and energy values at the corresponding level are also shown. The bond represented by broken line corresponds to the dissociating bond.

$n_N\sigma_{N-C}^*$ states interact electronically with the ground state to form conical intersections around the exit region. In both the N – H bond and N – C bond fission channels, the $3s\sigma_{N-H\text{ or }N-C}^*$ (henceforth termed S_1 state) and ground S_0 states are adiabatically correlated to the pathway with the electronically excited products ($H + CH_3NH(\tilde{A}^2A')$, $CH_3 + NH_2(\tilde{A}^2A_1)$) and the pathway with the ground state product ($H + CH_3NH(\tilde{X}^2A'')$, $CH_3 + NH_2(\tilde{X}^2B_1)$) at nonplanar geometries, respectively. The local minimums, transition states (TS), and minimum energy conical intersections (MECI) between the S_1 and S_0 PESs along both N – H and N – C bond cleavage directions which were explored theoretically by Xiao *et*

*al.*²⁷ are shown in Figure 1.10. Thus, the PES topology of CH₃NH₂ along the N–H and N–C bond-dissociation coordinates resembles that of NH₃; therefore, a similar argument to the NH₃ photodissociation has been presented for both bond-dissociation dynamics of CH₃NH₂. The calculated reaction barrier in N–C bond fission on the excited state surface was 581.6 kJ/mol which was somewhat larger than that in N–H bond fission (558.8 kJ/mol)²⁷ as seen in Figure 1.10. This energy difference has been considered as one of reasons for the predominance of the N–H bond dissociation channel following UV excitation of CH₃NH₂.

N–H Bond Fission Channel

The N–H bond dissociation channel with the largest dissociation yield has been widely studied by various groups.³²⁻³⁹ The resonantly enhanced multiphoton ionization (REMPI) spectra of CH₃NH₂ and CH₃ND₂ measured by Beak *et al.* showed the huge NH/ND isotope effect on the spectral width.³²⁻³⁴ The excited state lifetime of CH₃NH₂ at the zero-point energy level of the *S*₁ state was estimated to be ~ 0.3 ps from the linewidth, which is about 20 times shorter than that of CH₃ND₂ (~8 ps). They interpreted the lifetime as the N–H bond dissociation lifetime, because the linewidth was insensitive to the H/D substitution of the CH₃ moiety (CH₃NH₂ → CD₃NH₂). They concluded that the N–H bond rupture of CH₃NH₂ at the zero-point energy level occurs via a quantum tunneling through the small

barrier near FC region, resulting in the huge isotope effect in the excited state lifetime of CH_3NH_2 and CH_3ND_2 .

The dissociative trajectory beyond the reaction barrier proceeds on the repulsive surface where the $n_{\text{N}}\sigma_{\text{N-H}}^*$ state is predominant rather than the $n_{\text{N}}3s$ Rydberg state, and then encounters a conical intersection located at the longer N–H distance ($\text{CI}_{\text{N-H}}$).²⁷ The $\text{CI}_{\text{N-H}}$ plays an essential role in the bifurcation to $\text{H} + \text{CH}_3\text{NH}(\tilde{\text{A}}^2\text{A}')$ and $\text{H} + \text{CH}_3\text{NH}(\tilde{\text{X}}^2\text{A}'')$ pathways. The H fragment total kinetic energy distributions were obtained in the photolysis wavelength of 219–240 nm whose photon energies are insufficient to access energetically higher $\text{H} + \text{CH}_3\text{NH}(\tilde{\text{A}}^2\text{A}')$ product pathway (calculated wavelength threshold of 210 nm).^{36,39} The kinetic energy distributions were, however, two distinct bimodal distribution. The distribution for the higher energy component was sharp, indicating that the N–H bond rupture is enough fast to leave only the small energy to the internal degrees of freedom of $\text{CH}_3\text{NH}(\tilde{\text{X}}^2\text{A}'')$. On the other hand, the lower energy component showed the Boltzmann distribution, suggesting that the internal energy of the $\text{CH}_3\text{NH}(\tilde{\text{X}}^2\text{A}'')$ counter-product is randomized. The source for the slow H fragment was proposed to be the vibrationally hot CH_3NH_2 in the S_0 state generated through the non-adiabatic transition around the $\text{CI}_{\text{N-H}}$. Since the $\text{CH}_3\text{NH}(\tilde{\text{A}}^2\text{A}') + \text{H}$ pathway is not energetically accessible in the wavelength region of 219–240 nm, the adiabatic potential of the $\tilde{\text{A}}$ state is bounced off the potential wall on the $\text{H} + \text{CH}_3\text{NH}(\tilde{\text{A}}^2\text{A}')$ product side, leaking into the rovibrationally hot ground

state. The hot CH_3NH_2 on the S_0 surface dissociates finally to generate the $\text{H} + \text{CH}_3\text{NH}$ (\tilde{X}^2A'') products with the statistic energy-distribution for all degrees of freedom.

Reed *et al.* employed the similar experiment in the shorter wavelength than 210 nm which is a long-wavelength threshold for dissociation to the $\text{H} + \text{CH}_3\text{NH}$ (\tilde{A}^2A') products.³⁸ In addition to the two components attributed to the $\text{H} + \text{CH}_3\text{NH}$ (\tilde{X}^2A'') pathways, they found third component with the narrow energy distribution located in the extremely high energy region. This component was assigned to the $\text{H} + \text{CH}_3\text{NH}$ (\tilde{A}^2A') pathway. Thus, if the photon energy is sufficiently high, the $\text{N}-\text{H}$ bond cleavage produces both electronically excited and ground CH_3NH products as a result of the adiabatic/non-adiabatic dynamics around the exit $\text{CI}_{\text{N}-\text{H}}$ as in NH_3 photochemistry.

N-C Bond Fission Channel

The S_1 PES along the $\text{N}-\text{C}$ bond cleavage coordinate is also characterized by a small barrier at an elongated $\text{N}-\text{C}$ bond length, and another conical intersection ($\text{CI}_{\text{N}-\text{C}}$) at an further elongated $R_{\text{N}-\text{C}}$, as same as that along the $\text{N}-\text{H}$ dissociation coordinate.²⁷ A pioneering work for the $\text{N}-\text{C}$ bond dissociation dynamics is the measurements of the center-of-mass translational energy distribution with photofragment translational spectroscopy at 222 nm by Waschewsky *et al.*³¹ The translational energy distribution showed that more than 90 % of the total available energy (206 kJ/mol) are partitioned into the internal energy of products. The highest kinetic energy of this distribution was near 73

kJ/mol which corresponds to the energetic limit (133 kJ/mol) for generation of the NH₂ counter-product in the \tilde{A}^2A_1 state, implying that the N–C bond fission generates exclusively the electronically excited NH₂ photofragment. On the basis of NH₃, the excited surface of CH₃NH₂ correlates with ground state NH₂ (\tilde{X}^2B_1) only at the cisoid geometry where the NH₃-frame is planar. Any deviation from the planar NH₃-frame removes the symmetry restriction, and then the excited surface correlates adiabatically with electronically excited NH₂ (\tilde{A}^2A_1) product. Because the NH₂ wagging mode (ν_9), which is one of progressions in the vibronic structure of the UV absorption spectrum, is considerably excited during photodissociation, the N–C dissociative trajectory passes adiabatically the region of the exit CI_{N-C} where the upper and lower adiabats are widely split.

Thomas *et al.* applied resonantly enhanced multiphoton ionization (REMPI) spectroscopy to the CH₃ photoproduct at various wavelengths of 222–240 nm.⁴⁰ The vibrational structure in the REMPI spectra was assigned to the $3\nu_3'$ band sequence up to $\nu_3 = 3$, indicating the internal excitation of the degenerate C–H stretch mode (ν_3 , 3161 cm⁻¹) of the CH₃ fragment. The vibrational state-distributions of the CH₃ product for various photolysis wavelengths peak in the vibrationless level and decrease monotonically with the ν_3 excitation. These distributions are independent of the initially selected vibronic state of CH₃NH₂. The generation of the vibrationally excited CH₃ radical up to $\nu_3 = 3$ is incompatible with simultaneous production of the electronically excited NH₂ (\tilde{A}^2A_1) fragment in the wavelength region of 222–240 nm based on the energetic consideration. They proposed that

the N–C bond dissociation occurs on the S_0 surface to produce the vibrationally excited $\text{CH}_3(\nu_3)$ and the electronically ground $\text{NH}_2(\tilde{X}^2\text{B}_1)$. In this proposed dissociative trajectory, the N–H bond is first elongated following UV absorption, and then the populations on the S_0 surface is caused by the internal conversion around the exit $\text{CI}_{\text{N-H}}$. The internally hot CH_3NH_2 in the S_0 state leads to only the $\text{CH}_3(\nu_3 = 0-3) + \text{NH}_2(\tilde{X}^2\text{B}_1)$ product pathway in the photoexcitation wavelength-region of 222–240 nm.

Because the electronic state of the NH_2 fragment in the photodissociation of CH_3NH_2 remains controversial, the non-adiabatic dynamics around the exit $\text{CI}_{\text{N-C}}$ in the N–C bond cleavage channels cannot be compared with that in the N–H bond dissociation channels of NH_3 and CH_3NH_2 . The determination of the electronic state of the nascent NH_2 photoproduct is required to discuss amine photochemistry in terms of the difference in the N–H and N–C bonds. Although application of laser spectroscopy to the NH_2 radical is essentially a definitive method to identify the electronic state, direct application of laser detection to electronically excited species is generally not easy.

NH(X³Σ⁻) Production Channel

Recently, a new pathway to produce NH(X³Σ⁻) + CH₄ fragments following the S₁–S₀ photoexcitation of CH₃NH₂ was proposed experimentally by Thomas *et al.*⁴¹ This interesting pathway was explained by a so-called roaming mechanism including the triplet surface (T₁). Roaming dynamics was first conclusively identified in combined experimental and theoretical work on formaldehyde (HCHO) photodissociation.^{42,43} This mechanism in the HCHO dissociation provides an alternative route to the molecular products, H₂ + CO, that bypasses the conventional skewed transition state on the S₀ surface. Instead, the dissociation to the radical products, H + HCO, is frustrated, resulting in extended excursions at long-range prior to the H–C bond cleavage. One of H atoms nearly detaching via the H + HCO channel meanders in the broad attractive space of the H + HCO surface, far from the reaction path, until it abstracts another H atom. This long-range intramolecular abstraction produces the vibrationally hot H₂ and rotationally cold CO fragments, in marked contrast to the product state-distribution arising from dissociation via the conventional transition state. This behavior has been also recognized in the photolysis of acetaldehyde (CH₃CHO + hv → CH₄ + CO)⁴⁴ and in the atmospherically important nitrate radical (NO₃ + hv → NO + O₂).^{45,46} The Roaming dynamics are, therefore, not restricted to small molecules such as HCHO.

Thomas *et al.* observed, following the photoexcitation of CH₃NH₂ at 222 and 240 nm, a rotationally structured band at mass-to-charge (m/z) ratio of 15.⁴¹ This spectral feature

was assigned to the $D^3\Pi-X^3\Sigma^-(0,0)$ band by comparison with spectral simulation. The rotational temperature of the nascent $NH(X^3\Sigma^-, v=0)$ was determined $\sim 700-800$ K. In contrast to the mildly rotational excitation, the vibrational state is cold; the $NH(X^3\Sigma^-)$ product is populated only in $v=0$ state, irrespective of the photoinitiated states. Although the NH molecule, whose electronic ground state is triplet state ($^3\Sigma^-$), has the metastable singlet state ($^1\Delta$) which lies only $12,500\text{ cm}^{-1}$ above the $X^3\Sigma^-$ state, no transitions originating in the $a^1\Delta$ state was identified. Dynamics of the $NH(X^3\Sigma^-)$ production was interpreted as a result of the intersystem crossing (ISC) in a long-range region. The exit Cl_N-H provides a convenient means for the internal conversion and funneling population back to the S_0 surface as discussed above. Thomas *et al.* proposed that roaming in the long-range region of the S_0 surface provides ample opportunity for ISC to the T_1 surface, on which the reaction to produce $CH_4 + NH(X^3\Sigma^-)$ fragments occurs finally. Xiao *et al.* carried out comprehensive calculations for photodissociation pathways of CH_3NH_2 including the S_0 , S_1 , and T_1 surfaces.²⁷ They found the potential crossing between the S_0 and T_1 states, and the transition state (TS) on T_1 surface for the intramolecular H atom transfer from the NH_2 moiety to the CH_3 group. The molecular structures and the relative energies at the corresponding local minimum and TS are described in Figure 1.11. The dynamics proposed by Xiao *et al.* is consistent with that suggested experimentally by Thomas *et al.*⁴¹

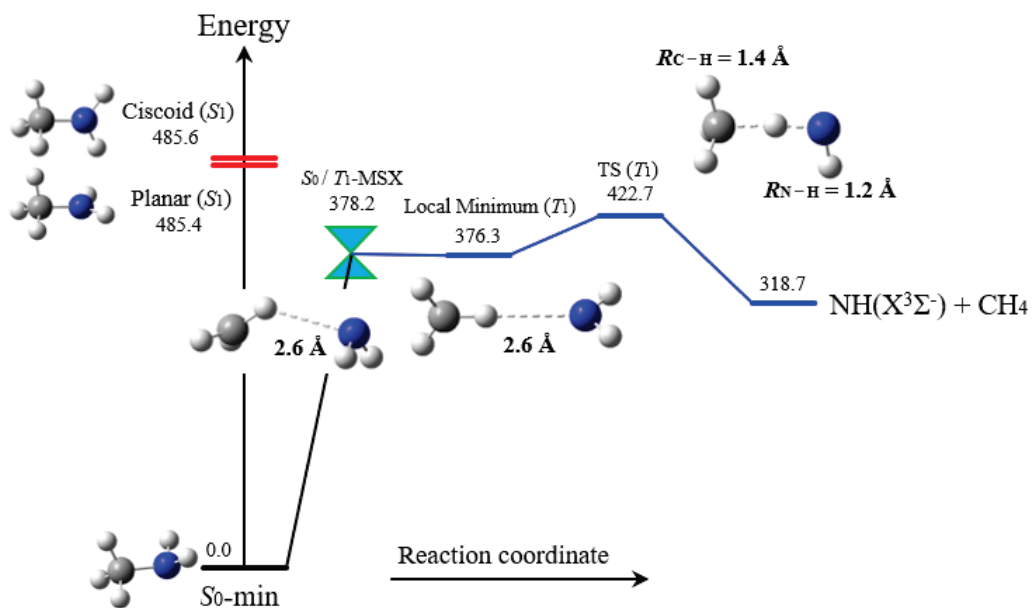
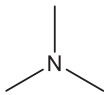
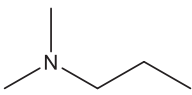
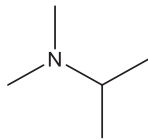
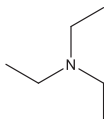
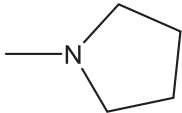
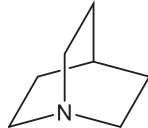


Figure 1.11 Local minimum, transition state (TS), and minimum on the seam of crossing (MSX) between singlet (S_0) and triplet (T_1) states reported by Xiao *et al.* in Ref. 24. The corresponding molecular structures and relative energies (kJ/mol) at these positions are shown. For comparison, the equilibrium structures on the S_1 and S_0 surfaces and the cisoid geometry are also illustrated.

1.3.3 Photochemistry of Trimethylamine

TMA where all H-atoms of NH_3 are substituted by CH_3 groups has only $\sigma_{\text{N-C}}$ bonds; therefore, only the N–C bond cleavage channel is available in the photodissociation of TMA. TMA is also the simplest tertiary aliphatic amines (TAAs), and several examples of TAAs are displayed in Table 1.2. The UV absorption spectra of these TAAs shown in Figure 1.12 are characterized by structureless and two unseparated broad bands, where the strong and weak bands are traditionally assigned to the $S_2(3p)\text{--}S_0$ and $S_1(3s)\text{--}S_0$ transitions, respectively. Regardless of the same $S_1(3s)\text{--}S_0$ transition for both TAAs and NH_3 -derivatives, the $S_1(3s)$ photochemistry of TAAs is significantly different from that of NH_3 and CH_3NH_2 : the $S_1(3s)$ state of TAAs is generally characterized by a highly fluorescent property. The fluorescence quantum yields (Φ_{flu}) of TAAs are close to unity at the longer excitation wavelength, and significantly decrease down to $\Phi_{\text{flu}} = 0$ as the excitation wavelength decreases.⁴⁷⁻⁵⁰

Table 1.2 Structures of several TAA molecules. Note that all TAAs are pyramidal around the N atom.

Trimethylamine (TMA)	<i>N,N</i> -dimethylpropylamine (DMPA)	<i>N,N</i> -dimethylisopropylamine (DMIPA)
		
Triethylamine (TEA)	<i>N</i> -methylpyrrolidine (Mpyr)	1-azabicyclo[2,2,2]octane (ABCO)
		

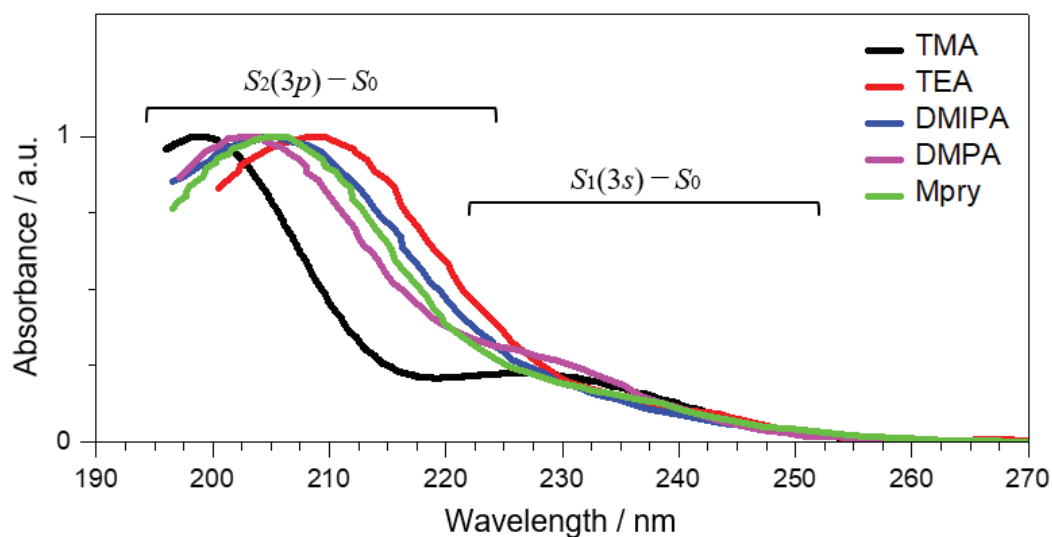


Figure 1.12 Absorption spectra of several TAA molecules: trimethylamine (TMA), triethylamine (TEA), *N,N*-dimethylisopropylamine (DMIPA), *N,N*-dimethylpropylamine (DMPA), and *N*-methylpyrrolidine (Mpyr) whose molecular structures are shown in Table 1.2. All spectra show the structureless and unseparated absorption bands which are assigned to the $S_2(3p)-S_0$ and $S_1(3s)-S_0$ transitions in ascending order of the wavelength.

Internal conversion between the $3s$ and $3p$ Rydberg states is a common character of the $S_2(3p)$ photochemistry of multifarious TAAs from a small tri-substituted amine such as TMA to a large such as azabicyclo[2,2,2]octane (ABCO) and *N*-methylpyrrolidine (Mpyr). Time-resolved photoelectron spectroscopy were applied to these TAAs by several groups.⁵¹⁻⁵⁵ For all these TAAs systems, two distinct dynamical timescales were observed following the excitation at 200 nm corresponding to the peak of the $S_2(3p)-S_0$ absorption band: “ultrafast” (in sub-picosecond order) component and a long-lived one. In the case of Mpyr, the initial excitation predominantly populates the lowest member of the $3p$ Rydberg manifold ($3p_y$ state), and then the photoexcited Mpyr undergoes internal conversion directly to the $3s$ state with an exponential decay time of 400 fs. In contrast, for *N,N*-

dimethylisopropylamine (DMIPA) and *N,N*-dimethylpropylamine (DMPA), a slight energy-shift was observed in the photoelectron spectra associated with ionization from the $3p$ manifold. As the optically bright $3p$ state with the highest oscillator strength sits energetically in the middle of the manifold for DMIPA ($3p_z$) and DMPA ($3p_y$), the shift is ascribed to the inter-manifold electronic relaxation with ~ 100 – 300 fs prior to the internal conversion to the $S_1(3s)$ state (~ 500 – 600 fs).

Theoretical calculations for the excited PES of DMIPA and ABCO by Townsend *et al.* demonstrated a new propensity for the electronic interaction between the $n_N 3p$ Rydberg state and valence $n_N \sigma_{N-C}^*$ state.^{52,54} The $n_N \sigma_{N-C}^*$ state of CH_3NH_2 couples to the $n_N 3s$ Rydberg state, resulting in the predissociative $S_1(3s / \sigma_{N-C}^*)$ PES as in NH_3 , while for DMIPA and ABCO, the $n_N \sigma_{N-C}^*$ state and one of the $3p$ manifold interacts to form the quasi-bound $S_2(3p / \sigma_{N-C}^*)$ surface which is essentially identical to the $S_1(3s / \sigma_{N-H \text{ or } N-C}^*)$ PES of NH_3 and CH_3NH_2 . The $S_1(3s)$ surfaces of DMIPA and ABCO are purely bound and crosses with the dissociative part of the $S_2(3p / \sigma_{N-C}^*)$. The calculated potential energy curves along the N–C bond extension for DMIPA are illustrated in Figure 1.13. Townsend *et al.* proposed that TAAs in the $S_1(3s)$ state prepared by the $S_2 \rightarrow S_1$ internal conversion dissociate on the repulsive part of the $S_2(3p / \sigma_{N-C}^*)$ state through the crossing of the $S_2(3p / \sigma_{N-C}^*)$ and $S_1(3s)$ states.⁵²⁻⁵⁴

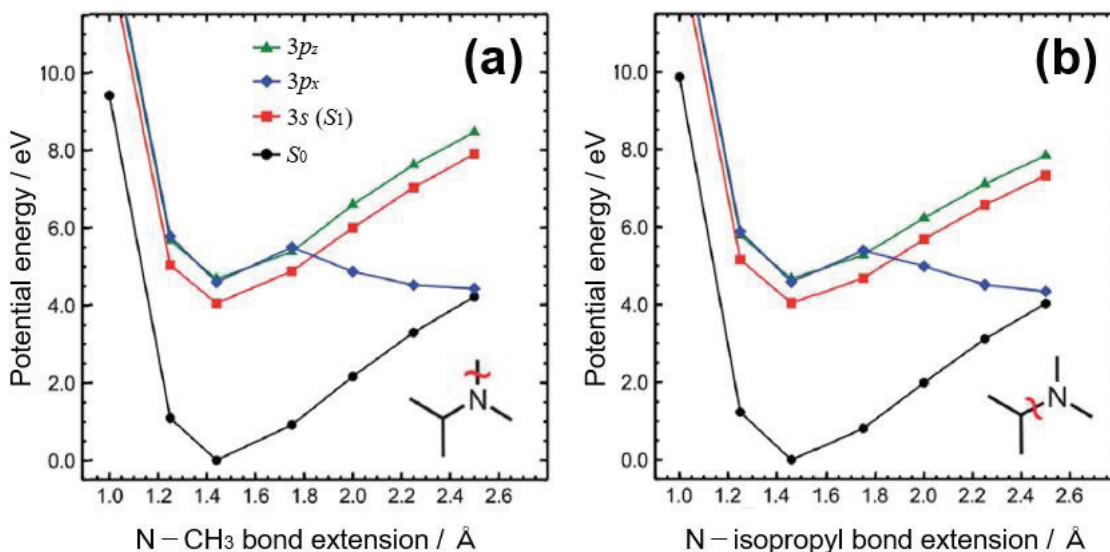


Figure 1.13 Potential energy curves for DMIPA calculated by Thompson *et al.* in Ref. 49: (a) the N–methyl bond, and (b) N–isopropyl bond. The bound S_0 and $S_1(3s)$ curves plotted by black and red, respectively. The $3p_x$ state (blue) is predissociative, while the $3p_z$ curve (green) is bound. For both N–C bond extensions, the $3p_z$ state crosses with the bound $3s$ state at $R_{N-C} \approx 1.8 \text{ \AA}$.

TMA also shows the broad absorption spectrum composed of the $S_2(3p)$ – S_0 and $S_1(3s)$ – S_0 bands. The photochemistry on the both $S_2(3p)$ and $S_1(3s)$ surfaces is similar to TAAs rather than NH₃-derivatives: the S_1 and S_2 dynamics are characterized by fluorescence and fast internal conversion.⁴⁸⁻⁵¹ The fluorescence of the $S_1(3s)$ state was investigated with emission spectroscopy in the excitation wavelength from the onset (250 nm) of the $S_1(3s)$ – S_0 band toward the peak of the $S_2(3p)$ – S_0 band. The fluorescence quantum yield (Φ_{flu}) were measured as a function of the excitation wavelengths of 215–250 nm; the Φ_{flu} was invariant and almost unity at excitation wavelengths above 240 nm and decreased rapidly with increasing the excitation energies below 235 nm. Although the emission intensity at the wavelength near the peak of the S_2 – S_0 band (206 nm) is quite low ($\Phi_{\text{flu}} < 0.01$), the measured

dispersed fluorescence spectrum at 206 nm showed a similar structure to that observed at 250 nm; therefore, the fluorescence from the S_1 state prepared by the $S_2 \rightarrow S_1$ internal conversion was suggested. Sequential studies by Cureton *et al.* found that the fluorescence decay time in the excitation wavelengths of 230–260 nm, where TMA is dominantly excited to the S_1 state, showed single exponential character, whereas at higher energies below 230 nm simultaneous excitation to the S_1 and S_2 states resulted in dual exponential decay.^{49,50} They explained this dual decay components as different method of preparing on the fluorescent S_1 state: the direct photoexcitation or the population via the $S_2 \rightarrow S_1$ internal conversion. The mixed absorption spectrum was decomposed by plotting the ratio between these two components, leading to speculate the S_2 origin of 42,500 cm^{-1} (235 nm).

Cardoza *et al.* applied time-resolved photoelectron spectroscopy (TRPES) to TMA in the S_1 and S_2 states.⁵¹ The observed photoelectron spectra allowed the spectroscopic determination of the band origins for three low-lying excited states: 37,550 cm^{-1} (266 nm) for the $3s$ state, 44,290 cm^{-1} (226 nm) for the $3p_{xy}$ state, and 44,290 cm^{-1} (224 nm) for the $3p_z$ state. The sub-structure of the $3p_{xy}$ and $3p_z$ states are not resolved in the absorption spectra and traditionally assigned to the S_2-S_0 band due to a small energy splitting of 380 cm^{-1} . On the basis of the photoelectron spectra and theoretical calculation, Cardoza *et al.* concluded that the probability of excitation to the $3p_z$ state, P_z , much more dominant than P_{xy} ($P_z / P_{xy} \sim 9$). The time-dependent photoionization-photoelectron spectra in the excitation at 200 nm and 208 nm demonstrated clearly evidence of the internal conversion

to the S_1 state. In addition, a time-dependent peak-shift in the S_2 signal prior to disappearance of the total S_2 signal was also found, indicating the relaxation from the $3p_z$ state with higher oscillator strength to the low-lying $3p_{xy}$ state. The rate constant of the total S_2 signal-decay was consistent with that of the S_1 signal-rise; therefore, an exclusive electronic-dynamics of the $S_2 \rightarrow S_1$ internal conversion with a 2.9 ps time constant was proposed. The rate constant for the $3p_z \rightarrow 3p_{xy}$ electronic relaxation prior to the $S_2 \rightarrow S_1$ internal conversion was also determined to be 75 fs. No signature of the S_1 state decay, in contrast, was found until 10 ps, which is time window of the measurements.

The photodissociation following the S_2 - S_0 photoexcitation at 193 nm was investigated using photofragment translational spectroscopy.^{56,57} A primary channel was the N-C bond rupture, $\text{N}(\text{CH}_3)_3 + h\nu \rightarrow \text{CH}_3 + \text{N}(\text{CH}_3)_2$, where the translational energy distribution consisted of distinct two components: the higher and lower kinetic energy components peaked at 84 kJ/mol and 188 kJ/mol, respectively. Since the kinetic energy release is correlated with the internal energy by the energy conservation law, the lower kinetic component was associated with generation of $\text{N}(\text{CH}_3)_2$ with larger internal energy, and vice versa. The higher kinetic component was definitely assigned to the $\text{N}(\text{CH}_3)_2(\tilde{X}^2\text{B}_1) + \text{CH}_3$ pathway, whereas the electronic state of the highly internally excited $\text{N}(\text{CH}_3)_2$ product conjugated with the lower kinetic component could not be determined in this measurement, and there are two possibility: the electronic excited $\tilde{A}^2\text{A}_1$ state whose term energy was theoretically calculated to be 153 kJ/mol, and the rovibrationally excited $\text{N}(\text{CH}_3)_2$ in the

ground electronic \tilde{X}^2B_1 state. The N—C bond fission at 193 nm was proposed to occur on the S_1 PES after the $S_2 \rightarrow S_1$ internal conversion, which facilitates the non-adiabatic transition around the exit conical intersection through the vibrational excitation of the NH_3 -frame out-of-plane mode on the basis of an assumption that the S_1 PES of TMA, as in case of NH_3 , crosses with the S_0 PES to form the exit conical intersection along the reaction coordinate.

Quantum chemistry calculations for investigation of the dissociative excited states of TMA have been carried out.^{58,59} The systematic calculations for CH_3NH_2 , $(CH_3)_2NH$, and $(CH_3)_3N$ by Taylor *et al.* indicated that the electronic character of the excited states varies with CH_3 -substitution of NH_3 molecule.⁵⁹ A Rydberg state on the carbon atom contribute to several low-lying states. The dissociative $3s$ state originated from carbon atom and the bound $3s$ state associated with the nitrogen center were found; however, the assignment of these states to the absorption spectrum was not concurred. TMA is a NH_3 -derivative molecule and also the simplest TAA molecule. The excited S_1 and S_2 states of TMA in Franck-Condon region are known to be predominantly $3s$ and $3p$ Rydberg character; however, the coupling preference of the σ_{N-C}^* orbital with either of the $3s$ or $3p$ Rydberg orbitals in TMA were not clarified.

1.4 Goal and Outline

The substitution of H atom to aliphatic substituent (R) in NH_3 influences the NH_3 photochemistry. Even methylamine, dimethylamine and trimethylamine which are substituted by the simplest R (CH_3 group), these $\text{N}-\text{CH}_3$ bond dissociation dynamics are significantly different from the $\text{N}-\text{H}$ bond dissociation of NH_3 . A first step toward understanding amine photochemistry is elucidation of the photodissociation dynamics of the CH_3 -substituted NH_3 ; therefore, we have investigated the $\text{N}-\text{CH}_3$ bond dissociation mechanisms of methylamine composed of both $\text{N}-\text{H}$ and $\text{N}-\text{CH}_3$ bonds and trimethylamine, which has only $\text{N}-\text{CH}_3$ bonds, on the basis of NH_3 photochemistry.

This chapter provided the general background for amine photochemistry. In Chapter 2, the experimental approaches employed in the present study are introduced. The experimental principle and apparatus are also explained in detail. In Chapter 3, the photodissociation dynamics for the $\text{N}-\text{C}$ bond fission and the $\text{NH}(\text{X}^3\Sigma^-)$ production following the S_1-S_0 transition of CH_3NH_2 are investigated. For the former pathway, we determined the electronic state of the nascent NH_2 product and revealed the electronic branching to the $\text{CH}_3 + \text{NH}_2(\tilde{\text{A}}^2\text{A}_1)$ and $\text{CH}_3 + \text{NH}_2(\tilde{\text{X}}^2\text{B}_1)$ asymptotes. On the other hand, the dependence of the $\text{NH}(\text{X}^3\Sigma^-)$ state distribution on the photoinitiated vibronic state of CH_3NH_2 , and the available energy partitioning are mentioned to the latter pathway. In Chapter 4, the $\text{N}-\text{C}$ bond dissociation dynamics on the S_2 and S_1 surfaces of TMA are examined. The reaction barrier which controls the yields for the dissociation and

fluorescence, and the critical TMA molecular geometry at the exit conical intersection are discussed. A summary of this thesis and the general conclusion are presented in Chapter 5. We show the recent apparatus-development for further elucidation of the CH_3NH_2 and TMA photochemistry and the preliminary results measured with this developed apparatus in Appendix.

1.5 Reference

1. J. Christodoulou, *J. Paediatr. Child Health* **48**, E153 (2012).
2. R. Runau, S. D. Peyerimhoff and R. J. Buenker, *J. Mol. Spectrosc.* **68**, 253 (1977).
3. E. Kassab and E. M. Evleth, *The Rydberg Photophysics and Photochemistry of Amines. in The Role of Rydberg States in Spectroscopy and Photochemistry: Low and High Rydberg States*, edited by C. Sándorfy (Springer, Dordrecht, 1999), Vol. 20, p. 231.
4. P. Rosmus, P. Botschwina, H. -J. Werner, V. Vaida, P. C. Engelking and M. I. McCarthy, *J. Chem. Phys.* **86**, 6677 (1987).
5. A. E. Douglas, *Discuss. Faraday Soc.* **35**, 158 (1963).
6. M. I. McCarthy, P. Rosmus, H.-J. Werner, P. Botschwina and V. Vaida, *J. Chem. Phys.* **86**, 6693 (1987).
7. M. N. R. Ashfold, C. L. Bennett and R. N. Dixon, *Chem. Phys.* **93**, 293 (1985).
8. J. Biesner, L. Schnieder, J. Schmeer, G. Ahlers, X. Xie, K. H. Welge, M. N. R. Ashfold and R. N. Dixon, *J. Chem. Phys.* **88**, 3607 (1988).
9. J. Biesner, L. Schnieder, G. Ahlers, X. Xie, K. H. Welge, M. N. R. Ashfold and R. N. Dixon, *J. Chem. Phys.* **91**, 2901 (1989).
10. E. L. Woodbridge, M. N. R. Ashfold and S. R. Leone, *J. Chem. Phys.* **94**, 4195 (1991).
11. M. N. R. Ashfold, G. A. King, D. Murdock, M. G. D. Nix, T. A. A. Oliver and A. G. Sage, *Phys. Chem. Chem. Phys.* **12**, 1218 (2010).
12. J. Ma, C. Xie, X. Zhu, D. R. Yarkony, D. Xie and H. Guo, *J. Phys. Chem. A* **118**, 11926 (2014).
13. K. L. Wells, G. Perriam and V. G. Stavros, *J. Chem. Phys.* **130**, 074308 (2009).
14. N. L. Evans, H. Yu, G. M. Roberts, V. G. Stavros and S. Ullrich, *Phys. Chem. Chem. Phys.* **14**, 10401 (2012).
15. J. D. Rodríguez, M. G. González, L. Rubio-Lago and L. Bañares, *Phys. Chem. Chem. Phys.* **16**, 406 (2014).
16. A. D. Smith, H. M. Watts, E. Jager, D. A. Horke, E. Springate, O. Alexander, C. Cacho, R. T. Chapman and R. S. Minns, *Phys. Chem. Chem. Phys.* **18**, 28150 (2016).
17. J. B. Nee, M. Suto and L. C. Lee, *J. Phys. B* **18**, L293 (1985).
18. B.-M. Cheng, H.-C. Lu, H.-K. Chen, M. Bahou, Y.-P. Lee, A. M. Mebel, L. C. Lee, M.-C. Liang and Y. L. Yung, *Astrophys. J.* **647**, 1535 (2006).
19. D. R. Yarkony, *Rev. Mod. Phys.* **68**, 985 (1996).
20. H. S. W. Massey, *Rep. Prog. Phys.* **12**, 248 (1949).
21. C. Zener, *Proc. R. Soc. Lon. A* **137**, 696 (1932).
22. C. De Grandi and A. Polkovnikov, *Quantum Quenching, Annealing and Computation* (Springer, Berlin Heidelberg, 2010), p. 75.
23. C. Wittig, *J. Phys. Chem. B* **109**, 8428 (2005).
24. M. -J. Hubin-Franskin, J. Delwiche, A. Giuliani, M. -P. Ska, F. Motte-Tollet, I. C. Walker, N. J. Mason,

- J. M. Gingell and N. C. Jones, *J. Chem. Phys.* **116**, 9261 (2002).
25. The MPI-Mainz UV/VIS Spectral Atlas of Gaseous Molecules of Atmospheric Interest: www.uv-vis-spectral-atlas-mainz.org.
26. M. Tsuboi, A. Y. Hirakawa and H. Kawashima, *J. Mol. Spectrosc.* **29**, 216 (1969).
27. H. Xiao, S. Maeda and K. Morokuma, *J. Phys. Chem. A* **117**, 5757 (2013).
28. K. M. Dunn and K. Morokuma, *J. Phys. Chem.* **100**, 123 (1996).
29. E. Kassab, J. T. Gleghorn and E. M. Evleth, *J. Am. Chem. Soc.* **105**, 1746 (1983).
30. J. V. Michael and W. A. Noyes, *J. Am. Chem. Soc.* **85**, 1228 (1963).
31. G. C. G. Waschewsky, D. C. Kitchen, P. W. Browning and L. J. Butler, *J. Phys. Chem.* **99**, 2635 (1995).
32. S. J. Baek, K.-W. Choi, Y. S. Choi and S. K. Kim, *J. Chem. Phys.* **117**, 10057 (2002).
33. S. J. Baek, K.-W. Choi, Y. S. Choi and S. K. Kim, *J. Chem. Phys.* **118**, 11026 (2003).
34. S. J. Baek, K.-W. Choi, Y. S. Choi and S. K. Kim, *J. Chem. Phys.* **118**, 11040 (2003).
35. M. H. Park, K.-W. Choi, S. Choi and S. K. Kim, Y. S. Choi, *J. Chem. Phys.* **125**, 084311 (2006).
36. D.-S. Ahn, J. Lee, J.-M. Choi, K.-S. Lee, S. J. Baek, K. Lee, K.-K. Baek and S. K. Kim, *J. Chem. Phys.* **128**, 224305 (2008).
37. D.-S. Ahn, J. Lee, Y. C. Park, Y. S. Lee and S. K. Kim, *J. Chem. Phys.* **136**, 024306 (2012).
38. C. Reed, M. Kono and M. N. R. Ashfold, *J. Chem. Soc. Faraday Trans.* **92**, 4897 (1996).
39. M. N. R. Ashfold, R. N. Dixon, M. Kono, D. H. Mordaunt and C. L. Reed, *Philos. Trans. R. Soc. London, Ser. A* **355**, 1659 (1997).
40. J. O. Thomas, K. E. Lower and C. Murray, *J. Phys. Chem. A* **118**, 9844 (2014).
41. J. O. Thomas, K. E. Lower and C. Murray, *J. Phys. Chem. Lett* **3**, 1341 (2012).
42. D. Townsend, S. A. Lahankar, S. K. Lee, S. D. Chambreau, A. G. Suits, X. Zhang, J. Rheinecker, L. B. Harding and J. M. Bowman, *Science* **306**, 1158 (2004).
43. A. G. Suits, *Acc. Chem. Res.* **41**, 873 (2008).
44. B. R. Heazlewood, M. J. T. Jordan, S. H. Kable, T. M. Selby, D. L. Osborn, B. C. Shepler, B. J. Braams and J. M. Bowman, *Proc. Natl. Acad. Sci. U. S. A.* **105**, 12719 (2008).
45. H. Xiao, S. Maeda and K. Morokuma, *J. Phys. Chem. Lett.* **2**, 934 (2011).
46. M. P. Grubb, M. L. Warter, A. G. Suits and S. W. North, *J. Phys. Chem. Lett.* **1**, 2455 (2010).
47. R. H. Newman, C. G. Freeman, M. J. McEwan, R. F. C. Claridge and L. F. Phillips, *Trans. Faraday Soc.* **67**, 1360 (1971).
48. Y. Matsumi and K. Obi, *Chem. Phys.* **49**, 87 (1980).
49. C. G. Cureton, D. V. O'Connor and D. Phillips, *Chem. Phys. Lett.* **73**, 231 (1980).
50. C. G. Cureton, K. Hara, D. V. O'Connor and D. Phillips, *Chem. Phys.* **63**, 31 (1981).
51. J. D. Cardoza, F. M. Rudakov and P. M. Weber, *J. Phys. Chem. A* **112**, 10736 (2008).
52. J. O. F. Thompson, L. B. Klein, T. I. Sølling, M. J. Paterson and D. Townsend, *Chem. Sci.* **7**, 1826 (2016).

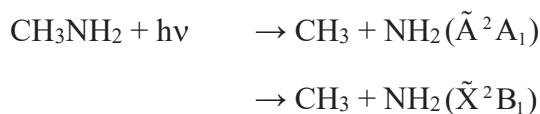
53. M. M. Zawadzki, M. Candelaresi, L. Saalbach, S. W. Crane, M. J. Paterson and D. Townsend, *Faraday Discuss.* **194**, 185 (2016).
54. L. B. Klein, T. J. Morsing, R. A. Livingstone, D. Townsend and T. I. Sølling, *Phys. Chem. Chem. Phys.* **18**, 9715 (2016).
55. M. P. Minitti, J. D. Cardoza and P. M. Weber, *J. Phys. Chem. A* **110**, 10212 (2006).
56. N. R. Forde, M. L. Morton, S. L. Curry, S. J. Wrenn and L. J. Butler, *J. Chem. Phys.* **111**, 4558 (1999).
57. N. R. Forde, L. J. Butler, B. Ruscic, O. Sorkhabi, F. Qi and A. Suits, *J. Chem. Phys.* **113**, 3088 (2000).
58. P. Avouris and A. R. Rossl, *J. Phys. Chem.* **85**, 2340 (1981).
59. D. P. Taylor, C. F. Dion and E. R. Bernstein, *J. Chem. Phys.* **106**, 3512 (1997).

Chapter 2

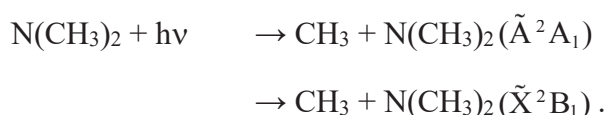
Experimental Principle and Methods

2.1 Experimental Approaches

Methylamine (CH_3NH_2) and trimethylamine ($\text{N}(\text{CH}_3)_3$, TMA) have complicated PESs along the N–C bond cleavage coordinate. In reactant region near FC region, a reaction barrier on PES of CH_3NH_2 , and existence of the $3p$ state energetically close to the $3s$ state in TMA cause predissociation and the competition between dissociation and electronic relaxation, respectively. Additionally, the conical intersection along N–C bond dissociation coordinate ($\text{CI}_{\text{N-C}}$) in product region, where the N–C bonds of CH_3NH_2 and TMA are considerably elongated, can cause the electronic branching of product on the basis of NH_3 photochemistry:



and



In the present study, we carried out a pump-probe experiment under the condition controlling the reactant and product states. A conceptual scheme for the employed pump-probe experiment is illustrated in Figure 2.1.

The advance in laser technology over the past few decades^{1,2} has allowed the development of spectroscopic techniques which enable one to experimentally obtain information on electronically excited-state dynamics. A pump-probe experiment has been

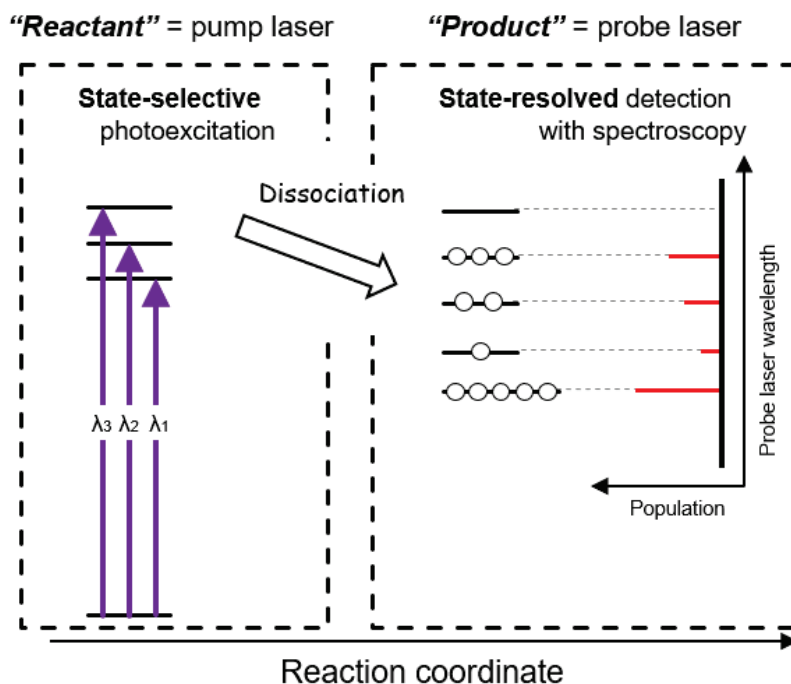


Figure 2.1 Conceptual scheme for the employed pump-probe experiment under the condition controlling the reactant and product states. State- and energy-selective photodissociation is initiated by pump laser, and the state-resolve detection is achieved by the probe laser with spectroscopy.

widely employed for exploring photodissociation dynamics. Two different pulsed lasers, pump and probe lasers, are used in this experiment. The pump laser photoexcites a parent molecule and initiates photodissociation, and the nascent photoproducts are irradiated by the second (probe) laser for detection after a short time delay from the pump laser. The pump-probe experiment is suitable for examining the photoinitiated-state dependence on the predissociation in the aliphatic amines because the photoexcitation to a discrete level and the detection are temporally separated. The UV absorption spectrum of CH_3NH_2 shows vibronic structure where each peak corresponds to a single vibronic level. We can inspect the photodissociation dynamics for each vibronic state of CH_3NH_2 by tuning pump laser

wavelength at a given peak in the UV spectrum. The UV absorption bands of alkyl amines extend to deep-UV (DUV, ~200 nm) region. Generally, the tunable wavelength laser source in this region is scarcely available; therefore, a DUV laser was designed and developed in the present study.

Products in photodissociation retain dynamical information of a dissociating molecule as rovibrational motions. Electronic states of the products, in addition, is a result of adiabatic or non-adiabatic dynamics if the parent molecule has a conical intersection along dissociation coordinate as well as NH_3 . In CH_3NH_2 and TMA photodissociation, we have measured the electronic and rovibrational state-distributions of the photoproducts, which are CH_3 , NH_2 and NH radicals, by resonantly enhanced multiphoton ionization (REMPI) spectroscopy and emission spectroscopy. Translational energy and scattering angular distributions of photoproducts are also significant physical-quantities for elucidation of photodissociation dynamics. A velocity-map imaging (VMI) method coupled with a spectroscopic detection, which was established by Eppink and Parker in 1997,^{3,4} enables to observe simultaneously both velocity and angular distributions. The translational energy distribution of the detected photoproduct is related to the internal energy distribution of the unobserved counter-product by energy and linear-momentum conservation laws, giving the energetic estimation of the electronic state of the counter-product. The scattering angular distribution becomes an index of a relative dissociation lifetime with respect to the rotational

period of parent molecule, and provides rarely information on orientation⁵ and alignment effect⁶.

Although the fact that one can discuss energetically the nascent electronic states of the unobserved products by imaging measurements is significantly useful, this method cannot give evidence for generation of electronically excited products. Spectroscopic detection of electronically excited photoproducts is not easy since photoexcitation of the electronic excited fragments for probing causes accidentally a second dissociation. The electronically excited $\text{NH}_2(\tilde{\text{A}}^2\text{A}_1)$ radical, which can be generated in the photodissociation of CH_3NH_2 , is unsuitable for a detection with laser spectroscopy. In this study, emission spectroscopy was applied to direct detection of $\text{NH}_2(\tilde{\text{A}}^2\text{A}_1)$ photoproduct in the CH_3NH_2 photodissociation.

2.2 Experimental Principles

2.2.1 REMPI Spectroscopy

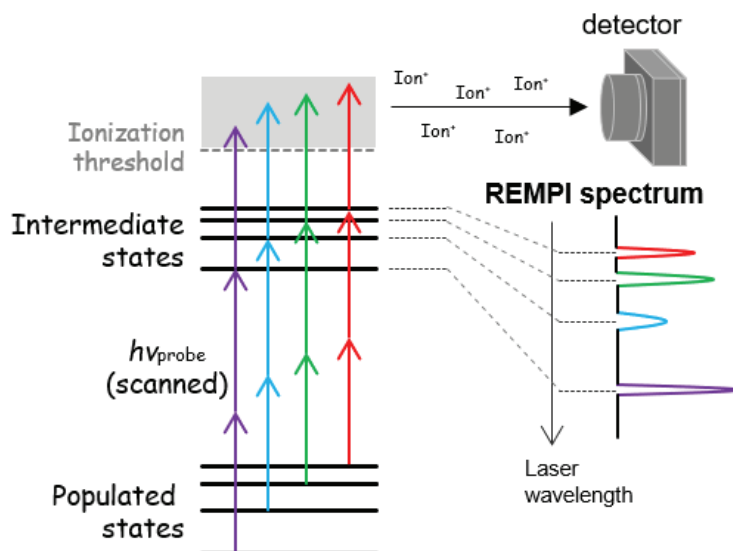


Figure 2.2 Schematic showing the basic concept of a $[2 + 1]$ REMPI detection scheme. As $h\nu_{\text{probe}}$ is scanned, target fragments in each lower state are excited individually to intermediated states and ionized. The intensity of resulting ions is monitored as a function of the probe laser wavelength to obtain the REMPI spectrum.

Resonantly enhanced multiphoton ionization (REMPI) spectroscopy is a photoionization technique where multiple photons are used for the excitation and the ionization of molecules as shown in Figure 2.2. REMPI is employed widely for state-selective ionization of various molecules and radicals.⁷ REMPI schemes are usually referred to as $m + n$, where m and n denote the number of photons used to the excitation and the ionization, respectively. We can obtain a REMPI spectrum by monitoring the intensity of generated ions as a function of excitation wavelength. In order to determine the population of each populated state from the REMPI spectrum, one must divide the intensity of the

spectral peaks by the oscillator strength (Franck-Condon factor). In present study, the CH₃ was detected with [2 + 1] REMPI scheme.

The 2 + 1 REMPI scheme via $3p_z^2A_2'' - \tilde{X}^2A_2''$ electronic transition was applied for the detection of the nascent methyl (CH₃) radicals in photodissociation. The scheme was established by Hudgens *et al.*⁸ and has been widely used for the detection of CH₃ radical in the gas phase. The equilibrium structure of CH₃ radical is planar with D_{3h} symmetry. The ground state has A_2'' symmetry due to the electronic configuration: $(1a_1')^2(2a_1')^2(2e')^4(2a_2'')^1$. Figure 2.3 shows the higher energy molecular orbitals for a planar CH₃ radical and their correlation to the united atom, fluorine. All of these levels are Rydberg states, and the state symmetry is the same as the molecular orbital symmetry. Table 2.1 lists the selection rules for several two-photon transitions from the ground \tilde{X}^2A_2'' state. Although the low-lying $3p_{xy}^2E'$ and $3p_z^2A_2''$ states are optically accessible from the ground state, the signal attributed to only the $3p_z^2A_2'' - \tilde{X}^2A_2''$ transition was detected.⁸ Owing to the planar (D_{3h}) structure, only the vibration with A_1' symmetry can undergo $\Delta v = \pm 1$ transitions. All other vibronic structure arises from $\Delta v = 0, \pm 2, \pm 4, \dots$ transitions. Because the molecular structures in the ground state and the excited $3p_z^2A_2''$ state are similar to each other, the FC factors of $\Delta v = 0$ transitions are larger than that of the other transitions.⁹

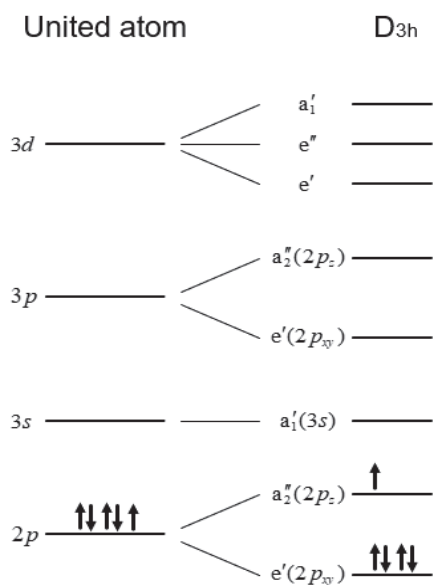


Figure 2.3 Correlation diagram between united atom, fluorine, and the D_{3h} symmetry orbitals of CH_3 radicals.

Table 2.1 Optical selection rules for transition from the vibrationless \tilde{X}^2A_2'' state of methyl radical to singly excited states of other symmetries. N and K denotes a rotational quantum number and a signed quantum number of total angular momentum about the symmetry axis, respectively.

Upper state symmetry species	Selection rule for two-photon excitation
A_1'	Forbidden
A_1''	$\Delta K = 0 \begin{cases} K = 0; \Delta N = \pm 1 \\ K \neq 0; \Delta N = 0, \pm 1, \pm 2 \end{cases}$
A_2'	Forbidden
A_2''	$\Delta K = 0 \begin{cases} K = 0; \Delta N = 0, \pm 2 \\ K \neq 0; \Delta N = 0, \pm 1, \pm 2 \end{cases}$
E'	$\Delta K = \pm 1; \Delta N = 0, \pm 1, \pm 2$
E''	$\Delta K = \pm 2; \Delta N = 0, \pm 1, \pm 2$

The vibrational band attributed to 2_1^1 band of CH_3 radical, where ν_2 denotes the out-of-plane bending mode (606 cm^{-1}), is enough far from other vibrational bands to be discriminated. However, the bands attributed to the C—H symmetric stretch (ν_1 , 3005 cm^{-1}) and the antisymmetric one (ν_3 , 3161 cm^{-1}) are unresolved because of the similar transition frequencies and the broad spectral line. Table 2.2 lists the transition frequencies and the Franck-Condon factors which was previously reported.^{8,10-13} The broad feature is caused by lifetime broadening arising from predissociation. The lifetime of CD_3 radical was estimated to be an upper limit of 3 ps at the vibrationless state, and this value decreased with increasing vibrational excitation (1 ps at $\nu_2 = 1$, 0.8 ps at $\nu_2 = 2$ and 0.4 ps at $\nu_2 = 3$).¹⁴

Table 2.2 Transition frequencies and the corresponding wavelengths and FC factors in the $2 + 1$ REMPI scheme via the $3p_z \ ^2A_2'' - \tilde{X} \ ^2A_2''$ transition. These values are taken from Refs. 8 and 11-14.

Transition	Wavelength / nm	Two-photon energy / cm^{-1}	FC factor
0_0^0	333.4	59,972	0.9234
1_1^1	334.0	59,881	-
1_0^1	317.9	62,886	0.0405
2_1^1	329.4	60,700	0.8208
2_2^2	325.8	61,390	0.6746
2_0^2	319.1	62,660	0.0700
2_3^3	322.7	61,972	0.4688
2_1^3	315.6	63,335	0.1575
3_1^1	333.9	59,898	-

2.2.2 Emission Spectroscopy

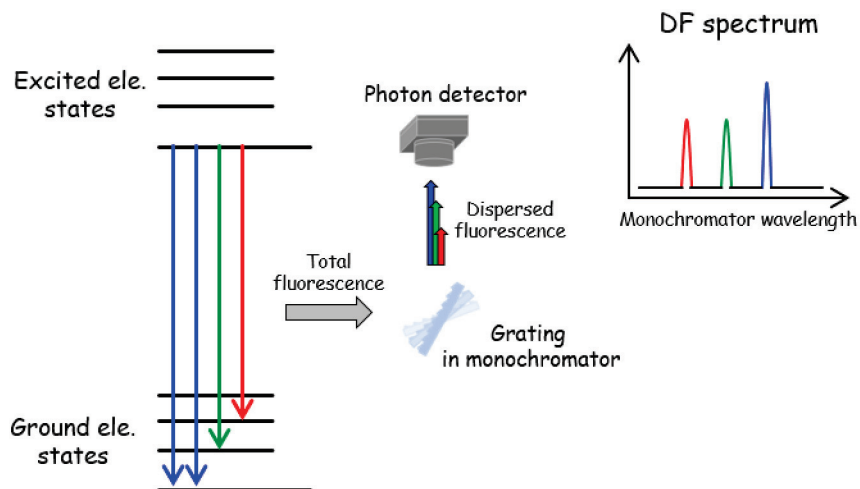


Figure 2.4 Schematic diagram of dispersed fluorescence (DF) measurements. Molecules at a rovibrational level in the electronically excited state generated in photochemical reaction or laser excitation emit photons as fluorescence. Total fluorescence is collected on a grating in a monochromator to be dispersed for each wavelength. DF spectrum is obtained by recording the intensity of the dispersed fluorescence with respect to the monochromator wavelength.

Molecules and radicals in a rovibrational level of an excited electronic state relax to various levels of the ground electronic state by emitting photons as fluorescence, as illustrated schematically in Figure 2.4. In dispersed fluorescence (DF) spectroscopy which is one of emission spectroscopy, the fluorescence to various levels in the lower state is dispersed by a grating in a monochromator prior to detection with a photon detector such as a photomultiplier tube. A DF spectrum is measured by recording the intensity of dispersed fluorescence as a function of the monochromator wavelength. The preparation of the detected molecule in the excited electronic state is achieved generally by laser excitation or photochemical reaction. A DF measurement with laser excitation is employed traditionally

for experimental determination of the energy level spacing and the oscillator strength of transitions. An electronically excited molecule generated in photochemical reaction has widely spread state-distribution in the upper electronic state. DF spectrum allows the direct detection of the electronically excited photoproduct and the determination of the nascent state-distribution which is information on the reaction dynamics. In the photodissociation of CH_3NH_2 , the electronic state of the NH_2 product was determined spectroscopically by the DF measurement.

The electronic configuration and term-type of the ground state of NH_2 radical is

$$(a_1)^2(b_2)^2(a_1)^2(b_1)^1, \ ^2B_1,$$

and of the low-lying excited states:

$$(a_1)^2(b_2)^2(a_1)^1(b_1)^2, \ ^2A_1,$$

$$(a_1)^2(b_2)^1(a_1)^2(b_1)^2, \ ^2B_2.$$

The observed transition should correspond to the allowed transition $\ ^2A_1 - \ ^2B_1$ rather than the forbidden transition $\ ^2B_2 - \ ^2B_1$. The spectrum of the NH_2 radical was first observed by Herzberg and Ramsay in 1952.¹⁵ Latter, Dressler and Ramsay discovered for the first time the Renner-Teller effect in the pattern of the rovibronic energy levels of its $\tilde{A}^2A_1 - \tilde{X}^2B_1$ transition.¹⁶ The analysis of the $\tilde{A}^2A_1 - \tilde{X}^2B_1$ spectrum revealed that the \tilde{X}^2B_1 electronic ground state is strongly bent, whereas the \tilde{A}^2A_1 state is quasilinear. The NH_2 radical in the \tilde{X}^2B_1 state has three vibrational freedoms: the symmetric N–H stretch (ν_1 , 3219.4 cm^{-1}), the deformation (ν_2 , 1497.2 cm^{-1}), and the asymmetric N–H stretch (ν_3 , 3301.1 cm^{-1}). The spectrum also showed that the majority of strong transitions correspond

to the progression $\tilde{A}^2A_1(0, v'_2, 0) - \tilde{X}^2B_1(0, 0, 0)$ and that the sub-states of the type $\tilde{A}^2A_1(1, v'_2, 0)$ also appear when they are in Fermi resonance with those of the type $\tilde{A}^2A_1(0, v'_2 + 2, 0)$ (in the notation appropriate to the bent molecule). The correlation between the linear and bent notations for the vibrational numbering is $v_2(\text{linear}) = 2v_2(\text{bent}) + K_a + 1$, where K_a denotes a signed quantum number of total angular momentum about the a -axis.

2.2.3 Velocity-Map Imaging

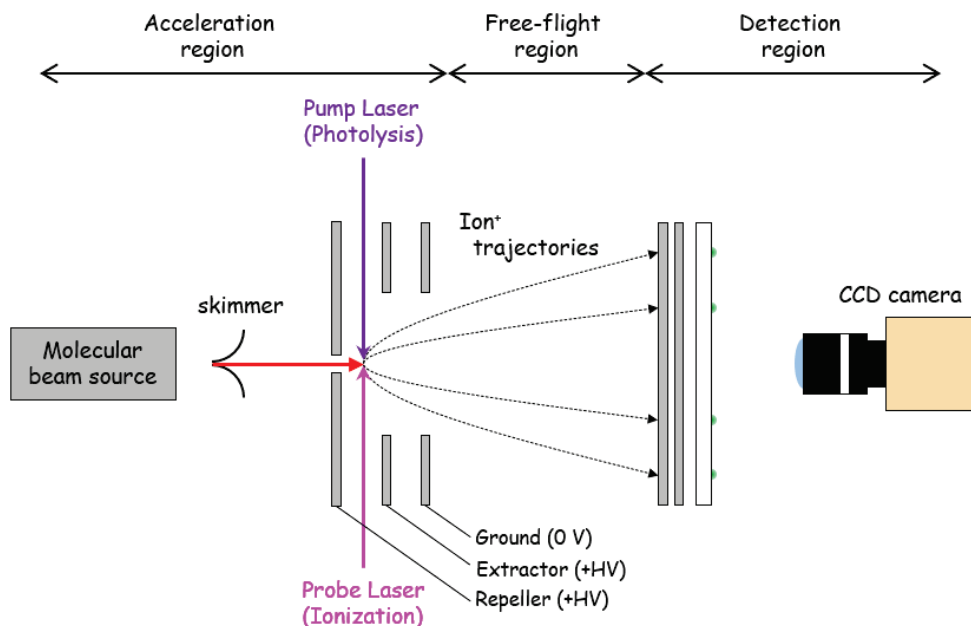


Figure 2.5 Schematic diagram of a standard VMI apparatus. A 3D ion cloud of photoproducts is created at the crossing point of the lasers (pump and probe) and the molecular beam. An open electrostatic lens assembly (a repeller, extractor and ground electrodes) maps the particle velocities uniquely onto a microchannel plate (MCP) detector. A CCD camera records the position of the emission from a phosphor screen, which installed in the back side of the MCP detector.

Velocity-map imaging (VMI) technique³ allows the three-dimensional (3D) velocity distribution of photoproducts to be visualized. The capability for simultaneous probing the translational energy and angular distributions of the photoproducts in a single image has contributed greatly to photodissociation dynamics studies. A standard VMI apparatus is represented schematically in Figure 2.5. The VMI apparatus is composed of three regions: acceleration, free-flight and detection regions. The acceleration region contains a molecular beam source, a skimmer, an ion optics consisted of three plates (repeller, extractor and

ground electrodes). There are no external electric fields for time-of-flight (TOF) mass selection in the free-flight region. A position sensitive detector and a CCD camera are equipped in the detection region.

The parent molecule of interest is expanded by a pulsed valve to generate the molecular beam, which is intercepted by a pair of counter-propagating laser beams (pump and probe). The pump laser pulse initiates the photodissociation of the parent molecule, and the generated photofragments fly out from reaction center with velocity and angular distributions. After a short delay, the probe laser pulse ionizes state-selectively one of the photoproducts by REMPI spectroscopy. The ions are then accelerated by the electrostatic field created by the ion optics through the free-flight region toward the imaging detector which is a microchannel plate (MCP) detector coupled to a phosphor screen. The pump and probe laser beams cross in a finite interaction volume, which causes considerable blurring of the measured distribution. This problem is solved by adjusting the electric field such that all ions with the same initial velocity and recoil-angle strike the same position on the detector. This condition for the electric field is called as the velocity mapping condition. The field is simultaneously tuned to compress the ion cloud along the axis such that the 3D distribution is 'pancaked' onto the detector. When an ion strikes at a position of the MCP detector, the corresponding position of the phosphor screen emits a flash of light. The optical image at the phosphor screen is captured by a CCD camera. The image recorded with the CCD camera is transferred to a PC on each laser pump-probe cycle for processing and data

storage. In order to obtain the image with high signal to noise ratio, a large number of images are summed to give the final image to be analyzed.

2.2.4 Analysis of Scattering Distribution

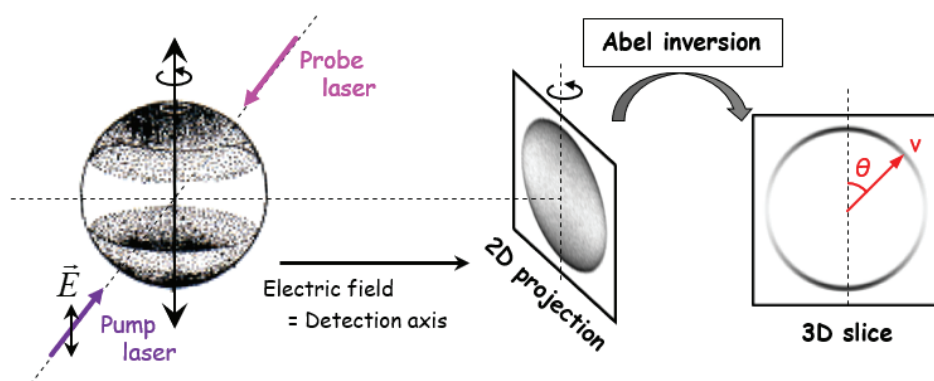


Figure 2.6 Measurement and analysis of a spherical ion-cloud of products. The cylindrically symmetric cloud (left) is created using a linearly polarized laser with the polarization axis lying in the vertical direction of the figure. An electric field projects the sphere of the ions onto a 2D detector (center). Abel inversion recovers the 3D sphere. The recoil velocity and angular distributions are extracted from a slice through the sphere (right).

Abel Inversion

The 3D cloud of the ionized photoproducts is detected as the 2D projection image in the VMI experiment. The linear polarized pump laser whose polarization is perpendicular to a detection axis is employed; therefore, the 3D velocity distribution is rotationally symmetric around the pump laser polarization direction. The observed 2D projection is restored mathematically to the original 3D distribution, and then a central slice-image of the 3D distribution is extracted. This transformation is well known as the Abel inversion.¹⁷

The sliced image possesses information of interest: the radius corresponds to the recoil speed, v , whereas the angle with respect to the pump laser polarization, θ , is the scattering angle. The scattering velocity and angular distributions, therefore, are extracted from the slice image by integrating the signal intensity over the angle and the radius, respectively. The velocity-to-radial calibration is conducted by using a well-known dissociation process. In present study, the calibration was carried out with reference to the scattering image of the $\text{CH}_3(v=0)$ fragment in the photodissociation of CH_3I at 266 nm: $\text{CH}_3\text{I} + h\nu(266\text{nm}) \rightarrow \text{CH}_3(v=0) + \text{I}(^2\text{P}_{1/2} \text{ and } ^2\text{P}_{3/2})$.¹⁸ The data set for this $\text{CH}_3(v=0)$ product is shown in Figure 2.7.

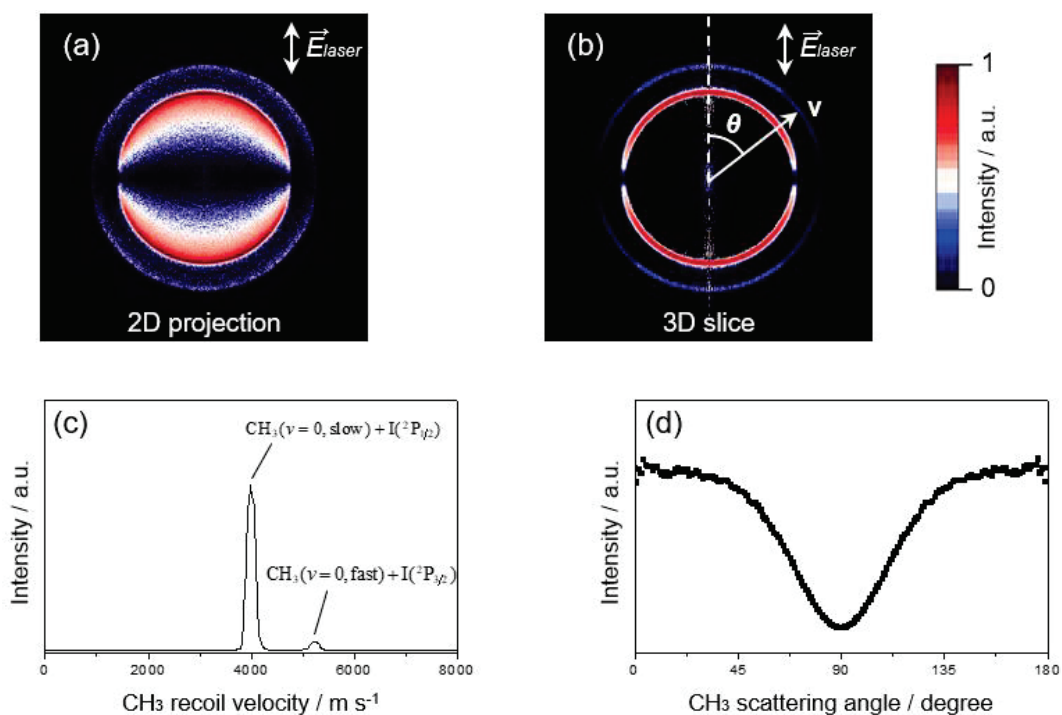


Figure 2.7 Data set for $\text{CH}_3(v=0)$ product in the photodissociation of CH_3I at 266 nm; (a) the 2D projection is transformed to (b) the 3D slice with the Abel inversion. Integrations of the intensity over the angle and radius produces (c) the velocity distribution and (d) the angular distribution, respectively.

Counter-Product Analysis

The strongest advantage of the VMI experiment coupled with laser spectroscopy is that the energy distribution of the unobserved product coproduced with a detected product is automatically obtained with the counter-product analysis. The recoil velocity of the detected photoproduct (v_P) is related with that of the counter-products (v_{CP}) by the linear momentum conservation law: $m_P v_P = m_{CP} v_{CP}$, where m_P and m_{CP} are mass of the detected product and the counter-product, respectively. The translational energy of the counter-product (E_{trans}^{CP}) is evaluated mathematically from $E_{trans}^{CP} = (m_P / m_{CP}) E_{trans}^P$. The total internal energy of undetected counter-product (E_{int}^{CP}) is obtained automatically by the energy conservation law: $h\nu_{pump} = D_0 + E_{int}^P + E_{trans}^{CP} + E_{int}^P + E_{int}^{CP}$, where $h\nu_{pump}$ and D_0 are the photon energy of the pump laser and the bond dissociation energy, respectively. The internal energy of the detected photoproduct (E_{int}^P) is selected by the state-resolved detection with REMPI spectroscopy. Thus, the E_{trans}^P -distribution obtained from the sliced image is converted into the E_{int}^{CP} -distribution. The slower and faster components of the detected product correspond to the higher and lower internal energy-components of the counter-product, respectively. For example, the photodissociation of CH_3I is well known to produce the spin-orbit excited ($^2P_{1/2}$) and ground ($^2P_{3/2}$) states of atomic iodide.¹⁸ The two peaks in the velocity distribution of the $CH_3(v=0)$ product shown in Figure 2.7 (c) are individually associated with these spin-orbit states: $CH_3(\text{slow}) + I(^2P_{1/2})$ and $CH_3(\text{fast}) + I(^2P_{3/2})$.

Determination of Anisotropy Parameter

An anisotropy parameter, β ($-1 \leq \beta \leq 2$), which indicates anisotropy of the scattering, is determined by fitting the angular distribution (Figure 2.7(d)) with the standard formula for one-photon photodissociation described by the Legendre polynomial $P_2(\cos \theta)$,

$$\frac{\partial \sigma}{\partial \Omega} = \frac{\sigma}{4\pi} (1 + \beta P_2(\cos \theta)),$$

where θ is the center-of-mass scattering angle with respect to the pump laser polarization direction, and σ is the integral cross section. A sign of the β depends on a vector correlation between the transition dipole moment (μ) and the dissociating bond direction (b); $\mu \perp b$ and $\mu \parallel b$ lead to negative and positive anisotropy parameters, respectively. The magnitude of the β gives the relative dissociation lifetime to the rotational period of the dissociating molecule. If the molecule dissociates instantaneously after photoexcitation by pump laser, the products fly out only along the dissociating bond direction, leading to $\beta = -1$ or 2 . On the other hand, assuming the quite longer dissociation lifetime than the rotational period of the parent molecule, the μ - b vector-correlation is completely lost due to the molecular rotation. In this limiting case, the scattering direction of the photoproducts is isotropic, and then the β value becomes approximately zero.

2.3 Experimental Apparatus

2.3.1 VMI Experiment

The VMI experimental apparatus employed in the present study, whose sectional drawing is displayed in Figure 2.8, consisted of a source chamber and a detection chamber that are separated by a wall with a skimmer (aperture diameter: 0.8 mm, Beam Dynamics). Two turbomolecular pumps (TMU1601P and TU521, Pfeiffer Vacuum) are equipped to evacuate the two chambers, whose typical base pressure is 1×10^{-7} Torr (source) and 3×10^{-8} Torr (detector). The source chamber contains a pulsed valve driven by a piezoelectric plate¹⁹ to generate the molecular beam. The detection chamber has a pair of inlets for the pump and probe laser beams. These laser beams are crossed with the molecular beam inside a set of ion optics. The ion optics are placed so that the ions are directed toward a position sensitive MCP detector with a phosphor screen in the back (Chevron-type, 40 mm in diameter, Phonics). The direction of the ion acceleration is collinear to the molecular beam. The distance between the ion optics and the MCP detector (490 mm) served as a free-flight region for time-of-flight (TOF) mass selection. The ion optics consists of three plates: a repeller-, an extractor- and a ground-electrode. The repeller plate has a hole (1mm diameter) for introducing the molecular beam into the ion optics assembly. The extractor and ground plates are ring-shaped with an open 20 mm diameter aperture to form an electrostatic ion-accelerating field. To achieve VMI condition, the ratio of electrostatic potential applied to the repeller and extractor was maintained at 0.69, which is first estimated by a numerical

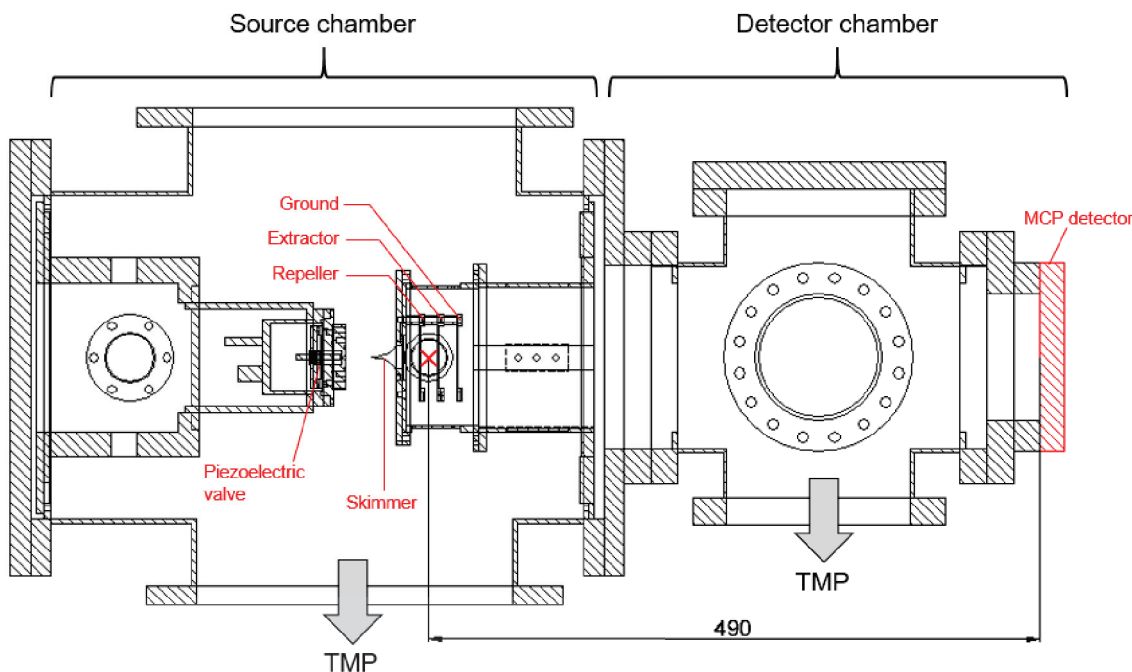


Figure 2.8 Sectional drawing of the experimental apparatus. Red cross mark corresponds to a crossing point between the laser beams and the molecular beam. A distance from the crossing point to the surface of the MCP detector which corresponds to a free-flight region is 490 mm.

simulation of ion trajectories with commercial software (SIMION 8.0) and then optimized by measuring the scattering distribution of the atomic oxygen fragment in the O_2 photodissociation at 266 nm region as a reference.⁴ Thus, the resolution and linearity of velocity of the VMI apparatus were sufficiently high for investigating the photodissociation dynamics of methylamine ($CH_3NH_2 + h\nu \rightarrow CH_3 + NH_2$) and trimethylamine ($N(CH_3)_3 + h\nu \rightarrow CH_3 + N(CH_3)_2$).

The molecular beam is irradiated by the pump and the probe laser beams at midway between the repeller and extractor electrodes. The nascent products in photodissociation are ionized state-selectively with REMPI spectroscopy. The ionized fragments are accelerated

by the VMI electrostatic field toward the MCP detector. A high voltage pulse defining the TOF (duration of 100 ns) is applied to the MCP detector for mass selection. The electron avalanche in the MCP detector striking the phosphor screen creates an ion image that is then captured using a CCD camera (C8800, Hamamatsu) controlled by a computer program (HiPic 9.4, Hamamatsu). The number of arriving ions is measured by monitoring the intensity of the emission from the phosphor screen using a photomultiplier tube (PMT, R2496, Hamamatsu). The signal from the PMT is averaged with a gated boxcar integrator (SR-250, Stanford Research System). Operation of the pulsed valve, the laser, and the imaging system with the TOF method are synchronously controlled by a digital delay generator (Model-555, Berkeley Nucleonics) combined with a home-made pulse distributor at a repetition rate of 10 Hz.

The wavelength of the pump laser was selected in the range of 200–240 nm to initiate the photodissociation on an arbitrary state of CH_3NH_2 or $(\text{CH}_3)_3\text{N}$. The laser oscillation in this region is achieved by using a developed deep-UV (DUV) laser for 200–220 nm and a second harmonic generation (SHG) unit for 220–240 nm. A tunable dye laser (CobraStretch, Spectra Physics) pumped by a Nd:YAG laser (LAB-170, Spectra Physics) is used for both DUV and SHG systems. The construction of the DUV laser source is explained later. The SHG output of the dye laser with a barium metaborate (BBO) crystal is used for the photolysis of 220–240 nm. The pulse energy of the pump laser was reduced to less than 10 μJ /pulse during all measurement to prevent multiphoton processes. Another laser set of a

frequency-doubled tunable dye laser (CobraStretch, Spectra Physics) pumped by a Nd:YAG laser (Powerlite 9010, Continuum) is employed for probing photoproducts by REMPI spectroscopy. The REMPI spectrum which is associated with the final-state distribution of the photoproducts is measured by scanning the probe laser wavelength continuously. The pulse energy of the probe laser was tuned to a suitable value in the range of 0.4–1.5 mJ/pulse for high signal-to-noise ratio. The remaining dye laser output in visible region is separated from the frequency-doubled light and is introduced into a Ne hollow cathode lamp (L2783-26NE-FE, Hamamatsu). Wavelength calibration of the REMPI spectrum can be performed by simultaneous measurement of an optogalvanic spectrum.²⁰

2.3.2 Construction of DUV Laser

A DUV light (~200 nm) is important for photodissociation study of organic molecules since their absorption bands are located in the DUV region as well as ammonia-derivatives. In the DUV region, a few laser sources which generate a single wavelength, such as a ArF excimer laser (193 nm) and a fifth harmonic of a Nd:YAG laser (212.8 nm), are used widely; however, a tunable laser source is scarcely available. We designed and developed a DUV laser based on sum-frequency mixing (SFM).²¹

The block diagram of the DUV laser and the schematic energy level description are illustrated in Figures 2.9. The DUV laser consists of several optical assemblies: a frequency-

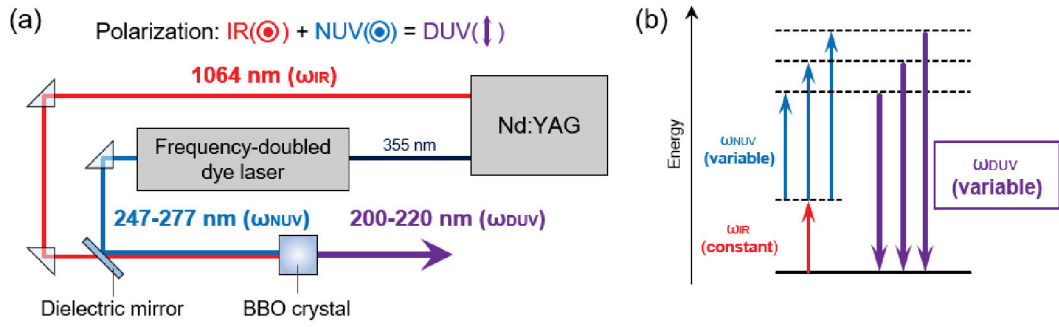


Figure 2.9 (a) Block diagram of the DUV laser. Two laser beams, ω_{IR} (1064 nm) and tunable ω_{NUV} (247–277 nm), are spatially and temporally overlapped on a BBO crystal to generation of ω_{DUV} (200–220 nm). The polarization directions of the incident IR and NUV beams are perpendicular to a paper surface, and that of the resulting DUV laser is vertical direction in a paper plane. (b) Schematic energy level description for the SFM process.

doubled dye laser pumped by a third harmonic of a Nd:YAG laser, a dielectric mirror (TFM-25.4C05-248 or TFM-25.4C05-266, SIGMAKOKI) and a BBO crystal ($\theta = 51.2$ degree, A-Star). The fundamental output (1064 nm, ω_{IR}) of the Nd:YAG laser and the second harmonic of the dye laser (near-UV, 247–277 nm, ω_{NUV}) are spatially and temporally overlapped on the BBO crystal, and then a DUV light ω_{DUV} , whose photon energy is sum of the two incident lights, ($\omega_{DUV} = \omega_{IR} + \omega_{NUV}$), is generated. The polarization of the IR and NUV laser beams is parallel to each other, and that of resulting DUV beam is perpendicular to the polarization direction of the incident beams. The dependence of the pulse energy of the DUV laser at 200 nm (I_{DUV}) on that of the IR (I_{IR}) and NUV laser (I_{NUV}) beams is displayed in Figures 2.10. The I_{DUV} was invariant with respect to the I_{IR} , and proportional to the I_{NUV} . The conversion efficiency from the incident I_{NUV} to the resulting I_{DUV} was typically 15 %.

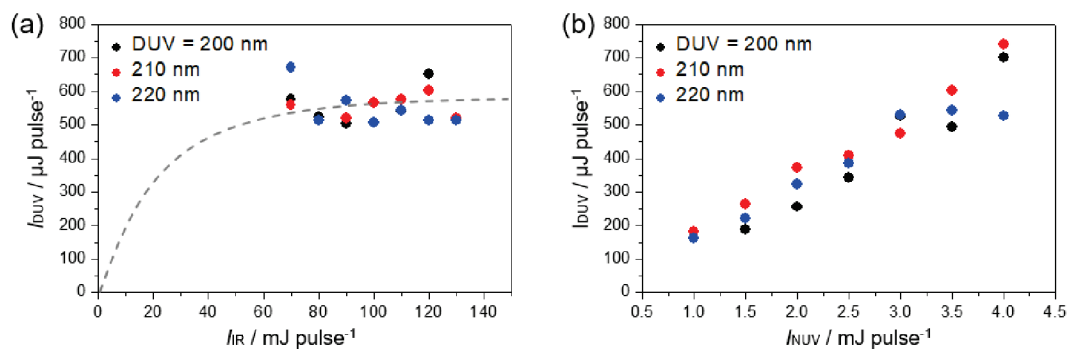


Figure 2.10 Dependence of I_{DUV} on (a) I_{IR} and (b) I_{NUV} . The I_{NUV} was fixed at 3.5 mJ/pulse in the I_{DUV} – I_{IR} plot. Black, red and blue plots indicate the I_{DUV} at 200, 210 and 220 nm, respectively.

2.3.3 Fluorescence Experiment

Figure 2.11 shows a schematic diagram of the apparatus used in the dispersed fluorescence measurement. A glass cell, whose total length is 690 mm, is evacuated by a dry primary pump (Adixen ACP28G, Alcatel Vacuum Technology). A sample gas at 298 K is slowly flowed in the cell, and the pressure is monitored with a capacitance manometer (122AA, MKS Baratron). The sample is irradiated by a pump laser, and then is photolyzed to generate products in the electronically excited state. The pump laser pulse in the UV region of 212–226 nm is generated with a frequency-doubled dye laser (LDP3002, Lambda Physik) pumped by the third harmonic of a Nd:YAG laser (GCR-170, Spectra Physics). The electronically excited products fluoresce to various rovibrational levels in the ground electronic state with own specific lifetime. The fluorescence is collected with a quartz lens ($f = 80$ mm, 40 mm in a diameter), focused on the entrance slit of a monochromator (JEOL JSG-125S, $f = 1250$ mm, $\Delta\lambda(\text{fwhm}) = 3$ nm), and detected with a photomultiplier tube (PMT, R928, Hamamatsu) mounted on the exit slit. The PMT is terminated with a 1 k Ω load resistor,

and the signal averaged with a gated integrator (SR-250, Stanford Research System) is stored on a disk of a PC. In order to evaluate the system performance, the DF spectrum of the nascent $\text{NH}_2(\tilde{\text{A}}^2\text{A}_1)$ fragment in the photodissociation of NH_3 at 193 nm with an ArF excimer laser (LEXtra50, Lambda Physik) was measured as a reference.²² The resolution and sensitivity of the apparatus was sufficiently high for direct detection of the $\text{NH}_2(\tilde{\text{A}}^2\text{A}_1)$ product in the photodissociation of CH_3NH_2 ($\text{CH}_3\text{NH}_2 + h\nu \rightarrow \text{NH}_2(\tilde{\text{A}}^2\text{A}_1) + \text{CH}_3$).

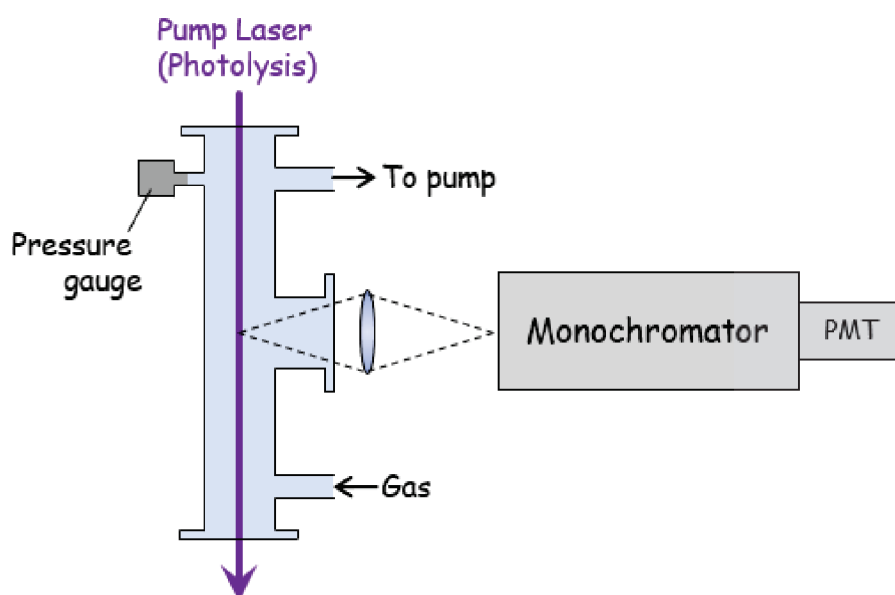


Figure 2.11 A schematic diagram of the gas cell. Fluorescence from the nascent products is focused on the entrance of a monochromator by a quartz lens ($f = 80$ mm), and is detected by the PMT terminated with a 1 k Ω load resistor.

2.4 Reference

1. W. Demtröder, *Laser Spectroscopy 1: Basic Principles*, (Springer, Berlin, 2015).
2. W. Demtröder, *Laser Spectroscopy 2: Experimental Techniques*, (Springer, Berlin, 2015).
3. A. T. J. B. Eppink and D. H. Parker, *Rev. Sci. Instrum.* **68**, 3477 (1997).
4. D. H. Parker and A. T. J. B. Eppink, *J. Chem. Phys.* **107**, 2357 (1997).
5. J. W. G. Mastenbroek, C. A. Taatjes, K. Nauta, M. H. M. Janssen and S. Stolte, *J. Phys. Chem.* **99**, 4360 (1995).
6. M. H. M. Janssen, D. H. Parker, G. O. Sitz, S. Stolte and D. W. Chandler, *J. Phys. Chem.* **95**, 8007 (1991).
7. M. N. R. Ashfold and J. D. Howe, *Annu. Rev. Phys. Chem.* **45**, 57 (1994).
8. J. W. Hudgens, T. G. DiGiuseppe and M. C. Lin, *J. Chem. Phys.* **79**, 571 (1983).
9. D. H. Parker, Z. W. Wang, M. H. M. Janssen and D. W. Chandler, *J. Chem. Phys.* **90**, 60 (1989).
10. R. Schott, J. Schlütter, M. Olzmann and K. Kleineremanns, *J. Chem. Phys.* **102**, 8371 (1995).
11. R. O. Loo, H. -P. Haerri, G. E. Hall and P. L. Houston, *J. Chem. Phys.* **90**, 4222 (1989).
12. P. Botschwina, J. Flesch and W. Meyer, *Chem. Phys.* **74**, 321 (1983).
13. H. B. Fu, Y. J. Hu and E. R. Bernstein, *J. Chem. Phys.* **123**, 234307 (2005).
14. J. G. Zhou, J. J. Lin, W. Shiu, S. -C. Pu and K. Liu, *J. Chem. Phys.* **119**, 2538 (2003).
15. G. Herzberg and D. A. Ramsay, *J. Chem. Phys.* **20**, 347 (1952).
16. K. Dressler and D. A. Ramsay, *Philos. Trans. R. Soc. London, Ser. A* **251**, 553 (1959).
17. B. J. Whitaker, *ACS Sympo. Ser.* **770**, 68 (2001).
18. A. T. J. B. Eppink and D. H. Parker, *J. Chem. Phys.* **109**, 4758 (1998).
19. D. Proch and T. Trickl, *Rev. Sci. Instrum.* **60**, 713 (1989).
20. D. S. King, P. K. Schenck, K. C. Smyth and J. C. Travis, *Appl. Opt.* **16**, 2617 (1977).
21. R. W. Boyd, *Nonlinear Optics, 3rd ed.*, (Elsevier, London, 2008).
22. V. M. Donnelly, A. P. Baronavski and J. R. McDonald, *Chem. Phys.* **43**, 271 (1979).

Chapter 3

Photodissociation Dynamics of Methylamine

3.1 Introduction

Chemical reaction mechanisms are often understood by the characteristic nuclear motions in a few critical regions of the reaction potential energy surfaces (PESs). A reaction barrier controls reactivity, and a surface crossing determines the branching ratio of competing product pathways. The photochemistry of ammonia (NH_3) is a typical example of a reaction mechanism explained by the reaction barrier of the excited state (\tilde{A}^1A_2'') and the conical intersection between the excited state and the ground state (\tilde{X}^1A_1').¹⁻⁴ The reaction barrier of the \tilde{A}^1A_2'' state is located at an elongated N–H bond length ($R_{\text{N-H}} \sim 1.3$ Å) from the equilibrium distance in the \tilde{X}^1A_1' state (~ 1.0 Å). The \tilde{A}^1A_2'' and \tilde{X}^1A_1' PESs are adiabatically correlated to the $\text{NH}_2(\tilde{A}^2A_1) + \text{H}$ and $\text{NH}_2(\tilde{X}^2B_1) + \text{H}$ product pathways in the pyramidal geometry, respectively. The conical intersection of these two PESs in the planar geometry is located at the longer N–H distance (~ 1.7 Å),^{5,6} determining the branching ratio of the product pathways.^{2-4,7} A similar argument has been presented for the photodissociation dynamics of methylamine (CH_3NH_2), which is the simplest ammonia-derivative species.⁸⁻¹¹ Methylamine has two types of σ -bonds to nitrogen (N–C and N–H), both of which are photodissociated following the S_1 – S_0 transition (the first absorption band in 190–240 nm).^{9,11-15} In both N–C and N–H bond fission channels, the S_1 and S_0 states are adiabatically correlated to the pathway with the electronically excited product ($\text{CH}_3 + \text{NH}_2(\tilde{A}^2A_1)$, $\text{H} + \text{CH}_3\text{NH}(\tilde{A}^2A')$) and the pathway with only ground state products, respectively. The S_1 PES has potential barriers along both N–C and N–H bond lengths at

a slightly longer bond length than each equilibrium length in the S_0 state.^{16,17} In both fission channels, conical intersections of the S_1 and S_0 PESs are formed at further elongated bond distances, similarly to NH_3 . As for the generation of $\text{CH}_3 + \text{NH}_2$ products, it is simply considered that the reactivity of the $\text{N}-\text{C}$ bond fission is first governed by the reaction barrier height in the outer Franck–Condon region, and then the bifurcation to the $\text{CH}_3 + \text{NH}_2(\tilde{\text{A}}^2\text{A}_1)$ and $\text{CH}_3 + \text{NH}_2(\tilde{\text{X}}^2\text{B}_1)$ pathways is caused by a non-adiabatic transition around the conical intersection region. This explanation, based on the successive two-stage mechanism, is applicable only for the single-dimensional elongation of a dissociating bond, which is the case in ammonia photodissociation. Substitution of a hydrogen atom of NH_3 by a methyl group provides additional degrees of freedom for the system to exhibit complex nuclear dynamics, which is a key issue in the photochemistry of polyatomic molecules.

In reaction dynamics, the generation of the $\text{NH}_2(\tilde{\text{A}}^2\text{A}_1)$ product in the photodissociation of CH_3NH_2 remains controversial under a molecular beam condition. The center-of-mass translational energy distribution for the $\text{N}-\text{C}$ bond fission obtained by photofragment translational spectroscopy at 222 nm was explained by Waschewsky *et al.* as the result of the exclusive generation of the NH_2 product in the $\tilde{\text{A}}^2\text{A}_1$ state.¹¹ Recently, Thomas *et al.* applied resonantly enhanced multi-photon ionization (REMPI) spectroscopy to the CH_3 fragment at photolysis wavelengths of 222–240 nm.¹³ The REMPI spectra were assigned to the sequential bands of the ν_3 (degenerate $\text{C}-\text{H}$ stretch) mode excited up to $\nu_3 = 3$. Because the CH_3 fragment was thus internally excited, the NH_2 counter-product was

indicated as populated in the \tilde{X}^2B_1 state on the basis of the energetic consideration. Participation of the upper adiabat would be ideally identified by laser spectroscopy applied to the $NH_2(\tilde{A}^2A_1)$ product. However, direct application of laser detection to electronically excited species is not easy.

Recently, Thomas *et al.* found a production of $NH(X^3\Sigma^-)$ photofragment by REMPI spectroscopy in the wavelength range of 222–240 nm. On the basis of standard thermochemical data, the counter-product of the $NH(X^3\Sigma^-)$ product is determined to be only closed shell CH_4 fragment. They proposed that the mechanism involves intramolecular abstraction between a radical pair ($CH_3\cdots NH_2$) on the triplet state via roaming-mediated intersystem crossing (ISC),¹⁸ where “roaming” is a reaction mechanism involving intramolecular recombination discovered in unimolecular photolysis of simple species such as formaldehyde (HCHO) and nitrate radical.^{19–22} Roaming in the HCHO photodissociation provides an alternative route to the molecular products, $H_2 + CO$, that avoids the conventional skewed transition state (TS) on the S_0 surface. The $H + CHO$ radical-pair production is frustrated, leading to extended excursions at long-range region prior to reaction. The long-range intramolecular abstraction of H atom from the CHO moiety provides vibrationally hot H_2 and rotationally cold CO. Thomas *et al.* measured the rotationally unresolved REMPI spectra of the $NH(X^3\Sigma^-)$ product in the photodissociation in wavelength range of 222–240 nm with 3 + 1 REMPI scheme via $D^3\Pi - X^3\Sigma^-$ transition.¹⁸ The rotational temperature of the nascent $NH(X^3\Sigma^-)$ fragment was estimated

to be $\sim 700\text{--}800$ K by least-squares fits of the simulation to the experimental band contours, indicating generation of the modestly rotationally excited NH ($X^3\Sigma^-$) fragment. The dependence of the branching fraction for NH ($X^3\Sigma^-$) production on the initial vibronic state prepared was suggested; excitation on the 9_0^1 and 7_0^1 bands leads to 2.1 and 1.4 times more NH ($X^3\Sigma^-$) than that on the 0_0^0 band. They proposed that a roaming in the long-range region provides ample opportunity for ISC to the T_1 surface on the S_0 surface of CH_3NH_2 prepared by the $S_1 \rightarrow S_0$ internal conversion, upon which reaction to produce $\text{CH}_4 + \text{NH}$ ($X^3\Sigma^-$) ultimately occurs. Theoretical study by Xiao *et al.* found a seam of crossing between S_0 and T_1 in a partially dissociated $\text{CH}_3\cdots\text{NH}_2$ geometry supported the roaming-like pathway to $\text{CH}_4 + \text{NH}$ ($X^3\Sigma^-$) products.¹⁶

In this study, we perform two complementary experiments for the photodissociation of CH_3NH_2 : state-resolved scattering under a molecular beam condition and dispersed fluorescence spectroscopy in a gas cell. The former is employed for the CH_3 and NH ($X^3\Sigma^-$) photofragments, yielding the nascent internal energy distributions of the NH_2 and CH_4 counter-products. In addition, the dependence of the product state-distribution and the available energy partitioning on the photoinitiated states of CH_3NH_2 is examined by varying the photolysis wavelength over the $S_1\text{--}S_0$ absorption band. The latter is conducted to directly identify the electronic state of the NH_2 product, whose total internal energy was determined by the scattering data of the CH_3 counter-product.

3.2 Experimental Methods

The pump-probe experiment under a molecular beam condition was performed by using a velocity-mapping imaging (VMI) apparatus, which consists of an imaging system with a time-of-flight (TOF) mass spectrometer. The details of the VMI apparatus have been described in Chapter 2. A molecular beam of CH_3NH_2 seeded in He (1 %) was generated by a piezoelectric valve with a stagnation pressure of 2 atm. The pump and probe laser beams, which were aligned in the counter-propagating direction, were focused by quartz lenses ($f = 350$ mm and 300 mm, respectively) on the molecular beam. The pump laser pulse (50–100 $\mu\text{J}/\text{pulse}$) in the deep-UV range of 205–220 nm and the near-UV range of 220–240 nm was generated by sum-frequency mixing (SFM) and second harmonic generation (SHG), respectively. A tunable dye laser (CobraStretch, Spectra Physics) pumped by a Nd: YAG laser (LAB-170, Spectra Physics) was used for SFM and SHG. The photolysis wavelengths were tuned to the eight vibronic bands of the $S_1 - S_0$ electronic transitions of CH_3NH_2 , whose UV absorption spectrum²³ is shown in Figure 3.1 where vertical lines denote the positions for each vibronic band which is assigned to progressions in the NH_2 wagging mode (ν_9 , 636 cm^{-1}) and the CH_3 rocking mode (ν_7 , 1008 cm^{-1}),²⁴ while eight arrows indicate the selected vibronic bands in this study. The selected vibronic bands, excitation wavelengths (λ_{ex}), and absorption cross sections ($\sigma_{\text{abs}}(\lambda_{\text{ex}})$) are listed in Table 3.1.

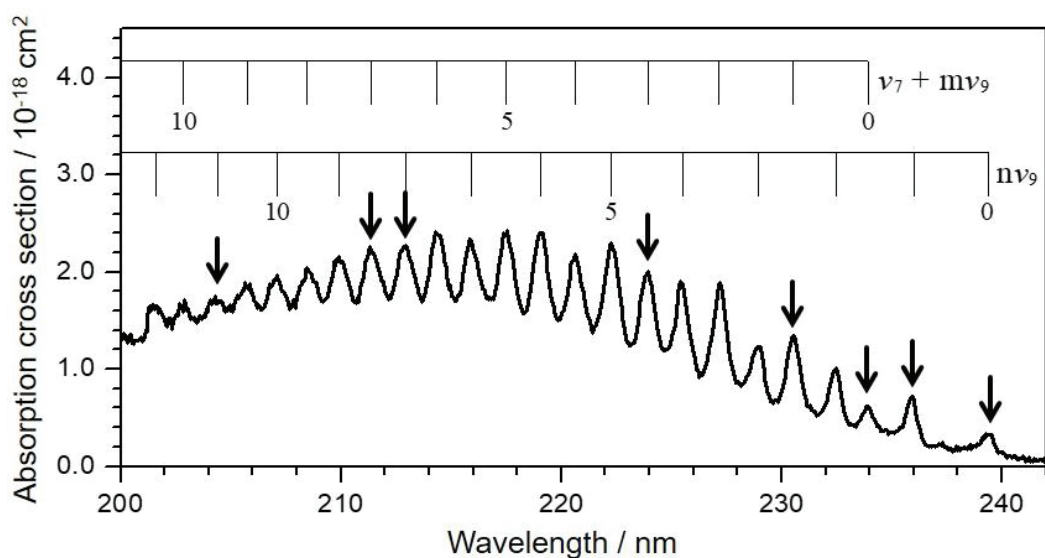


Figure 3.1 UV absorption spectrum associated with the S_1-S_0 electronic transition of methylamine (CH_3NH_2). The assignments with two optical active ν_7 (CH_3 rocking) and ν_9 (NH_2 wagging) modes displayed by vertical lines are taken from Ref. 24. Eight arrows denote the positions of the CH_3NH_2 photoinitiated states selected in the imaging experiment.

Table 3.1 Eight selected vibronic band, excitation wavelength (λ_{ex}), and absorption cross sections, $\sigma_{\text{abs}}(\lambda_{\text{ex}})$.

Vibronic band	$\lambda_{\text{ex}} / \text{nm}$	$\sigma_{\text{abs}}(\lambda_{\text{ex}}) / 10^{-18} \text{ cm}^2$
9_0^{11}	205.3	1.86
$7_0^1 9_0^7$	211.0	2.39
9_0^8	212.8	2.44
$7_0^1 9_0^3$	223.9	2.17
$7_0^1 9_0^1$	230.4	1.38
7_0^1	234.3	0.63
9_0^1	236.3	0.71
0_0^0	239.9	0.30

The probe laser pulse (~ 1.2 mJ/pulse), which was obtained from another set of a frequency-doubled tunable dye laser (CobraStretch, Spectra Physics) pumped by the second harmonic of another Nd:YAG laser (Powerlite 8000, Continuum), was used for detection of the CH_3 and $\text{NH}(\text{X}^3\Sigma^-)$ fragments: the $2 + 1$ REMPI scheme via the $3p^2A_2'' - \tilde{\text{X}}^2A_2''$ transition (332–335 nm),^{25,26} and the $3 + 1$ REMPI one via the $\text{D}^3\Pi - \text{X}^3\Sigma^-$ transition (335–340 nm)¹⁸ were applied to the CH_3 and $\text{NH}(\text{X}^3\Sigma^-)$, respectively. Wavelength calibration was performed by an optogalvanic method in the visible region using a Ne hollow cathode lamp. The probe laser pulse was delayed by 30 ns from the pump laser pulse. The ionized products were accelerated by VMI electrodes toward a microchannel plate (MCP) detector with a phosphor screen was recorded by a charge-coupled device (CCD) camera (C8800, Hamamatsu). The ion intensity was obtained with a photomultiplier tube (R2496, Hamamatsu), which measured the emission from the phosphor screen. The pulsed valve, the pump and probe laser pulses, and the TOF gate of the MCP detector for mass selection were synchronously controlled by a cascade of digital delay generators (Model-555, BNC and Model-DG535, Stanford Research Systems) with a repetition rate of 10 Hz.

The setup of the gas cell experiment has been also described in Chapter 2. Gaseous CH_3NH_2 [$p(\text{CH}_3\text{NH}_2) = 500$ mTorr], which was slowly flowed without a buffer gas to prevent the collisional relaxation of the nascent $\text{NH}_2(\tilde{\text{A}}^2A_1)$ product, was irradiated by the unfocused photolysis laser beam (~ 1.0 mJ/pulse) from a frequency-doubled dye laser (LPD3002, Lambda Physik) pumped by the third harmonic of a Nd:YAG laser (GCR-170,

Spectra Physics). The emission from the $\text{NH}_2(\tilde{A}^2A_1)$ photoproduct was collected through a band pass filter (Y-43, Toshiba) and focused with a quartz lens ($f=80$ mm a diameter of 40 mm) in the entrance slit of a monochromator (JSG-125S, JEOL, $\Delta\lambda(\text{fwhm})=3$ nm). The emission intensity was measured with a photomultiplier tube (R928, Hamamatsu) mounted on the exit slit.

A commercial CH_3NH_2 sample (40 % in water, Aldrich) was used in the measurements after purification by vacuum distillation. The distillation was repeated until the vapor pressure reached 2.5 atm, which is the vapor pressure of pure CH_3NH_2 at room temperature estimated from the Antoine equation.²⁷ The concentration of the water contaminant was much less than 1 % in the distilled CH_3NH_2 sample. In the molecular beam experiment, a low sample concentration pressure were applied to avoid formation of clusters ($\text{CH}_3\text{NH}_2-\text{H}_2\text{O}$, $(\text{CH}_3\text{NH}_2)_2$). We inspected the change of the scattering signal by varying the concentration and the stagnation pressure to higher values than the measured conditions, confirming no significant contribution of clusters to the experimental results.

3.3 Results

3.3.1 REMPI Spectra of the CH₃ Photofragments

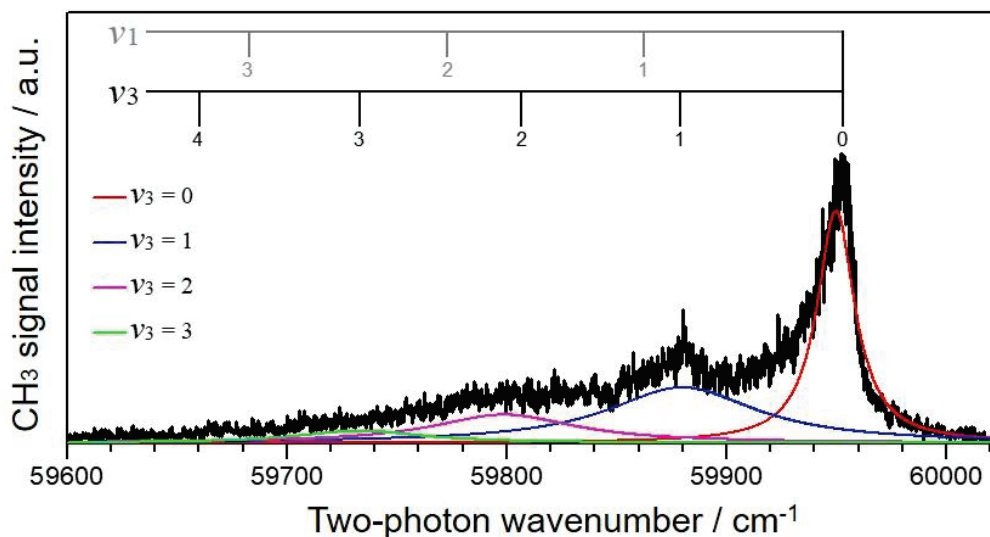


Figure 3.2 2 + 1 REMPI spectrum of CH₃ photofragments in the CH₃NH₂ photodissociation at 205.3 nm. The vibrational structure is assigned to the sequence band of the symmetric or antisymmetric C–H stretching modes (ν_1 or ν_3 , respectively). The band position of the ν_1 (gray) and ν_3 (black) modes are displayed. The quantum number of the ν_3 mode is used for the band assignment. The fits to the spectrum for each band are performed using Lorentzian functions.

The REMPI spectrum of the CH₃ photofragment generated at the photolysis wavelength of 205.3 nm is shown in Figure 3.2. The spectrum was measured under a molecular beam condition, yielding the nascent-state distribution of the CH₃ product. The vibrational structure displays a feature of the sequence of the C–H stretching mode. The transition frequencies associated with the two C–H stretching modes (ν_1 and ν_3) in this $3p^2A_2'' - \tilde{X}^2A_2''$ electronic transition are so close that the symmetric and antisymmetric forms of the CH₃ product cannot be discriminated.^{28,29} A similar REMPI spectrum of the deuterated product (CD₃) was analyzed as well.¹³

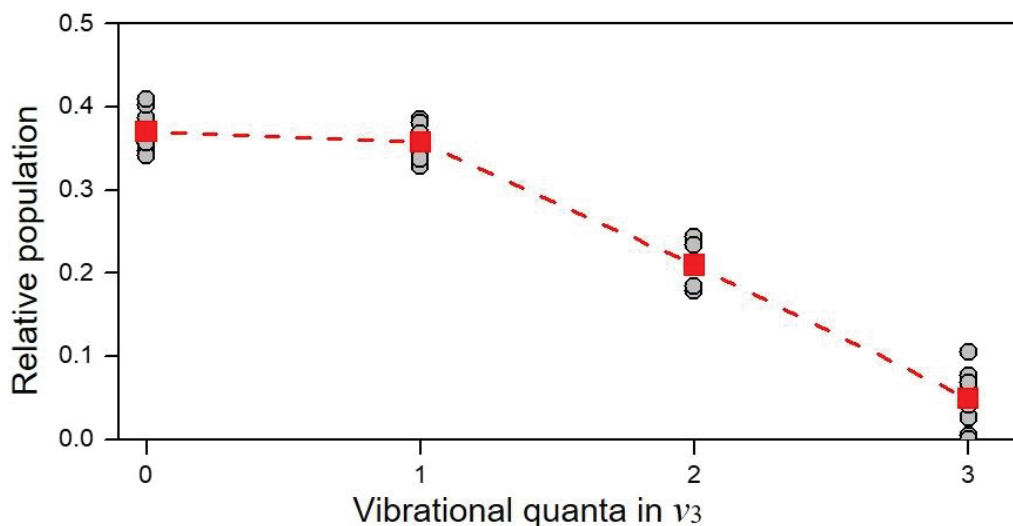


Figure 3.3 Nascent vibrational population distributions derived from 2 + 1 REMPI spectra of the CH_3 product in methylamine photodissociation at eight photolysis wavelengths of 205–240 nm. Distributions following excitation to each vibronic band are denoted by gray circles. The average value over these photoinitiated bands is shown by red squares.

We extended the photolysis wavelength up to 240 nm, which is associated with the band origin (0_0^0 band) of the S_1-S_0 transition of CH_3NH_2 . The REMPI spectra of the CH_3 product at eight photoinitiated states of CH_3NH_2 displayed no significant difference. The broad envelope of each vibrational band indicates highly rotational excitation of the CH_3 product. The spectral contour analysis yielded the vibrational-state distribution of the CH_3 fragment with high C–H mode excitation. The rotational distribution was approximated as a Lorentzian function centered at the calculated band frequency. We applied the same analysis procedure as that employed in the previous study¹³ for comparing the vibrational-state populations between the longer and shorter wavelength regions of the absorption band. The ν_3 vibrational-state populations of the CH_3 product at each photolysis wavelength are shown in Figure 3.3.

3.3.2 Vibrationally State-Resolved Ion-Images of the CH₃ Products

Figure 3.4 shows the CH₃ scattering images following initial 9_0^{11} excitation of CH₃NH₂ at 205.3 nm measured at the peak of the bands associated with the vibrational ground state (Figure 3.4 (a)) and the $\nu_3 = 1$ state (Figure 3.4 (b)). The difference between the scattering distributions of the $\nu_3 = 0$ and 1 states is seen in the translational energy distributions ($P(E_T^{\text{CH}_3})$), Figures 3.4 (c), (d) which were obtained through image data analyses with the Abel inversion. It was found that the CH₃($\nu = 0$) fragment is produced with high and low kinetic energies (Figure 3.4 (c)), whereas the vibrationally excited CH₃ fragment has a single kinetic energy component (Figure 3.4 (d)). The lower kinetic energy component observed in the CH₃($\nu = 0$) fragment (red curve) is distributed within a narrow $E_T^{\text{CH}_3}$ range, < 10 kJ/mol. The higher kinetic energy component exhibits the relatively broader distribution (with a maximum at $E_T^{\text{CH}_3} \approx 40$ kJ/mol), similarity to $P(E_T^{\text{CH}_3})$ of the CH₃($\nu_3 = 1$) fragment (blue curves). Therefore, the state-resolved $P(E_T^{\text{CH}_3})$ distributions imply that the CH₃ photofragment has two production origins; only one of them operates the generation of the slow CH₃ fragment in the vibrational ground state.

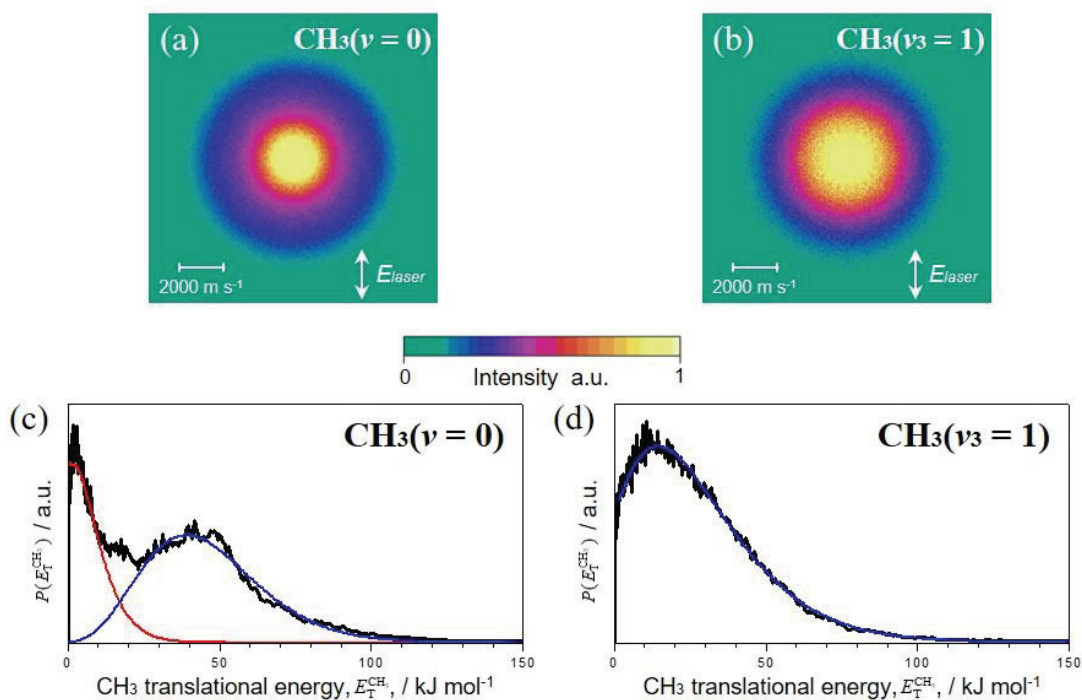


Figure 3.4 Vibrationally state-resolved scattering images of the CH₃ fragment in the (a) $\nu = 0$ and (b) $\nu_3 = 1$ states at the photolysis wavelength of 205.3 nm. The translational energy distributions of (c) the CH₃($\nu = 0$) and (d) the CH₃($\nu_3 = 1$) fragments obtained from the image data analysis. The fitting of the recoil velocity distributions is performed using Gaussian functions: Two and one gaussian functions were required for fitting to the velocity distributions of the CH₃($\nu = 0$) and the CH₃($\nu_3 = 1$) products, respectively. The recoil velocity distributions and fitting curves were transformed to the translational energy distributions by using Jacobian.

The internal energy of the NH₂ counter-product ($E_{\text{int}}^{\text{NH}_2}$) is uniquely related to $E_{\text{T}}^{\text{CH}_3}$ in the state-resolved scattering results by the energy conservation law,

$$h\nu = D(\text{CH}_3 - \text{NH}_2) + E_{\text{T}}^{\text{CH}_3} + E_{\text{T}}^{\text{NH}_2} + E_{\text{int}}^{\text{CH}_3} + E_{\text{int}}^{\text{NH}_2},$$

where the value of 359.6 kJ/mol for the bond dissociation energy ($D(\text{CH}_3 - \text{NH}_2)$)³⁰ of CH₃ + NH₂ was used in the evaluation. The rotational energy in the internal energy of the CH₃ fragment ($E_{\text{int}}^{\text{CH}_3}$) was neglected in the present analysis although the REMPI spectra

indicated the higher rotational excitation compared to the case for a different photolysis system,³¹ because the unresolved rotational structure and the overlapping of the band contours limited accurate evaluation of the rotational energies. The internal energy distributions of NH₂, $P(E_{\text{int}}^{\text{NH}_2})$, coproduced with each selected CH₃ vibrational state are shown in Figure 3.5, where all results for the N–C bond cleavage following excitation to eight photoinitiated states of CH₃NH₂ are also presented. For the vibrationless CH₃ production pathway in Figure 3.5 (a), the NH₂ product coupled to CH₃($v = 0$) at the shorter three photolysis wavelengths (205.3, 211.0, and 212.8 nm) has undoubtedly two internal energy components, while the NH₂ internal energy distributions for the remaining five wavelengths (223.9, 230.4, 234.3, 236.3, and 239.9 nm) are somewhat indistinct. For discussion of the ratio between the fast and slow components, we practically first fitted the measured velocity distributions to two Gaussian functions, then converted the fitted curves to the energy scale shown in Figures 3.5 (a), (b). The fitting of the indistinct distribution measured at five longer photolysis wavelengths was conducted by same procedure, because the vibrational state-population (Figure 3.3) related to the internal energy distribution of the NH₂ counter-product by the energy conservation law was invariant for the photoinitiated states. On the other hand, the NH₂ counter-product of the CH₃($v_3 = 1$) fragment (Figure 3.5 (b)) has single component for 205–240 nm.

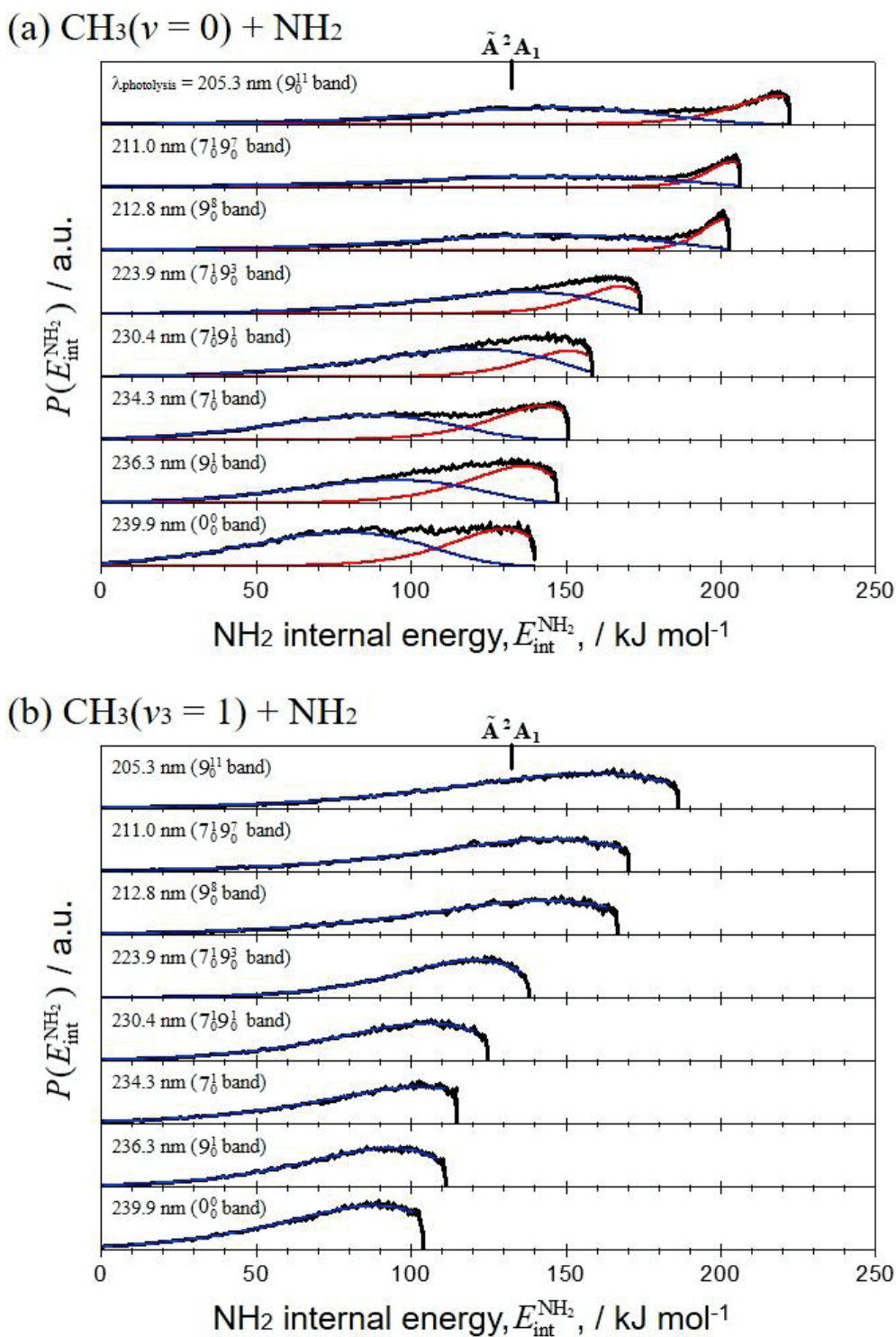


Figure 3.5 Internal energy distributions of the NH_2 product with the (a) $\text{CH}_3(\nu = 0)$ and (b) $\text{CH}_3(\nu_3 = 1)$ counter-product following excitation to eight photoinitiated states of CH_3NH_2 . The photoinitiated state and the photolysis wavelength are denoted in each frame. The energy position of the $\tilde{\text{A}}^2\text{A}_1$ excited state of NH_2 is shown for comparison.

3.3.3 Dispersed Fluorescence Spectra of $\text{NH}_2(\tilde{A}^2A_1)$

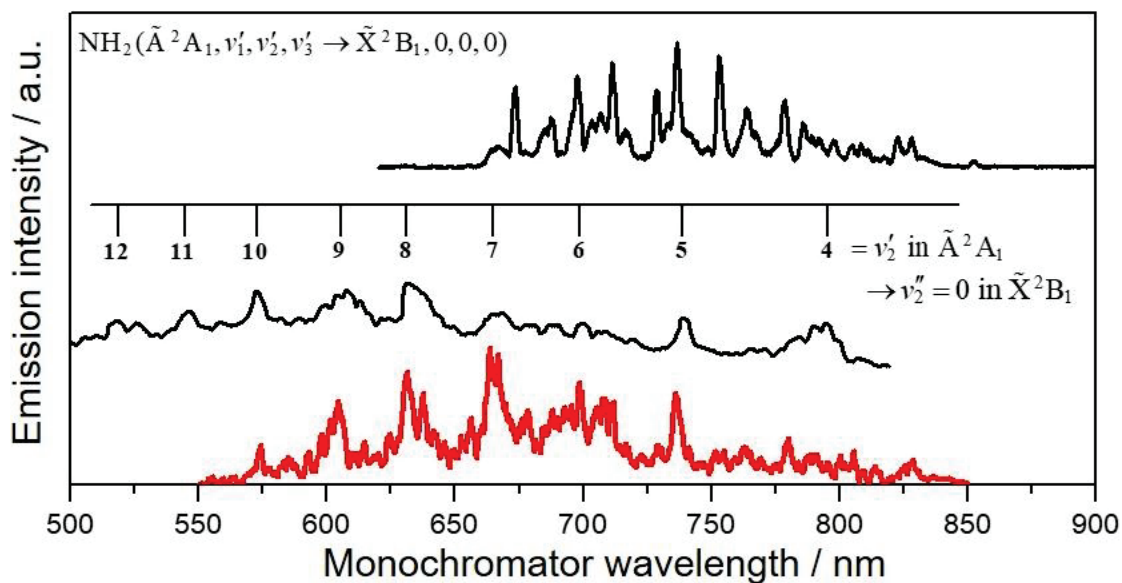


Figure 3.6 Dispersed fluorescence spectrum of the NH_2 photofragment in a gas cell experiment (bottom, red) at 212.8 nm. The calculated band positions associated with the ν_2 mode are shown. The variation of the detector sensitivity with respect to the wavelength is not corrected. The upper and the middle data are the NH_2 emission spectra of the NH_3 photolysis and the $\text{HN}_3 + \text{H}$ reaction, respectively. The upper and the bottom (CH_3NH_2 result) spectra were measured in the same setup in the present study for comparison. The middle spectrum is taken from Ref. 34. The assignments are appropriate to the linear configuration for the \tilde{A}^2A_1 state.

The emission spectrum measured at a photolysis wavelength of 212.8 nm in a quasi-static cell at room temperature is shown in Figure 3.6 (bottom, red). The spectral peaks were assigned to the vibronic structure of the $\tilde{A}^2A_1(0, \nu_2, 0) \rightarrow \tilde{X}^2B_1(0, 0, 0)$ electronic transition of NH_2 in the visible region, where ν_2 denotes a quantum number of the NH_2 bending mode. Because the $\text{NH}_2(\tilde{A}^2A_1, \nu_2 > 9)$ generation is energetically forbidden in the $\text{CH}_3\text{NH}_2(\nu = 0) + h\nu(212.8 \text{ nm})$ reaction, the observed peaks with $\nu_2 > 9$ indicate a certain contribution of the photodissociation of the vibrationally excited CH_3NH_2 sample thermally populated in

the cell. In addition, because photosensitivity of the whole detection system was not corrected for the observed wavelength region (550–850 nm), the vibrational-state distribution of the NH_2 ($\tilde{\text{A}}^2\text{A}_1$) product cannot be obtained from the spectrum. For comparison, we measured the dispersed fluorescence spectra of NH_2 in the NH_3 photodissociation at 193 nm using the same experimental setup (Figure 3.6, upper). The NH_2 emission spectrum in $\text{NH}_3 + h\nu \rightarrow \text{NH}_2(\tilde{\text{A}}^2\text{A}_1) + \text{H}$, which was previously measured under gas cell conditions,³² shows peaks in the high K_a state, indicating a -axis rotation of NH_2 as a result of the out-of-plane motion of the photoexcited NH_3 molecule with increasing N–H bond length.^{32,33} The NH_2 emission spectrum in the CH_3NH_2 photodissociation observed in the present study shows a marked difference from that of NH_3 ; the spectral peaks are well assigned to the signal emitted from the $K_a = 0$ state in the $\tilde{\text{A}}^2\text{A}_1$ state. This low K_a population of the NH_2 ($\tilde{\text{A}}^2\text{A}_1$) product is seen in previous studies on the HN_3 photolysis and the $\text{HN}_3 + \text{H} \rightarrow \text{NH}_2 + \text{N}_2$ reaction,^{34,35} to which we referred for the spectral assignment (Figure 3.6, middle).

We also conducted the emission measurements of NH_2 ($\tilde{\text{A}}^2\text{A}_1$) at the two photolysis wavelengths of 220.7 and 225.7 nm, which correspond to the $7_0^1 9_0^4$ and 9_0^4 vibronic bands, respectively. The energetically accessible ν_2 state of the nascent NH_2 ($\tilde{\text{A}}^2\text{A}_1$) fragment in the photodissociation of CH_3NH_2 changes from $\nu_2 = 9$ state to $\nu_2 = 5$ state as the photolysis wavelength increases from 212.8 nm to 225.7 nm. A series of spectra observed at the photolysis wavelengths of 212.8, 220.7 and 225.7 nm is presented in Figure 3.7 where the

energetic limits for formation of the $\text{NH}_2(\tilde{\text{A}}^2\text{A}_1)$ products are denoted as red broken lines. The population of the $\text{NH}_2(\tilde{\text{A}}^2\text{A}_1)$ product shifted toward the lower vibrational mode with decrease of the photon energy. The spectra show clearly the preferential population to the $K_a = 0$ state of the $\text{NH}_2(\tilde{\text{A}}^2\text{A}_1, v_2)$, irrespective of the photoinitiated states as same as the vibrational distribution of CH_3 (see Figure 3.3).

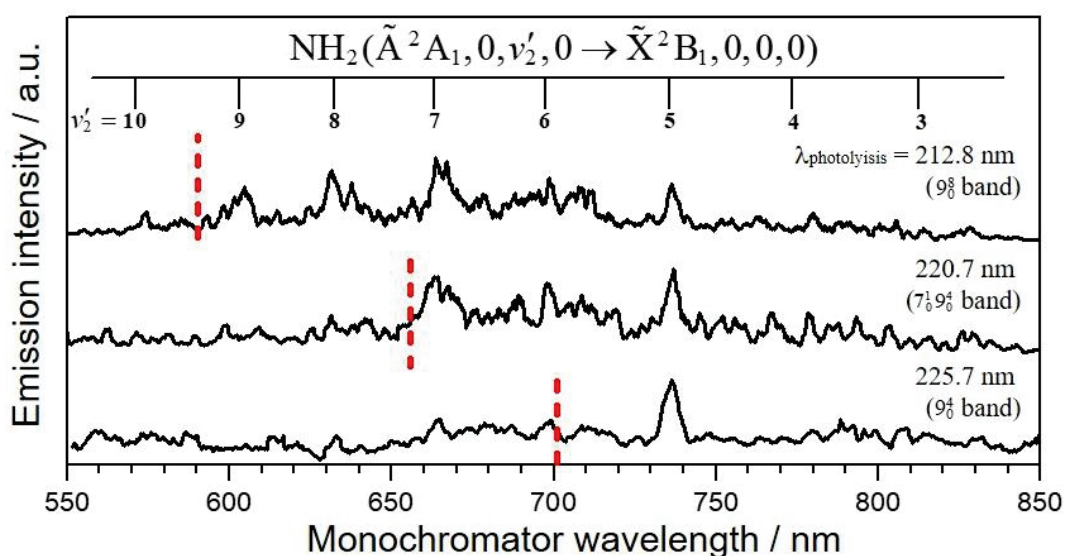


Figure 3.7 Dispersed spectra of the $\text{NH}_2(\tilde{\text{A}}^2\text{A}_1)$ photofragment at the photolysis wavelengths ($\lambda_{\text{photolysis}}$) of 212.8, 220.7 and 225.7 nm. The dissociation limit for each $\lambda_{\text{photolysis}}$ (red broken lines) is obtained from the energy conservation law ($h\nu = D(\text{CH}_3 - \text{NH}_2) + E_{\text{T}}^{\text{CH}_3} + E_{\text{T}}^{\text{NH}_2} + E_{\text{int}}^{\text{CH}_3} + E_{\text{int}}^{\text{NH}_2}$) where the $E_{\text{T}}^{\text{CH}_3}$, $E_{\text{T}}^{\text{NH}_2}$ and $E_{\text{int}}^{\text{CH}_3}$ are assumed to be zero. The value of 359.6 kJ/mol was used as $D(\text{CH}_3 - \text{NH}_2)$.

3.3.4 REMPI Spectra of the $\text{NH}(X^3\Sigma^-)$ Photofragments

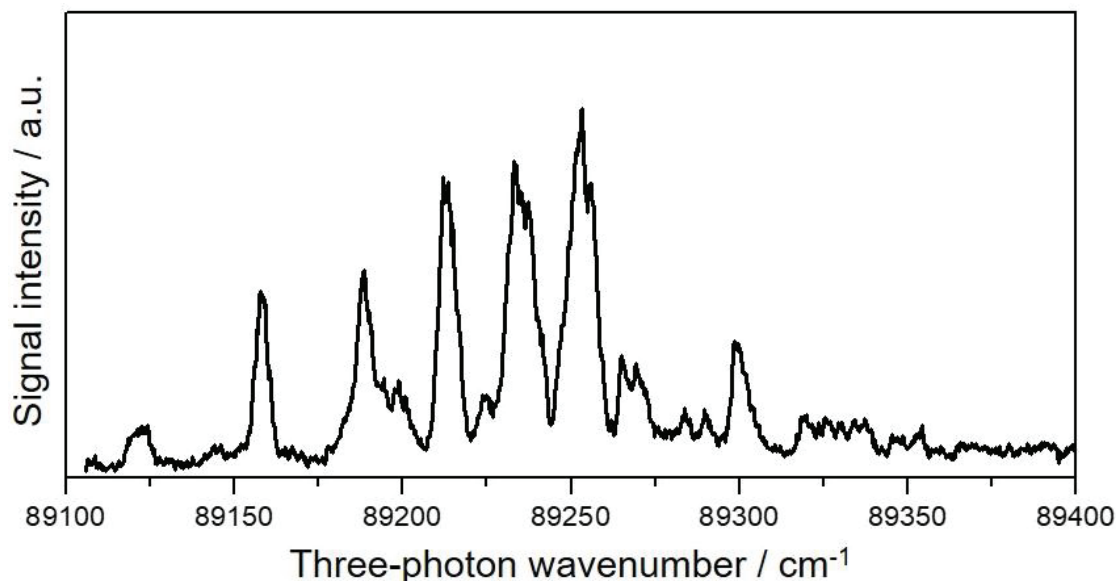


Figure 3.8 3 + 1 REMPI spectrum of the $\text{NH}(X^3\Sigma^-)$ photofragment in photodissociation following excitation to the 9_0^1 vibronic band.

Examples of the 3 + 1 REMPI spectra of the $\text{NH}(X^3\Sigma^-)$ product are shown in Figure 3.8. The spectrum is similar to that measured by Thomas *et al.*,¹⁸ where the rotational temperature was estimated to be $\sim 700\text{--}800$ K. We measured the $\text{NH}(X^3\Sigma^-)$ spectra at various photolysis wavelengths of 205–240 nm. The spectral appearance was insensitive with respect to the photoinitiated vibronic state of the parent CH_3NH_2 molecule. The calculated band position of (1,1) band on the $D^3\Pi-X^3\Sigma^-$ electronic transition would lie at ~ 338.3 nm.¹⁸ A signal attributed to the $\text{NH}(X^3\Sigma^-, \nu = 1)$ was not detected in this region. Generally, NH radicals in the $X^3\Sigma^-$ state and the metastable $a^1\Delta$ state are detected with the 2 + 1 REMPI scheme via the $B-X$ or $D-X$ electronic transitions^{36,37} and $d-a$ or $f-a$ electronic transitions,^{38,39} respectively. No signal corresponding to these transitions with 2 + 1 REMPI scheme could be identified definitively.

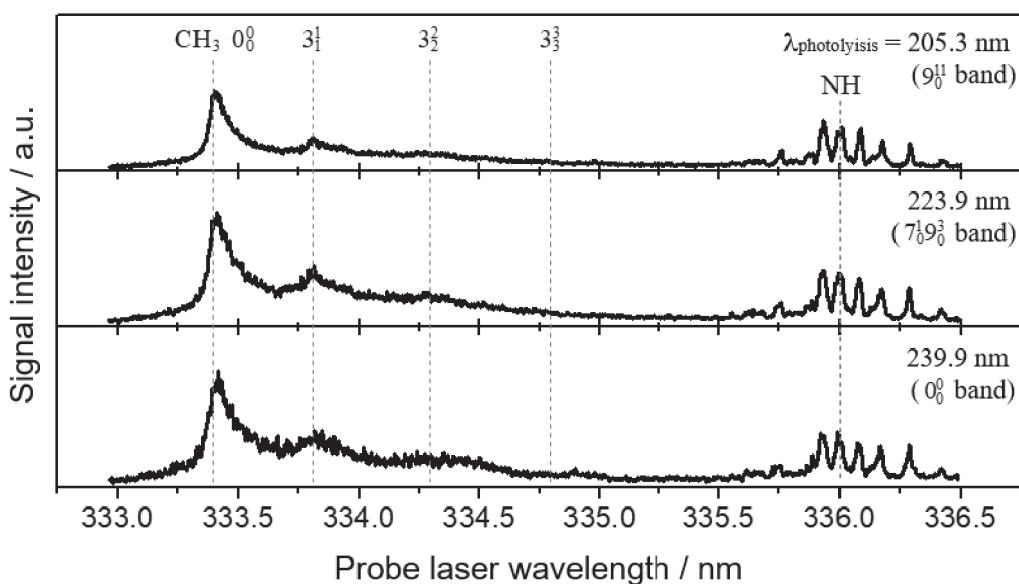


Figure 3.9 Wide-range REMPI survey spectra of nascent $m/z = 15$ products resulting from the photodissociation of methylamine at the photolysis wavelengths of 205.3 (top), 223.9 (middle), and 239.9 nm (bottom). Band positions for the 0_0^0 and $3_{v'}^{v''}$ ($v' = v'' = 1-3$) bands in the $3p^2A_2'' - \tilde{X}^2A_2'$ transition of the CH_3 radical and the $D^3\Pi - X^3\Sigma^-$ ($0,0$) band of the NH radical are indicated.

The wavelength region of the $D^3\Pi - X^3\Sigma^-$ ($0,0$) band in the $3 + 1$ REMPI scheme (~ 336 nm) is near that of the CH_3 $3p^2A_2'' - \tilde{X}^2A_2'$ transition (~ 333 nm). We measured REMPI spectra over both detection region for $NH(X^3\Sigma^-)$ and CH_3 radicals. Figure 3.9 shows the wide-range REMPI spectra following photoexcitation at 205.3, 223.9 and 239.9 nm. The relative yield of the $NH(X^3\Sigma^-)$ products with respect to the CH_3 ($v_3 = 0-3$) fragments, $\Phi(\lambda_{\text{photolysis}})$, is estimated by

$$\Phi(\lambda_{\text{photolysis}}) = \frac{S(NH)}{S(NH) + S(CH_3)},$$

where $S(NH)$ and $S(CH_3)$ is the spectral area obtained by integrating over the NH (335.5–336.5 nm) and CH_3 ($v_3 = 0-3$) (333.0–335.0 nm) signal regions, respectively. The values of

$\Phi(\lambda_{\text{photolysis}})$ which are listed in Table 3.2, were invariant (~ 0.2) for the photoinitiated state of CH_3NH_2 .

Table 3.2 Selected vibronic bands of the parent CH_3NH_2 molecule, the corresponding photoexcitation wavelength, and relative yield ($\Phi(\lambda_{\text{photolysis}})$) of the $\text{NH}(\text{X}^3\Sigma^-)$ products with respect to the CH_3 ($\nu_3 = 0-3$) products evaluated from Eq. (3.1).

$\lambda_{\text{photolysis}} / \text{nm}$	Vibronic state	$\Phi(\lambda_{\text{photolysis}})$
205.3	9_0^{11}	0.22
211.0	$7_0^1 9_0^{11}$	0.25
212.8	9_0^8	0.24
223.9	$7_0^1 9_0^3$	0.19
230.4	$7_0^1 9_0^1$	0.21
234.3	7_0^1	0.21
236.3	9_0^1	0.22
239.9	0_0^0	0.17

3.3.5 Scattering Images of the $\text{NH}(\text{X}^3\Sigma^-)$ Products

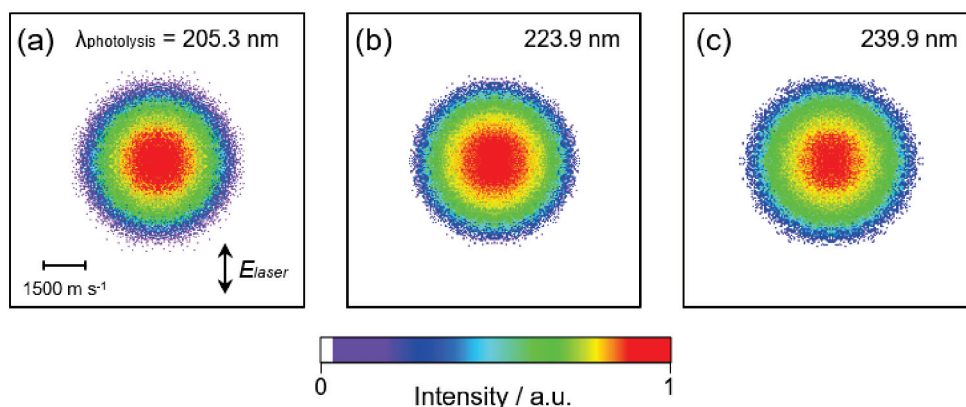


Figure 3.10 Observed scattering raw images of the NH product from the CH_3NH_2 photodissociation at the photolysis wavelength of (a) 205.3 nm, (b) 223.9 nm, and (c) 239.9 nm. The laser polarization direction is vertical on the figures and is described by an arrow.

The scattering images of the $\text{NH}(\text{X}^3\Sigma^-)$ product observed at the probe wavelength of 336 nm are shown in Figure 3.10: the photolysis wavelength of (a) 205.3 nm, (b) 223.9 nm, and (c) 239.9 nm. These images display similar velocity and isotropic angular distributions. The center-of-mass translational energy distributions, $P(E_{\text{T}}^{\text{NH}})$, extracted from the scattering images are shown in Figure 3.11. The $P(E_{\text{T}}^{\text{NH}})$ exhibits the single component, irrespective of the photolysis wavelength. On the basis of the fact that the counter-product is energetically the CH_4 molecule as mentioned in previous work,^{16,18} we applied the counter-product analysis to the $P(E_{\text{T}}^{\text{NH}})$ to obtain the internal energy distribution of the CH_4 counter-product, $P(E_{\text{int}}^{\text{CH}_4})$, where the $E_{\text{int}}^{\text{CH}_4}$ was determined by the energetic restriction: $h\nu = \Delta H^\circ + E_{\text{T}}^{\text{NH}} + E_{\text{T}}^{\text{CH}_4} + E_{\text{int}}^{\text{NH}} + E_{\text{int}}^{\text{CH}_4}$. The value of the standard enthalpy of formation ($\Delta H^\circ = 318.7 \text{ kJ/mol}$)¹⁶ was used, and the rotational energy in the $E_{\text{int}}^{\text{NH}}$ was

neglected in the evaluation. The evaluated $E_{\text{int}}^{\text{CH}_4}$ corresponds to the upper scale in Figure 3.11. The available energy $E_{\text{avl}} = hv - \Delta H^\circ$, the averaged translational energy of the NH ($X^3\Sigma^-$) product ($\langle E_{\text{T}}^{\text{NH}} \rangle$), and the averaged internal energy of the CH₄ counter-product ($\langle E_{\text{int}}^{\text{CH}_4} \rangle$) are summarized in Table 3.3. The 85 % of the E_{avl} was partitioned into the $E_{\text{int}}^{\text{CH}_4}$ in all photolysis wavelengths, indicating that the CH₄ product in the highly internal excited-states is generated.

Table 3.3 Vibronic bands used to initially photoexcitation of CH₃NH₂, available energy (E_{avl}), averaged NH translational and CH₄ internal energies ($\langle E_{\text{T}}^{\text{NH}} \rangle$ and $\langle E_{\text{int}}^{\text{CH}_4} \rangle$), and the fraction of $\langle E_{\text{int}}^{\text{CH}_4} \rangle$ for E_{avl} .

Band	E_{avl} / kJ mol ⁻¹	$\langle E_{\text{T}}^{\text{NH}} \rangle$ / kJ mol ⁻¹	$\langle E_{\text{int}}^{\text{CH}_4} \rangle$ / kJ mol ⁻¹	$f = \langle E_{\text{int}}^{\text{CH}_4} \rangle / E_{\text{avl}}$ %
9_0^1	264.0	18.7	227.8	86.3
$7_0^1 9_0^1$	248.2	18.2	212.9	85.8
9_0^8	243.4	18.0	208.6	85.7
$7_0^1 9_0^3$	215.6	18.0	180.8	83.8
$7_0^1 9_0^1$	200.5	15.9	169.7	84.7
7_0^1	191.9	14.3	164.2	85.6
9_0^1	187.6	13.9	160.6	85.6
0_0^0	180.0	13.3	154.1	85.6

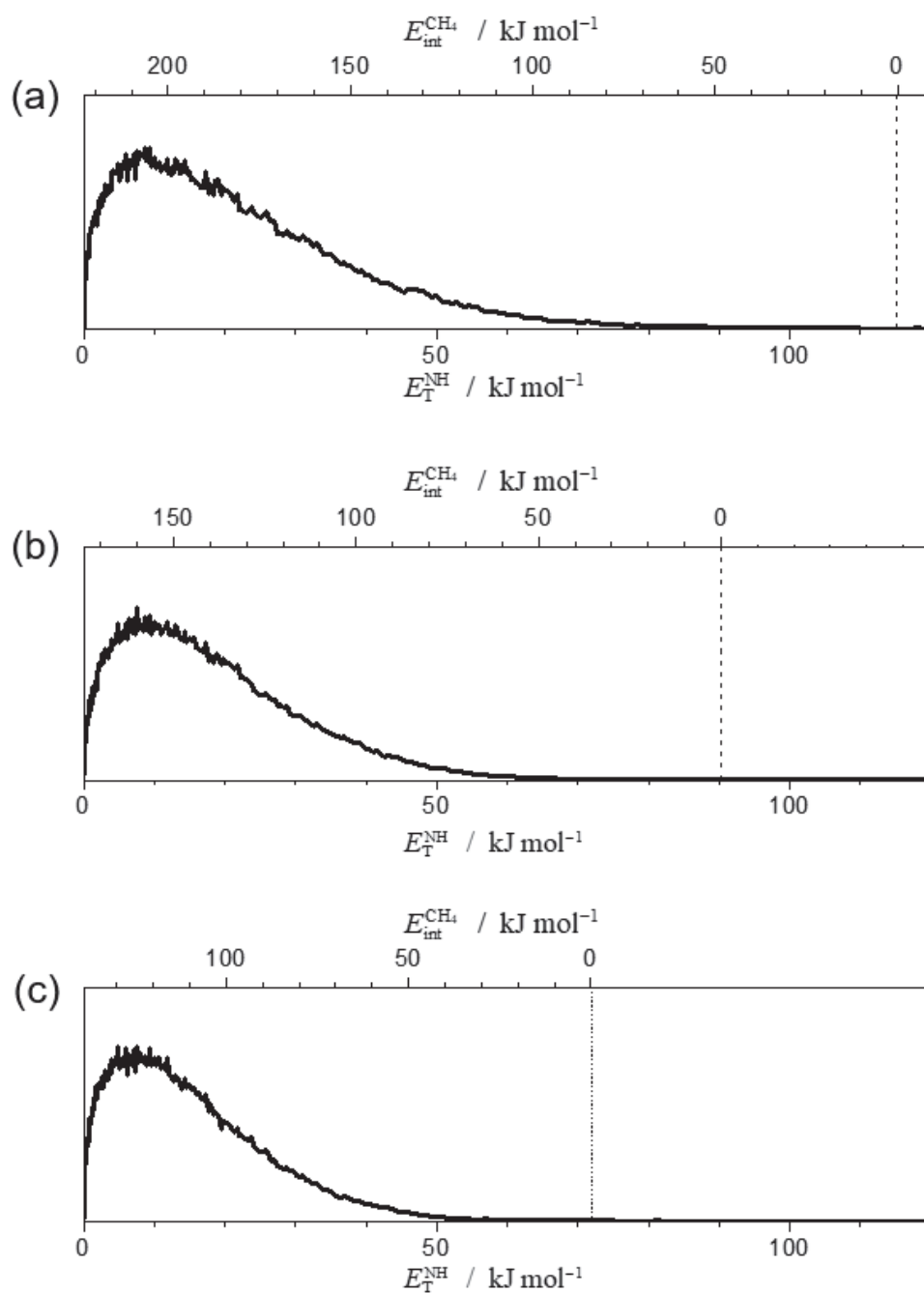


Figure 3.11 Center-of-mass translational energy distributions extracted from the scattering images of the NH fragment at the photolysis wavelength of (a) 205.3 nm, (b) 223.9 nm, and (c) 239.9 nm. The upper scale indicates the internal energy of the CH₄ counter-product evaluated through the energy conservation law, $h\nu = \Delta H^{\circ} + E_{\text{T}}^{\text{NH}} + E_{\text{T}}^{\text{CH}_4} + E_{\text{int}}^{\text{NH}} + E_{\text{int}}^{\text{CH}_4}$. Broken lines denote the energetic limit.

3.4 Discussion

The $P(E_{\text{int}}^{\text{NH}_2})$ distribution (Figure 3.5) demonstrates that the NH_2 product is highly internally excited; the NH_2 fragment has high enough internal energy to populate the $\tilde{\text{A}}^2\text{A}_1$ excited state, whose term energy is superimposed in the plot. Because the broader components of $P(E_{\text{int}}^{\text{NH}_2})$, which are coupled to both vibrational ground and excited CH_3 fragments, are distributed across the energy threshold for the $\text{NH}_2(\tilde{\text{A}}^2\text{A}_1)$ production, these components are reasonably ascribed to $\text{CH}_3 + \text{NH}_2(\tilde{\text{X}}^2\text{B}_1)$ with substantially high vibrational and/or rotational excitation. Conversely, the narrower component, which is observed only with the $\text{CH}_3(\nu = 0)$ counter-product, is interpreted as the result of the $\text{CH}_3 + \text{NH}_2(\tilde{\text{A}}^2\text{A}_1)$ product pathway because most of the corresponding NH_2 internal energy is above the threshold. We conjecture that the branching to the $\text{CH}_3 + \text{NH}_2(\tilde{\text{A}}^2\text{A}_1)$ and $\text{CH}_3 + \text{NH}_2(\tilde{\text{X}}^2\text{B}_1)$ asymptotes occurs around the conical intersection in the CH_3NH_2 photodissociation, as is the case in the $\text{NH}_3 + h\nu \rightarrow \text{NH}_2(\tilde{\text{A}}^2\text{A}_1) + \text{H} / \text{NH}_2(\tilde{\text{X}}^2\text{B}_1) + \text{H}$ reaction.

The internal energy distribution is revealed by the counter-product analysis. However, the product state ($\tilde{\text{A}}^2\text{A}_1$ or $\tilde{\text{X}}^2\text{B}_1$) is unambiguously determined by spectroscopy. Generation of the $\text{NH}_2(\tilde{\text{A}}^2\text{A}_1)$ product in the CH_3NH_2 photodissociation was not experimentally established in previous dynamics studies, where analysis based on the energetic constraint led to the opposite conclusions. Kinetic energy release measured by Waschewsky *et al.* gives $E_{\text{T}}^{\text{CH}_3} + E_{\text{T}}^{\text{NH}_2}$, hence, the $E_{\text{int}}^{\text{CH}_3} + E_{\text{int}}^{\text{NH}_2}$ distribution,¹¹ whereas the

REMPI spectroscopy employed by Thomas *et al.* provides the details of the $E_{\text{int}}^{\text{CH}_3}$ distribution.¹³ There is no consistency between the explanations provided in these studies because each discussion of the electronic-state distribution of NH_2 was indirectly made by assuming a uniform electronic behavior of the CH_3 and NH_2 product pairs. The $E_{\text{int}}^{\text{NH}_2}$ distribution obtained by our state-resolved scattering experiment indicates the state-specific generation of the $\text{NH}_2(\tilde{\text{A}}^2\text{A}_1)$ product with the $\text{CH}_3(v=0)$ counter-product. The dispersed fluorescence spectra (Figures 3.6 and 3.7) provide direct evidence of the $\text{NH}_2(\tilde{\text{A}}^2\text{A}_1)$ generation in the CH_3NH_2 photodissociation at 212.8, 220.7, and 225.7 nm, which corresponds to the excitation wavelength of the 9_0^8 , $7_0^1 9_0^4$, and 9_0^4 vibronic bands, respectively.²⁴ We consider that the carrier of the $\tilde{\text{A}}^2\text{A}_1 \rightarrow \tilde{\text{X}}^2\text{B}_1$ emission of NH_2 is the low kinetic energy component observed in the $\text{CH}_3(v=0)$ scattering data. Because the generation of the $\text{NH}_2(\tilde{\text{A}}^2\text{A}_1)$ product is coupled to the vibrationless CH_3 counter-product, the highly vibrational excitation of the overall CH_3 products, which were observed over the photolysis wavelength range of 222–240 nm by Thomas *et al.*¹³ in agreement with the REMPI spectrum at 205.3 nm (Figure 3.2), does not violate the energetic constraint. The present state-resolved measurement and analysis illuminate the product pathway of $\text{CH}_3\text{NH}_2 + h\nu \rightarrow \text{CH}_3 + \text{NH}_2(\tilde{\text{A}}^2\text{A}_1)$, retaining consistency with the previous experimental studies.

A peculiar generation mechanism is necessary for generating the electronically excited NH_2 and the vibrationally unexcited CH_3 product pair. A novel mechanism of the N–C bond fission was proposed by Thomas *et al.* on the basis of the observed vibrational-state

distribution of the CH₃ fragment; the internally excited CH₃NH₂, which is generated in the S₀ PES by non-adiabatic transition from the S₁ state through the conical intersection along the N–H bond ($R_{\text{N-H}} = 1.925 \text{ \AA}$),¹⁶ is ultimately dissociated to CH₃ + NH₂.¹³ In this mechanism, the conical intersection in the long-range region plays a significant role when the departing H atom returns to the CH₃NH radical moiety, explaining the generation of the highly vibrationally excited CH₃ fragment. We consider that the internally energized CH₃NH₂ can also visit another conical intersection region associated with the N–C bond ($R_{\text{N-C}} = 2.496 \text{ \AA}$),¹⁶ whose energy (428.3 kJ/mol) was theoretically calculated to be lower than that associated with the N–H bond (486.2 kJ/mol).¹⁶ In addition, the substantially high kinetic energy of 96 kJ/mol is given to the conical intersection of the N–H elongated geometry at the photolysis wavelength of 205.3 nm (582.7 kJ/mol). After visiting the N–H conical intersection, a portion of the trajectories of the internally excited CH₃NH₂ is expected to extend to the N–C conical intersection region, where the system can branch to the CH₃ + NH₂ ($\tilde{\text{A}}^2\text{A}_1$) pathway at a certain probability. The long-range dynamics likely exhibit the product-state distribution reflecting the large-amplitude motion with the CNH₂ planar geometry at the conical intersection.¹⁶ The observed isotropic angular distribution (Figure 3.4 (a)) supports complex nuclear motions prior to the dissociation rather than a direct mechanism. This interpretation is consistent with the observed emission spectra of the NH₂ ($\tilde{\text{A}}^2\text{A}_1$) product showing the low K_a excitation; the a -axis rotation of NH₂ is correlated to the out-of-plane motion of the dissociating CH₃NH₂. The ν_2 excitation of the

$\text{NH}_2(\tilde{\text{A}}^2\text{A}_1)$ product can be a result of the geometrical rearrangement from the bend NH_2 moiety of the dissociating CH_3NH_2 to the linear equilibrium structure of the electronically excited NH_2 radical.

The branching ratio between the electronically excited- and ground-state adiabatic pathways in the ammonia and CH_3NH_2 photodissociations has been discussed in connection with the dynamics around the conical intersections in the long-range region. Through theoretical and experimental investigations, the branching ration of the $\text{NH}_3 + h\nu \rightarrow \text{H} + \text{NH}_2(\tilde{\text{A}}^2\text{A}_1) / \text{NH}_2(\tilde{\text{X}}^2\text{B}_1)$ reaction was estimated at 0.06–0.35^{2-4,7,32,40} and depended on the photoinitiated vibronic band of $\text{NH}_3(\tilde{\text{A}}^1\text{A}_2'')$. For the N–H bond fission channel of CH_3NH_2 , the generation of the $\text{CH}_3\text{NH}(\tilde{\text{A}}^2\text{A}')$ product was indicated in the H atom tagging measurement by Reed and coworkers.¹⁰ Although the branching ratio of the $\text{H} + \text{CH}_3\text{NH}(\tilde{\text{A}}^2\text{A}') / \text{CH}_3\text{NH}(\tilde{\text{X}}^2\text{A}'')$ pathways was not quantified, the slower component in the bimodal kinetic energy spectra, which was ascribed to be due to the direct dissociation on the S_1 PES adiabatically correlating to $\text{H} + \text{CH}_3\text{NH}(\tilde{\text{A}}^2\text{A}')$, displayed a considerable portion of the relative intensity. The slow H product was similarly observed by Ahn *et al.* in the velocity-mapping imaging study with the ratios to the faster component of 0.38–0.78.⁹ However, the $\text{H} + \text{CH}_3\text{NH}(\tilde{\text{A}}^2\text{A}')$ pathway was excluded from their discussion because the photon energy was lower than the energy threshold. We roughly estimated the branching ratio of the $\text{CH}_3 + \text{NH}_2(\tilde{\text{A}}^2\text{A}_1) / \text{NH}_2(\tilde{\text{X}}^2\text{B}_1)$ pathways at ~ 0.1 from the scattering data and the vibrational-state distribution of the CH_3 product. The estimation based on the dispersed

fluorescence spectrum of NH_2 ($\tilde{\text{A}}^2\text{A}_1$) observed at 212.8 nm includes large errors; comparison of the spectral intensities between the CH_3NH_2 and NH_3 photodissociation results yields a much smaller branching ratio than 0.1 with any assumptions for the gas cell condition. A small contribution of the $\text{CH}_3 + \text{NH}_2$ ($\tilde{\text{A}}^2\text{A}_1$) pathway may be explained by the long-range dynamics proposed by Thomas *et al.*¹³ If we assume a large-amplitude motion reaching the conical intersection associated with the N—C bond driven by stretching / returning of the N—H bond, then the system has enough reaction time for the non-adiabatic transition to the ground-state products to occur efficiently, resulting in a small survival probability on the upper adiabatic state.

It is noted that the direct N—C bond dissociation on the S_1 PES, which is not included in the above discussion, is another possible mechanism of the NH_2 ($\tilde{\text{A}}^2\text{A}_1$) generation. The barrier height of the N—C bond cleavage on the S_1 PES was predicted theoretically to be 539, and 556 kJ/mol with zero-point energy corrected.^{16,17} The smaller value of 539 kJ/mol corresponds to the long-wavelength threshold of 221.9 nm for dissociation to the $\text{CH}_3 + \text{NH}_2$ pathway. The vibrational state-population of the CH_3 product in 205–240 nm (Figure 3.3) obtained in present study showed no significant threshold behavior for the direct dissociation on the S_1 surface, and the dispersed fluorescence spectrum were observed at the longer wavelength of 225.7 nm (Figure 3.7, bottom) than the wavelength threshold of 221.9 nm; therefore, the S_1 direct mechanism is omitted. The exclusion of this mechanism is consistent with the preference of N—H bond elongation to N—C bond cleavage on the S_1

surface of CH_3NH_2 , which established in early studies.^{15,41-43} The large-amplitude deformation from the long $R_{\text{N-H}}$ region to the long $R_{\text{N-C}}$ region in the dissociation mechanism will be corroborated in future theoretical and experimental works.

The relative yields of the NH photoproducts to the CH_3 photofragments in the photodissociation ($\Phi(\lambda_{\text{photolysis}})$) (Table 3.2), were insensitive to the photoinitiated vibronic bands of the parent CH_3NH_2 molecule. The NH ($X^3\Sigma^-$) production is expected to be initiated from the internally excited CH_3NH_2 in the S_0 state which is prepared through the conical intersection associated with the N-H bond cleavage as same as the N-C bond cleavage dynamics mentioned above. If the NH production and the N-C bond dissociation channels proceed from only the S_0 surface of CH_3NH_2 , the $\Phi(\lambda_{\text{photolysis}})$ (~ 0.2) determined experimentally in the present study can be interpreted as the branching ratio of the NH ($X^3\Sigma^-$) + CH_4 channel for the CH_3 + NH_2 pathway. Thomas *et al.* suggested the photoinitiated state dependence of the NH production yield; the excitation on the 9_0^1 and 7_0^1 bands leads to 2.1 and 1.4 times more NH ($X^3\Sigma^-$) than that on the 0_0^0 band.¹⁸ We speculate that this dependence is reasonably explained by the effect of the photoinitiated motion of CH_3NH_2 on the probability of the $S_1 \rightarrow S_0$ internal conversion in vicinity of the conical intersection along the N-H bond. Namely, the excitation to the 9_0^1 and 7_0^1 bands facilitates the $S_1 \rightarrow S_0$ internal conversion in comparison with that to 0_0^0 band. The photoinitiated state-dependence on the yield of the CH_3 photoproduct, which cannot be determined in present study, should be measured to justify this speculation.

The ~85 % of E_{avl} was partitioned into the $E_{\text{int}}^{\text{CH}_4}$. The local structure at the transition state on the T_1 surface shown in Figure 3.12, which was found theoretically by Xiao *et al.*,¹⁶ allows us to estimate the generation of the highly vibrational excited CH_4 . The bond length of the C–H bond, whose H atom is located between the N and C atoms, is 1.41 Å which is longer than the other C–H bond distances at ~1.08 Å; therefore, the nascent CH_4 molecule would be vibrationally excited in the C–H stretch mode(s). Further experiments and complimentary theoretical works are undoubtedly required to identify the NH production mechanism in the photodissociation of CH_3NH_2 . Experiments to determine the rotational state-distribution of the $\text{NH}(\text{X}^3\Sigma^-)$ and to examine the generation of the metastable NH ($a^1\Delta$) product are in progress.

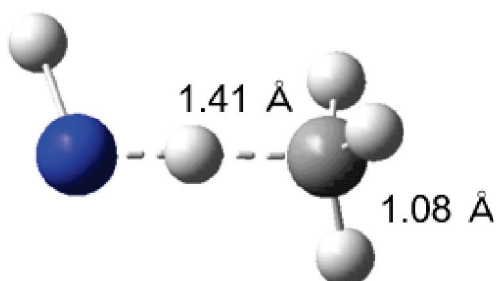


Figure 3.12 Local structure at the transition state on T_1 surface in the NH production channel. The structural parameters are taken from Ref. 16. The lengths of the newly forming C–H bond and a C–H bond of methyl moiety are shown.

3.5 Conclusion

The nascent state-distribution and the state-resolved scattering distribution of the CH₃ photofragment in the CH₃NH₂ photodissociation were measured over the $S_1 - S_0$ absorption band (205–240 nm). The CH₃ fragment produced in the vibrational ground state specifically shows bimodal kinetic energy release, whose lower energy component is the counter-product of NH₂ (\tilde{A}^2A_1). This assignment is based on dispersed fluorescence spectroscopic analysis performed on the NH₂ fragment. The spectral peaks are unambiguously characterized to the vibronic structure associated with the $\tilde{A}^2A_1 \rightarrow \tilde{X}^2B_1$ transition, providing experimental evidence of the generation of NH₂ (\tilde{A}^2A_1) has been so far discussed by analogy with ammonia photochemistry. The state-specificity of this pathway found in the present study reveals the significance of the large-amplitude dynamics in the long-range regions, which includes the conical intersection.

The state-selective ion-imaging was applied to the NH ($X^3\Sigma^-$) production channel. The relative yield of the NH photoproduct with respect to the CH₃ fragment showed no dependence on the photoinitiated state of CH₃NH₂. The counter-product analysis of the observed image revealed that the nascent CH₄ counter-product of the NH ($X^3\Sigma^-$) product is internally excited. The data obtained in the present study supports the mechanism including the S_1 , S_0 , and T_1 surfaces, which has been proposed in the previous theoretical and experimental study; however, the elucidation of the detailed dynamics demands necessarily further experimental and theoretical studies.

3.6 References

1. J. Biesner, L. Schnieder, J. Schmeer, G. Ahlers, X. Xie, K. H. Welge, M. N. R. Ashfold and R. N. Dixon, *J. Chem. Phys.* **88**, 3607 (1988).
2. J. Biesner, L. Schnieder, G. Ahlers, X. Xie, K. H. Welge, M. N. R. Ashfold and R. N. Dixon, *J. Chem. Phys.* **91**, 2901 (1989).
3. M. N. R. Ashfold, R. Dixon, M. Kono, D. H. Mordaunt and C. L. Reed, *Philos. Trans. R. Soc. London, Ser. A* **355**, 1659 (1997).
4. J. D. Rodríguez, M. G. González, L. Rubio-Lago and L. Bañares, *Phys. Chem. Chem. Phys.* **16**, 406 (2014).
5. M. N. R. Ashfold, C. L. Bennett and R. N. Dixon, *Chem. Phys.* **93**, 293 (1985).
6. M. I. McCarthy, P. Rosmus, H. -J. Werner, P. Botschwina and V. Vaida, *J. Chem. Phys.* **86**, 6693 (1987).
7. J. Ma, C. Xie, X. Zhu, D. R. Yarkony, D. Xie and H. Guo, *J. Phys. Chem. A* **118**, 11926 (2014).
8. D.-S. Ahn, J. Lee, Y. C. Park, Y. S. Lee and S. K. Kim, *J. Chem. Phys.* **136**, 024306 (2012).
9. D.-S. Ahn, J. Lee, J.-M. Choi, K.-S. Lee, S. J. Baek, K. Lee, K.-K. Baeck and S. K. Kim, *J. Chem. Phys.* **128**, 224305 (2008).
10. C. L. Reed, M. Kono and M. N. R. Ashfold, *J. Chem. Soc. Faraday Trans.* **92**, 4897 (1996).
11. G. C. G. Waschewsky, D. C. Kitchen, P. W. Browning and L. J. Butler, *J. Phys. Chem.* **99**, 2635 (1995).
12. M. Epshtein, A. Portnov and I. Bar, *Phys. Chem. Chem. Phys.* **17**, 19607 (2015).
13. J. O. Thomas, K. E. Lower and C. Murray, *J. Phys. Chem. A* **118**, 9844 (2014).
14. R. Marom, T. Weiss, S. Rosenwaks and I. Bar, *J. Chem. Phys.* **132**, 244310 (2010).
15. J. V. Michael and W. A. Noyes, *J. Am. Chem. Soc.* **85**, 1228 (1963).
16. H. Xiao, S. Maeda and K. Morokuma, *J. Phys. Chem. A* **117**, 5757 (2013).
17. K. M. Dunn and K. Morokuma, *J. Phys. Chem.* **100**, 123 (1996).
18. J. O. Thomas, K. E. Lower and C. Murray, *J. Phys. Chem. Lett.* **3**, 1341 (2012).
19. D. Townsend, S. A. Lahankar, S. K. Lee, S. D. Chambreau, A. G. Suits, X. Zhang, J. Rheinecker, L. B. Harding and J. M. Bowman, *Science* **306**, 1158 (2004).
20. A. G. Suits, *Acc. Chem. Res.* **41**, 873 (2008).
21. M. P. Grubb, M. L. Warter, A. G. Suits and S. W. North, *J. Phys. Chem. Lett.* **1**, 2455 (2010).
22. H. Xiao, S. Maeda and K. Morokuma, *J. Phys. Chem. Lett.* **2**, 934 (2011).
23. M. -J. Hubin-Franskin, J. Delwiche, A. Giuliani, M. -P. Ska, F. Motte-Tollet, I. C. Walker, N. J. Mason, J. M. Gingell and N. C. Jones, *J. Chem. Phys.* **116**, 9261 (2002).
24. M. Tsuboi, A. Y. Hirakawa and H. Kawashima, *J. Mol. Spectrosc.* **29**, 216 (1969).
25. J. W. Hudgens, T. G. DiGiuseppe and M. C. Lin, *J. Chem. Phys.* **79**, 571 (1983).
26. R. Schott, J. Schlütter, M. Olzmann and K. Kleineremanns, *J. Chem. Phys.* **102**, 8371 (1995).

27. *Handbook of Chemistry: Pure Chemistry, 5th ed.*, (Maruzen Publishing Co., 2004).
28. B. Zhang, J. Zhang and K. Liu, *J. Chem. Phys.* **122**, 104310 (2005).
29. H. B. Fu, Y. J. Hu and E. R. Bernstein, *J. Chem. Phys.* **123**, 234307 (2005).
30. *NIST Chemistry WebBook, NIST Standard Reference Database Number 69*, National Institute of Standards and Technology, Gaithersburg MD, 20899, P.J. Linstrom and W.G. Mallard edn.
31. M. Sumida, Y. Kohge, K. Yamasaki and H. Kohguchi, *J. Chem. Phys.* **144**, 064304 (2016).
32. V. M. Donnelly, A. P. Baronavski and J. R. McDonald, *Chem. Phys.* **43**, 271 (1979).
33. E. L. Woodbridge, M. N. R. Ashfold and S. R. Leone, *J. Chem. Phys.* **94**, 4195 (1991).
34. O. Kajimoto, T. Kawajiri and T. Fueno, *Chem. Phys. Lett.* **76**, 315 (1980).
35. K. Yamasaki, A. Watanabe, I. Tokue and Y. Ito, *Chem. Phys. Lett.* **204**, 106 (1993).
36. S. G. Clement, M. N. R. Ashfold, C. M. Western, R. D. Johnson and J. W. Hudgens, *J. Chem. Phys.* **97**, 7064 (1992).
37. S. G. Clement, M. N. R. Ashfold, C. M. Western, R. D. Johnson and J. W. Hudgens, *J. Chem. Phys.* **96**, 5538 (1992).
38. M. N. R. Ashfold, S. G. Clement, J. D. Howe and C. M. Western, *J. Chem. Soc. Faraday Trans.* **87**, 2515 (1991).
39. R. D. Johnson and J. W. Hudgens, *J. Chem. Phys.* **92**, 6420 (1990).
40. J. Ma, X. Zhu, H. Guo and D. R. Yarkony, *J. Chem. Phys.* **137**, 22A541 (2012).
41. S. J. Baek, K. -W. Choi, Y. S. Choi and S. K. Kim, *J. Chem. Phys.* **117**, 10057 (2002).
42. S. J. Baek, K. -W. Choi, Y. S. Choi and S. K. Kim, *J. Chem. Phys.* **118**, 11026 (2003).
43. S. J. Baek, K. -W. Choi, Y. S. Choi and S. K. Kim, *J. Chem. Phys.* **118**, 11040 (2003).

Chapter 4

Photodissociation Dynamics of Trimethylamine

4.1 Introduction

Electronic excitations of amines ($\text{NR}^1\text{R}^2\text{R}^3$) due to ultraviolet (UV) photoabsorption are expressed as electron promotion from a lone-pair orbital to a Rydberg orbital of the nitrogen atom. Therefore, despite the wide variety of possible alkyl groups (R) for amines, amine photochemistry is generally explained by Rydberg state dynamics.¹ For aliphatic amines, the first (S_1) and second (S_2) excited states predominantly have $3s$ and $3p$ Rydberg characters, respectively. Valence character is involved as a result of mixing of an anti-bonding $\sigma_{\text{N-R}}^*$ state. As was exemplified in previous NH_3 photochemistry studies,²⁻⁹ the electronic interactions of the $\sigma_{\text{N-R}}^*$ state with the $3s$ Rydberg state and with the ground state form a reaction barrier and a conical intersection on the S_1 potential energy surface (PES), respectively. The predissociative features of NH_3 photochemistry are well explained by this reaction barrier in the outer Franck-Condon region, and branching of the product pathways ($\rightarrow \text{NH}_2(\tilde{\text{A}}^2\text{A}_1) + \text{H}$, and $\rightarrow \text{NH}_2(\tilde{\text{X}}^2\text{B}_1) + \text{H}$) is established to be due to the exit conical intersection. Similar PES structures to those of NH_3 are expected for small amines. Indeed, the photodissociation dynamics of methylamine (CH_3NH_2), which is the simplest NH_3 -derivative species, are interpreted analogously to NH_3 photochemistry.⁹⁻²²

Aliphatic amines are further grouped into primary-, secondary-, or tertiary-amines. For tertiary aliphatic amines (TAAs), direct optical preparation of the S_1 state is characterized by a highly fluorescent property. Typical TAAs are observed to have nearly unity of fluorescence quantum yield in the S_1 - S_0 band. The fluorescence significantly decreases over

the short wavelengths, where the S_2-S_0 absorption overwhelms the S_1-S_0 band.²³⁻²⁵ On the other hand, internal conversion between the Rydberg states plays a dominant role in S_2 photochemistry in the ~ 200 nm region. The ultrafast dynamics of various TAAs have been investigated by time-resolved spectroscopy.²⁶⁻³¹ Change from the efficiently fluorescent behavior to the ultrafast electronic relaxation is regarded as a common feature of TAA photochemistry as the photoabsorption shifts from the S_1-S_0 to the S_2-S_0 bands. However, since wavelength dependence of dissociation is comparably less known, these understandings of the excited state dynamics in the Franck-Condon region are not well linked to elucidation of the photodissociation dynamics.³²

Trimethylamine ($N(CH_3)_3$, TMA) is the simplest of the TAAs. The radiative decay, non-radiative decay, and dissociation of TMA have been investigated as a pertinent model system for examining dynamical interactions between the electronic excited states of a polyatomic molecule.^{23,30-35} The UV absorption spectrum of TMA consists of two unseparated broad bands, and this feature is commonly observed in TAA spectra.^{23,24,31,36} A strong peak (maximum at ~ 200 nm) and a weak feature (maximum at ~ 230 nm) are traditionally assigned to the $S_2(3p)-S_0$ and $S_1(3s)-S_0$ transitions, respectively. The fluorescence property of the $S_1(3s)$ state of TMA was investigated on the basis of measurements of the radiative lifetime (τ_{rad}) and fluorescence quantum yield (Φ_{flu}) as a function of the excitation wavelength from the onset (~ 260 nm) of the S_1-S_0 band toward the peak of the S_2-S_0 band;^{23,24,35,37} the fluorescence with $\tau_{\text{rad}} \approx 40$ ns and $\Phi_{\text{flu}} \approx 1$ in the

longer wavelength region (greater than 248 nm) decreases with the overlaying S_2 absorption and vanished at ~ 215 nm. The non-radiative decay of the shorter wavelength region was speculated to be due to internal conversion of the S_2 state. Ultrafast internal conversion of the S_2 state was directly measured by Cardoza *et al.* with time-resolved photoelectron spectroscopy at excitation wavelengths of 200 nm and 208 nm.³² The time constants of the $3p$ state decay and the $3s$ state rise were identical, indicating an exclusive electronic dynamics of the $3p \rightarrow 3s$ internal conversion in the S_2 state.

The dissociation of TMA following the S_2 - S_0 photoexcitation at 193 nm was investigated using photofragment translational spectroscopy.³⁸⁻⁴⁰ N - C bond fission, $\text{N}(\text{CH}_3)_3 + h\nu \rightarrow \text{CH}_3 + \text{N}(\text{CH}_3)_2$, was the primary reaction, whose translational energy distribution showed two distinct peaks. The high and low kinetic energy components were ascribed to production of internally unexcited and highly-excited $\text{N}(\text{CH}_3)_2$, respectively. Although generation of the electronic excited $\text{N}(\text{CH}_3)_2(\tilde{\text{A}}^2\text{A}_1)$ product was indicated to be possible as with the photochemistry of NH_3 and CH_3NH_2 ,^{16,22} subsequent studies with ionization spectroscopy and theoretical calculations did not confirm $\text{N}(\text{CH}_3)_2(\tilde{\text{A}}^2\text{A}_1)$ production as a source of the slow $\text{N}(\text{CH}_3)_2$ product.³⁹⁻⁴¹ On the other hand, the high kinetic energy component was unambiguously assigned to the $\text{CH}_3 + \text{N}(\text{CH}_3)_2(\tilde{\text{X}}^2\text{B}_1)$ pathway. The N-C bond fission at 193 nm was explained to occur on the S_1 PES after $S_2 \rightarrow S_1$ internal conversion, which facilitates the non-adiabatic transition in the vicinity of the exit conical intersection through the vibrational excitation of the ammonia-frame umbrella mode.³⁹

Theoretical studies examining the dissociative excited states of TMA have been conducted using quantum chemistry calculations.⁴¹⁻⁴³ The systematic calculations for CH₃NH₂, (CH₃)₂NH₂, and TMA by Taylor *et al.* indicated that the dissociative 3s state originated from carbon atoms in TMA was located closely to the bound 3s state associated with the nitrogen center.⁴³ Presence of the 3s Rydberg state centered on carbon atoms was also theoretically shown by Forde *et al.*; however, the assignments of the states to the absorption spectrum was not concurred.³⁹ Meanwhile, theoretical calculations for a series of large TAAs by Thompson *et al.* illustrated that the S₂(3p) state is predissociative as a mixed Rydberg/valence state whereas the S₁(3s) state remains strongly bound along all coordinates.³¹ A theoretical S₂(3p) PES obtained for a typical TAA (*N,N*-dimethylisopropylamine, R¹ = R² = CH₃, R³ = *iso*-CH(CH₃)₂) was qualitatively similar to the predissociative S₁(3s) PES of NH₃. A detailed topology of TMA excited state PESs, for discussing the dissociation dynamics, is not known; however, the energy levels of three lowest excited states were determined by ultrafast Rydberg photoelectron spectroscopy.^{32,44} These three states, responsible for UV absorption, are labeled with increasing energy as the 3s, 3p_{xy}, and 3p_z states. The sub-structures of the 3p_{xy}, and 3p_z states, which are not resolved in the absorption spectra and traditionally assigned to the S₂-S₀ band, have a small energy splitting of ~50 meV. These ultrafast electronic dynamics around the Franck-Condon geometry provides the basis for elucidating the photodissociation mechanism.

In the present study, a photodissociation dynamics study of TMA with an ion-imaging method is presented. We examined the excitation-wavelength dependence in the $\text{N}(\text{CH}_3)_3 + h\nu \rightarrow \text{CH}_3 + \text{N}(\text{CH}_3)_2$ photodissociation with state-selective detection of the nascent photofragments at various photolysis wavelengths over the S_2-S_0 and S_1-S_0 absorption bands. Since TMA is a tri-substituted NH_3 -derivative molecule and also the simplest TAA molecule, we discuss the photodissociation dynamics of TMA in terms of extensions from NH_3 photochemistry and from known TAA photochemistry.

4.2 Experimental and Analysis Methods

The ion-imaging apparatus was described previously in Chapter 2, and significant features of the present study are given here. The molecular beam was generated by supersonic expansion of a gas mixture containing 1 % of TMA (Sigma Aldrich) in He buffer gas at a stagnation pressure of 2 bar. During valve operation, the pressure of the source chamber and the detection chamber was kept at 2×10^{-6} Torr and 5×10^{-7} Torr, respectively. Both pump and probe laser beams, which were aligned in a counter-propagating direction, were moderately focused by quartz lenses ($f = 350$ mm) onto the molecular beam. The wavelength of the pump laser was varied over for 200–236 nm, which covers the range between the peaks of the S_2-S_0 and S_1-S_0 transitions of TMA. We employed UV light sources based on sum-frequency mixing (SFM) for 200–220 nm and second harmonic generation (SHG) for 220–236 nm. A tunable dye laser (CobraStretch, Spectra Physics) pumped by a Nd: YAG laser (LAB-170, Spectra Physics) was used for SFM and SHG. The pulse energy of the photolysis laser was reduced to less than 10 μ J/pulse. The probe pulse to ionize photofragments was delayed by 30 ns from the pump pulse. Another laser set consisting of a frequency-doubled tunable dye laser (CobraStretch, Spectra Physics) pumped by a Nd: YAG laser (Powerlite 9010, Continuum) was used for probing. The nascent CH_3 photofragment, which generated by the N–C bond fission ($\text{N}(\text{CH}_3)_3 + h\nu \rightarrow \text{CH}_3 + \text{N}(\text{CH}_3)_2$), was state-selectively ionized by the 2 + 1 REMPI scheme via the $3p^2 A_2'' - \tilde{X}^2 A_2''$ transition (322–336)^{45,46} following the irradiation of probe pulse. The pulse

energy of the probe laser (400–600 $\mu\text{J}/\text{pulse}$) was relatively higher than that of the pump laser; however, the signal-to-noise ratio was not degraded due to the lower photon energy. The contributions of the ions originating solely from the pump or probe laser to the pump-probe signal were negligibly low ($< 0.1\%$) for the most populated CH_3 state ($v = 0$) at the strongest absorption wavelength (200 nm). Wavelength calibration of the REMPI spectrum was performed on the basis of an optogalvanic method in the visible region using a Ne hollow cathode lamp. Relative pulse energies of the photolysis and probe lasers were recorded during data acquisition for monitoring the variation.

We measured the state-resolved scattering images of the CH_3 fragment at photolysis wavelengths in 2 nm intervals from 200 nm to 224 nm. Each image data was accumulated for 150,000 laser shots. The observed image data were numerically transformed to a sliced distribution by the Abel inversion, from which the recoil velocity and the scattering angular distributions were extracted. In the longer photolysis wavelengths, a background noise, which appeared in a central part of the images, relatively increased. Cluster formation was excluded for the background noise source by examining the dependence on the stagnation pressure and the photolysis laser pulse energy. We measured the images of the background noise at an off-resonant wavelength (331 nm) of the probe laser. Since the background noise appeared in a different image area from that of the CH_3 fragments whose scattering distributions are discussed in the present study, we used image data subtraction with the background noise image in analyzing the data with a low signal-to-noise ratio.

We measured the CH_3^+ ion intensity as a function of the photolysis wavelength to obtain the relative dissociation yield, Φ_{diss} . The wavelength of the probe laser was fixed at either the 0_0^0 or 2_1^1 vibrational band peaks in the REMPI spectrum, where ν_2 denotes the out-of-plane mode of the CH_3 radical. A decrease of Φ_{diss} from 200 nm to 224 nm was roughly 1/20, which is more rapid than the decrease of the absorbance: $\sigma_{\text{abs}}(200 \text{ nm}):\sigma_{\text{abs}}(224 \text{ nm}) \approx 1:4$. We measured Φ_{diss} by continuously scanning the photodissociation wavelength in the longer than 224 nm region, where Φ_{diss} decreased further. We extended our measurement of Φ_{diss} to the longest wavelength of 236 nm, where the peak of the CH_3 REMPI spectrum was completely lost in the background noise. We carefully inspected Φ_{diss} in the 224–236 nm region because the S_2-S_0 and S_1-S_0 absorption bands overlap and alternate the fractions to the total absorbance in this region.

4.3 Results

4.3.1 REMPI Spectra of the CH₃ Photofragments

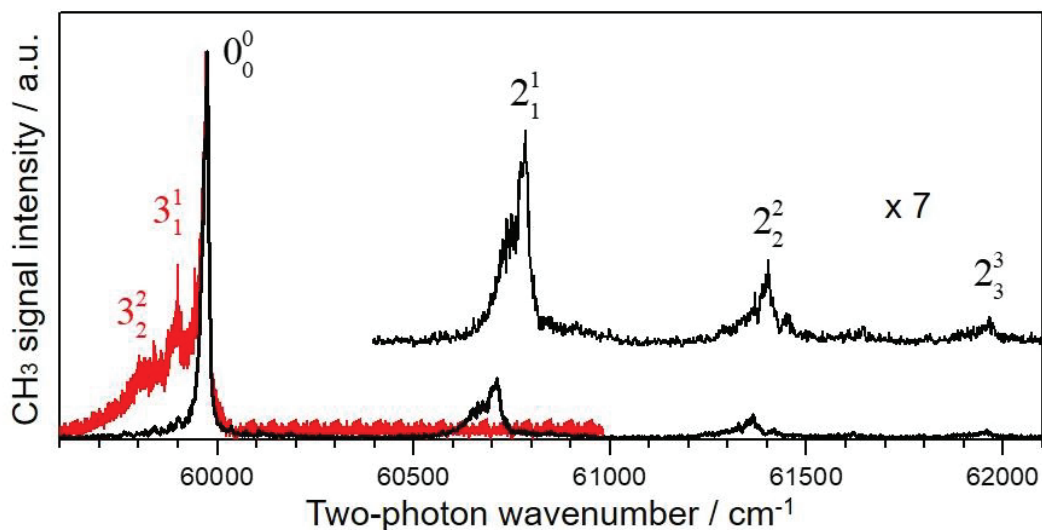


Figure 4.1 2 + 1 REMPI spectra of the CH₃ photofragment resulting from the photodissociation of trimethylamine, $\text{N}(\text{CH}_3)_3 + h\nu(200 \text{ nm}) \rightarrow \text{CH}_3 + \text{N}(\text{CH}_3)_2$, at photolysis wavelength of 200 nm (black). The weak bands are magnified for clarity. The CH₃ REMPI spectra in the photodissociation of methylamine ($\text{CH}_3\text{NH}_2 + h\nu(205 \text{ nm}) \rightarrow \text{CH}_3 + \text{NH}_2$) is shown in red for comparison.

The REMPI spectrum of the CH₃ fragment in the photodissociation of TMA at 200 nm, which is the peak wavelength of the S_2 – S_0 absorption band, is shown in Figure 4.1. The vibrational structure in the higher frequency region than the 0_0^0 band ($\sim 59,970 \text{ cm}^{-1}$) was assigned to the $2_{v'}^1$ band sequence, indicating the preferential excitation of the v_2 (out-of-plane bending) mode of the CH₃ product. The spectrum of the CH₃ fragment measured in the photodissociation of methylamine (CH_3NH_2) at 205 nm is shown in red for comparison. The intensity of the 0_0^0 band of the TMA (black) and CH_3NH_2 (red) photodissociations were normalized in Figure 4.1. A marked difference was visible for the vibrational-state

distribution in the N—C bond fission for the primary- amine and tertiary-amine. A favorable generation of the CH₃ product in the ν_3 (asymmetric C—H stretch mode, $\nu_3 = 3161 \text{ cm}^{-1}$) excited states was observed in CH₃NH₂ photodissociation,^{14,22} whereas the CH₃ fragments in the TMA dissociation were populated specifically in the ν_2 excited states of $\nu_2 = 1-3$ ($\nu_2 = 606 \text{ cm}^{-1}$). Since the available energy of the photodissociation of TMA at 200 nm is higher by $\sim 5000 \text{ cm}^{-1}$ than that of CH₃NH₂ at 205 nm for the observed pathways, the ν_2 excitation of the CH₃ product is not an energetic but a dynamical outcome of the TMA photodissociation. We extended the REMPI spectral measurements with the photolysis wavelengths from 200 nm to 224 nm by 2 nm increments, where the S_2-S_0 and S_1-S_0 transitions of TMA obviously overlapped. A wide spectral scan covering from the 0_0^0 band to the 2_3^3 band was conducted at the photolysis wavelengths of 200 nm, 206 nm and 212 nm. At other photolysis wavelengths, the spectral region containing the 0_0^0 band and the 2_1^1 band was measured. The relative band intensity of the REMPI spectra was quite similar in the photolysis wavelength range of 200–224 nm, which is shown in Figure 4.2. The ν_2 vibrational-state distributions of the CH₃ product (Figure 4.3) were determined by contour analysis of the vibrational bands using the Franck-Condon factors.⁴⁷ The ν_2 excitations were insensitive to the photolysis wavelength; the gray plots (showing the data at different photolysis wavelengths in Figure 4.3) did not deviate from the averaged values (shown in red).

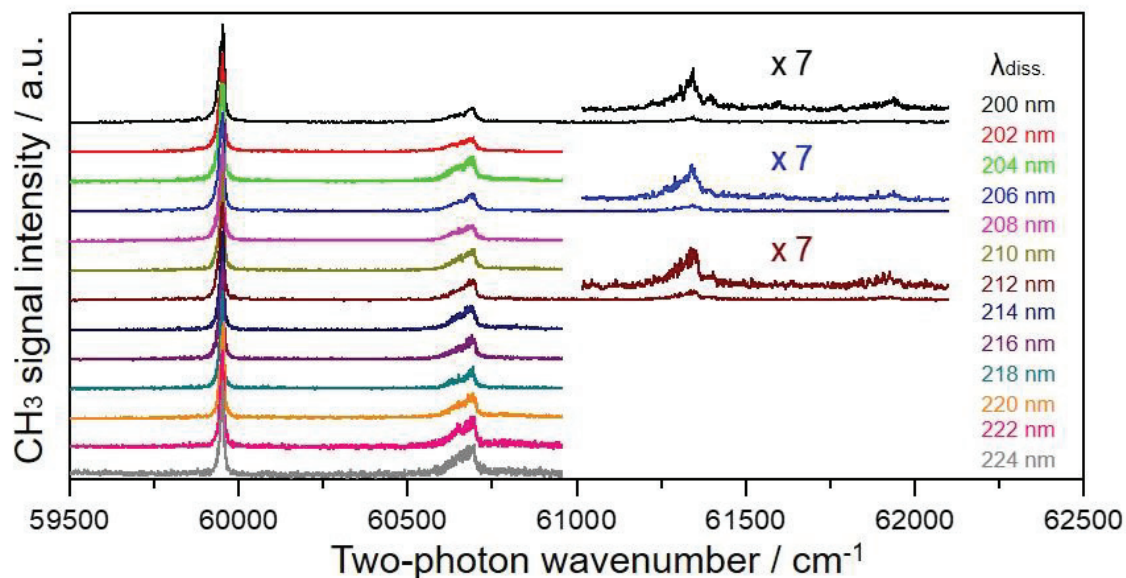


Figure 4.2 REMPI spectra of the CH_3 photofragment at various photolysis wavelength ($\lambda_{\text{diss.}}$) in the 200–224 nm region. The band assignment is shown in Figure 4.1.

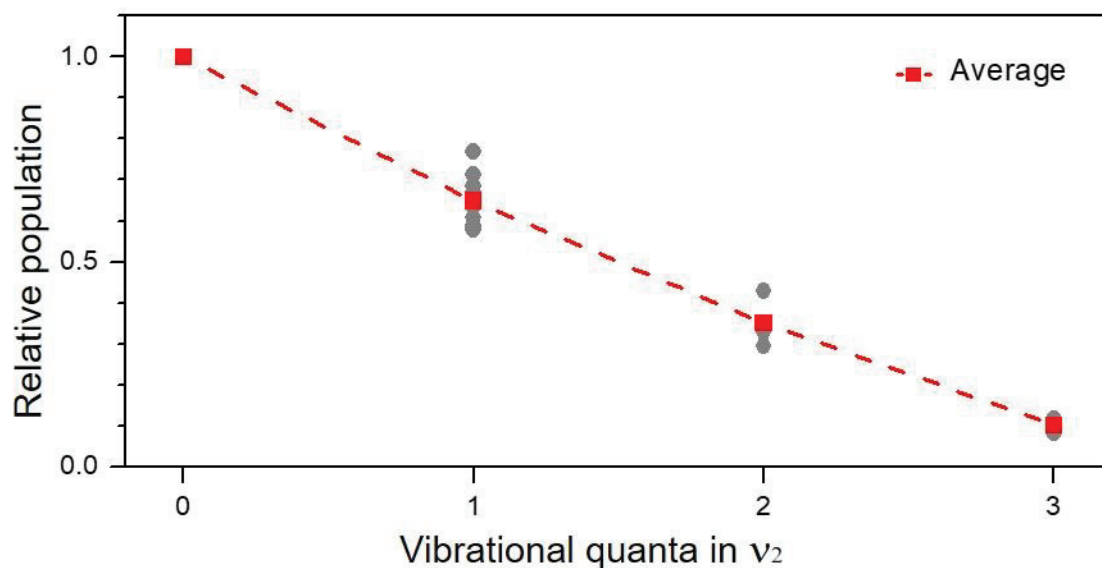


Figure 4.3 Vibrational-state distributions of the CH_3 photofragments for the ν_2 mode (out-of-plane bending). The relative population are normalized to unity at $\nu_2 = 0$. Gray points indicate the relative populations at various photolysis wavelength in the 200–224 nm region. The averaged value for the different photolysis wavelengths in each ν_2 state is plotted in red.

4.3.2 Dissociation Yields

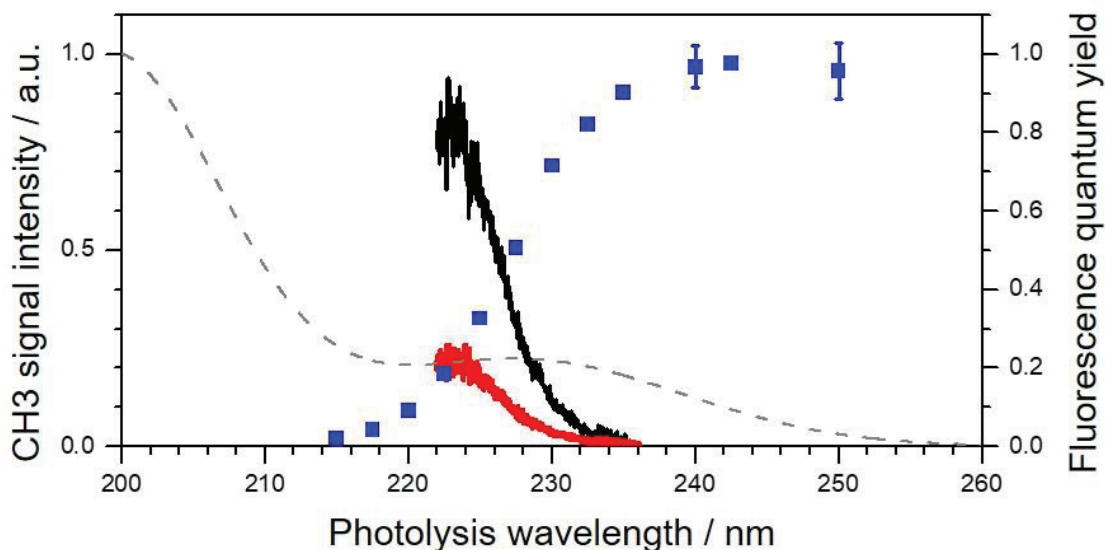


Figure 4.4 Dissociation yield spectra as a function of the photolysis wavelength (220–236 nm). The black and red lines denote the variation in the signal intensity of the nascent $\text{CH}_3(v = 0$ and $v_2 = 1)$, respectively. The fluorescence quantum yield (blue squares) taken from Ref. 35 and the absorption spectrum of TMA (gray broken line) are superimposed for comparison.

Figure 4.4 shows the relative Φ_{diss} (dissociation quantum yield) spectra for the $\text{CH}_3(v = 0)$ (in black) and $\text{CH}_3(v_2 = 1)$ (in red) products in the photolysis wavelength region of 222–236 nm. The Φ_{flu} (fluorescence quantum yield) values measured by Matsumi and Obi (in blue),³⁵ and the absorption spectrum at 298 K³⁶ (gray broken line) are displayed for comparison. The Φ_{diss} curves began to rise at 235 nm, indicating a dissociation threshold. The rising edge of Φ_{diss} was located energetically lower than the band origin of the S_2 – S_0 transition (226 nm, $44,290 \text{ cm}^{-1}$) determined by Cardoza and coworkers with ultrafast photoelectron spectroscopy,^{32,44} indicating dissociation occurs in the S_1 state. Differences in the rising edge wavelengths for $\Phi_{\text{diss}}(v = 0)$ and $\Phi_{\text{diss}}(v_2 = 1)$ were not discernible in the

present measurement. The ratio of $\Phi_{\text{diss}}(v = 0) : \Phi_{\text{diss}}(v_2 = 1) \approx 1:4$ was invariant over 222–236 nm. This wavelength dependence was consistent with that of the REMPI spectra in the 200–224 nm range, which exhibited a constant vibrational-state distribution for the CH₃ products. An alternation of the Φ_{diss} and Φ_{flu} intensities with respect to the wavelength was noted. The nearly unity value of Φ_{flu} from the S_1 origin at 266 nm ($37,550 \text{ cm}^{-1}$)²⁴ to 240 nm begins to fall at the rising edge of Φ_{diss} (235 nm), decreasing down to 0.3 at the S_2 origin. The three plots in Figure 4.4 imply a switching from a fluorescent nature to a dissociative nature for the photoexcited states in the S_2 – S_0 and S_1 – S_0 overlapping region. However, the S_2 and S_1 states were not individually characterized as dissociative and fluorescent states, respectively, because the CH₃ photofragments were detected below the S_2 origin.

4.3.3 State-Resolved Ion-Images of the CH₃ Photofragments

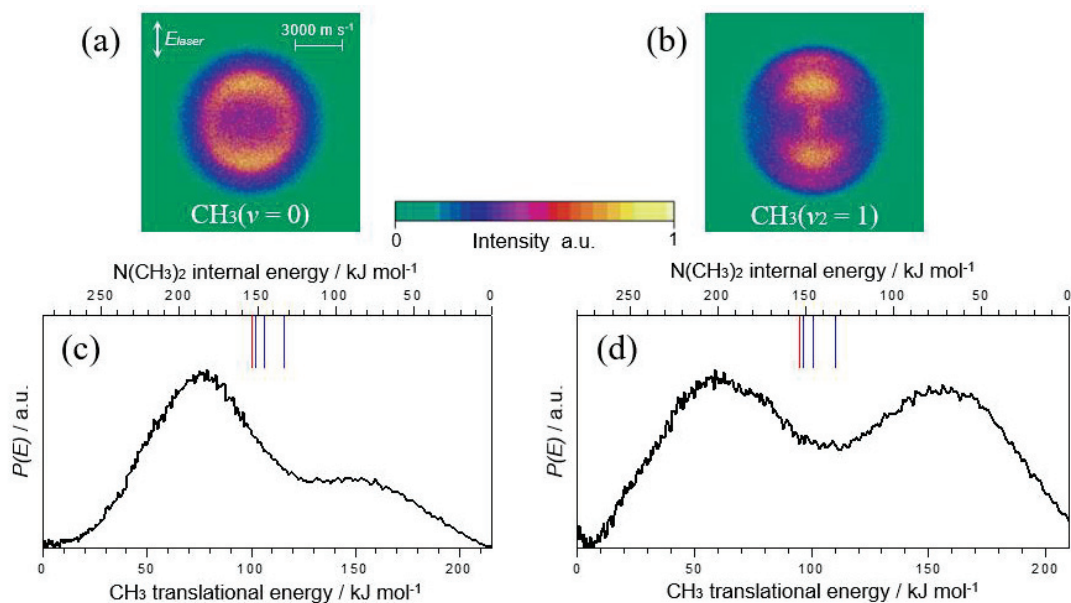


Figure 4.5 Vibrationally state-resolved scattering images of the CH₃ fragment generated in the (a) $\nu = 0$ and (b) $\nu_2 = 1$ states at the photolysis wavelength of 200 nm. These images were measured at the peak of each vibrational band in the REMPI spectrum. The CH₃ translational energy distributions of the (c) $\nu = 0$ and (d) $\nu_2 = 1$ states obtained by the image data analysis. The upper scale corresponds to the total internal energy of the N(CH₃)₂ counter-product. A red bar represents the theoretically predicted energy limit for formation of N(CH₃)₂(\tilde{A}^2A_1). Blue bars indicate the theoretical and experimental \tilde{A} state energy of the smaller amino radicals (NH₂(\tilde{A}^2A_1) and CH₃NH(\tilde{A}^2A')).

Examples of the state-resolved CH₃ scattering images are shown in Figure 4.5: the vibrational ground state (Figure 4.5(a)) and the $\nu_2 = 1$ state (Figure 4.5(b)) at the photolysis wavelength of 200 nm. The scattering images of the CH₃ fragments in both $\nu = 0$ and $\nu_2 = 1$ states exhibited dual ring-like features, indicating the generation of both slow and fast CH₃ products. These two velocity components were more visible in the translational energy distributions, $P(E_{trans}^{CH_3})$, extracted from these images, which are shown in Figures 4.5(c)

and 4.5(d). The $P(E_{trans}^{CH_3})$ of the $v = 0$ and $v_2 = 1$ states were similarly bimodal; however, the $E_{trans}^{CH_3}$ range and intensity ratio between the slow and fast components were state-dependent. The bimodal structure of $P(E_{trans}^{CH_3})$ was similar to that observed in the previous study with translational spectroscopy at the photolysis wavelength of 193 nm.^{39,40} We fitted the $P(E_{trans}^{CH_3})$ data to two Gaussian functions to determine the average values of the translational energy, $\langle E_{trans}^{CH_3} \rangle$, and the ratio between these components for quantitative analysis. The $\langle E_{trans}^{CH_3} \rangle$ for each velocity component of the $v = 0$ and $v_2 = 1$ states are listed in Table 4.1. The angular distributions of the observed images were apparently anisotropic. The anisotropy parameters (β) were also determined independently for each velocity component of the $v = 0$ and $v_2 = 1$ states. All the determined β values were positive (0.2–0.5). The β values of the $CH_3(v_2 = 1)$ fragment was noticeably larger than that of the $CH_3(v = 0)$ fragment, whereas the difference between the slow and fast components were considerably smaller (Table 4.1).

Table 4.1 Averaged translational energy and anisotropy parameters of the CH_3 photoproduct and averaged total internal energy of the $N(CH_3)_2$ counter-product for the photolysis wavelength of 200 nm.

State	Component	$\langle E_{trans}^{CH_3} \rangle / \text{kJ mol}^{-1}$	$\langle E_{int}^{N(CH_3)_2} \rangle / \text{kJ mol}^{-1}$	β
$v = 0$	slow	75.0	186.7	0.25
	fast	154.2	52.6	0.21
$v_2 = 1$	slow	61.4	197.6	0.48
	fast	154.2	73.2	0.48

The total internal energy of the nascent $\text{N}(\text{CH}_3)_2$ counter-product, $E_{trans}^{N(\text{CH}_3)_2}$, is related to $E_{trans}^{CH_3}$ in the state-resolved scattering results by the energy conservation restriction: $h\nu = D(\text{C}-\text{N}) + E_{trans}^{CH_3} + E_{trans}^{N(\text{CH}_3)_2} + E_{int}^{CH_3} + E_{int}^{N(\text{CH}_3)_2}$, where $D(\text{C}-\text{N}) = 310.8$ kJ/mol (bond dissociation energy of $\text{N}(\text{CH}_3)_3 \rightarrow \text{CH}_3 + \text{N}(\text{CH}_3)_2$)⁴⁸ was used in the evaluation. The upper scale in Figs. 4.5(c) and 4.5(d) indicates the calculated $E_{int}^{N(\text{CH}_3)_2}$ for each selected CH_3 vibrational state. Thus, the fast and slow components in $P(E_{trans}^{CH_3})$ correspond to the lower and higher $E_{int}^{N(\text{CH}_3)_2}$ components, respectively. The averaged value of $E_{int}^{N(\text{CH}_3)_2}$ ($\langle E_{int}^{N(\text{CH}_3)_2} \rangle$) for each component is also summarized in Table 4.1. The $\text{N}(\text{CH}_3)_2$ radical has a low-lying electronic state ($\tilde{\text{A}}^2\text{A}_1$), whose term energy was theoretically evaluated to be 153 kJ/mol,⁴¹ as indicated by the red bar on the upper scale in Figure 4.5(c) and 4.5(d). The energy of the $\tilde{\text{A}}^2\text{A}_1$ state of $\text{N}(\text{CH}_3)_2$ is not experimentally determined. Theoretical $\tilde{\text{A}}-\tilde{\text{X}}$ intervals of CH_3NH (152 kJ/mol and 145 kJ/mol)^{10,19} and the spectroscopic value for NH_2 (133 kJ/mol) are shown in blue as references. Generation of the excited $\text{N}(\text{CH}_3)_2(\tilde{\text{A}}^2\text{A}_1)$ product was discussed analogously with the photodissociations of NH_3 and CH_3NH_2 in the previous studies.^{39,40} Although the lower energy limit of the higher $E_{int}^{N(\text{CH}_3)_2}$ component was not determined because of the overlap of the two $E_{int}^{N(\text{CH}_3)_2}$ components, it is reasonable to consider that the onset of the higher $E_{int}^{N(\text{CH}_3)_2}$ component is located near the theoretically predicted threshold of the $\text{N}(\text{CH}_3)_2(\tilde{\text{A}}^2\text{A}_1)$ production. We ascribed the higher and lower $E_{int}^{N(\text{CH}_3)_2}$ peaks to the $\text{CH}_3 + \text{N}(\text{CH}_3)_2(\tilde{\text{A}}^2\text{A}_1)$ and $\text{CH}_3 + \text{N}(\text{CH}_3)_2(\tilde{\text{X}}^2\text{B}_1)$ product pathways, respectively.

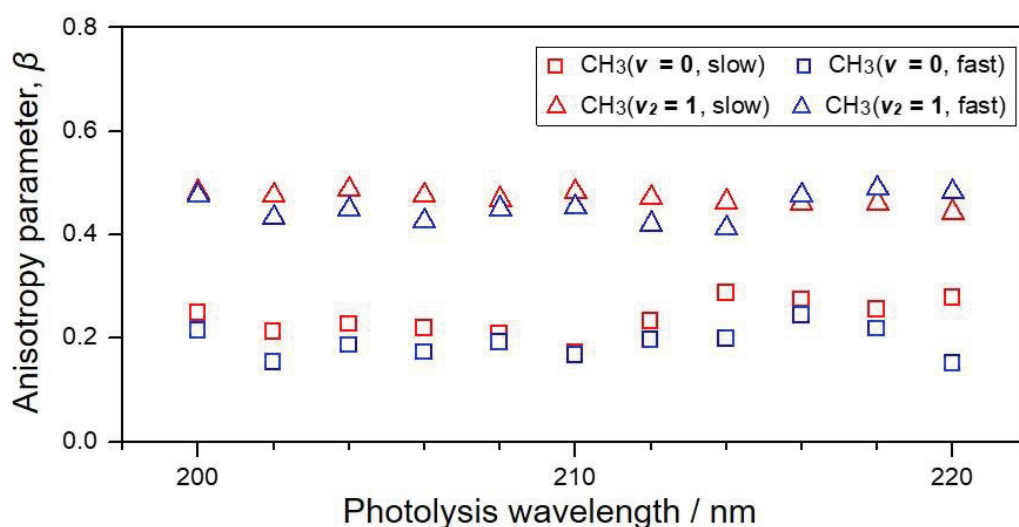


Figure 4.6 Anisotropy parameters (β) of the CH_3 photofragments as a function of the photolysis wavelengths varied from 200 nm to 220 nm. The β parameters obtained from the state-resolved scattering images of the CH_3 fragments generated in the vibrational ground ($\nu = 0$) and excited ($\nu_2 = 1$) states are shown by square and triangle points, respectively. The β parameters of the low and high kinetic energy components are shown in red and blue, respectively.

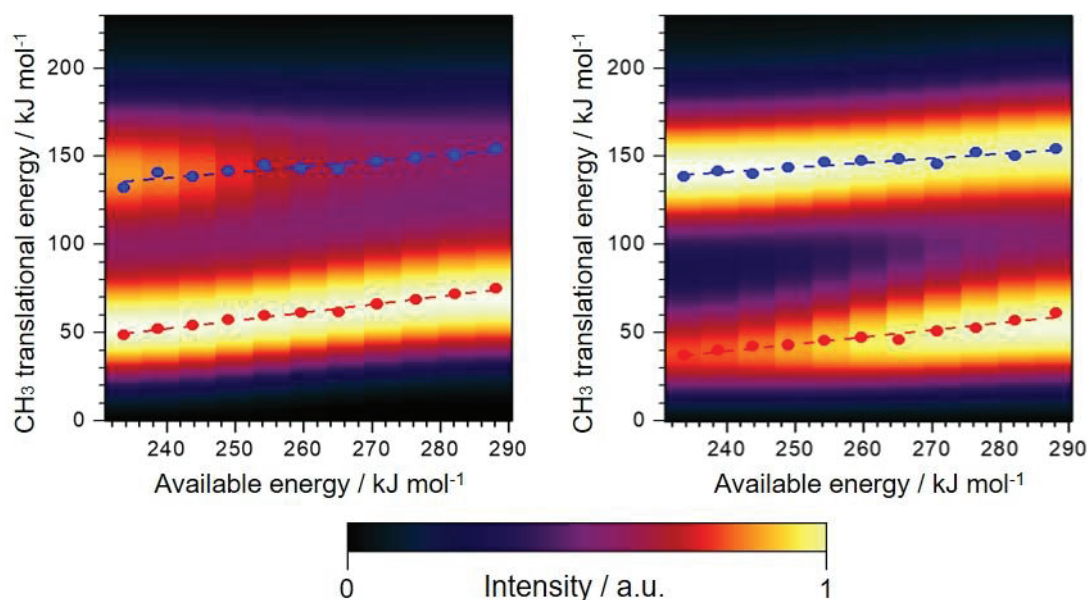


Figure 4.7 Counter plots of the CH_3 translational energy distributions of (a) $\nu = 0$ and (b) $\nu_2 = 1$ states with respect to the available energy. The peak energy positions of the low and high kinetic energy components are plotted as red and blue points, respectively.

We performed ion-imaging measurements of CH₃ ($v = 0$ and $v_2 = 1$) in the photolysis wavelength range of 200–220 nm at 2 nm intervals. The β values of the higher and lower $E_{trans}^{CH_3}$ components determined independently for the CH₃($v = 0$) and CH₃($v_2 = 1$) products were insensitive of the photolysis wavelength. The state-resolved and $E_{trans}^{CH_3}$ -resolved β values as a function of the photolysis wavelength are shown in Figure 4.6. However, since the available energy ($E_{avl} = h\nu - D(C-N)$) varies with the photon energy, $\langle E_{trans}^{CH_3} \rangle$ does. Figure 4.7 shows a contour plot of the $P(E_{trans}^{CH_3})$ obtained for 11 photolysis wavelengths as a function of E_{avl} : the $P(E_{trans}^{CH_3}) - E_{avl}$ plots for $v = 0$ (Figure 4.7(a)) and $v_2 = 1$ (Figure 4.7(b)). The $\langle E_{trans}^{CH_3} \rangle$ values obtained by assuming Gaussian functions are plotted in red (for slow CH₃) and blue (for fast CH₃). The $E_{trans}^{CH_3}$ of both slow and fast CH₃ ($v = 0$ and $v_2 = 1$) products increased linearly with increasing E_{avl} . The slopes ($\Delta E_{trans}^{CH_3} / \Delta E_{avl} \sim 0.4$) of these plots were constant over the inspected energy region.

The intensity ratio of the slow and fast CH₃ components in $P(E_{trans}^{CH_3})$ provided the branching ratio between the CH₃ + N(CH₃)₂($\tilde{A}^2 A_1$) and CH₃ + N(CH₃)₂($\tilde{X}^2 B_1$) product pathways. In addition, the present state-resolved measurements at varying photon energies quantified the preference between the vibrational states of the CH₃ product and the electronic states of the N(CH₃)₂ counter-products as a function of E_{avl} . The vibrational state-dependent branching ratio, $\Phi^v(\tilde{A}/\tilde{X})$, is defined as

$$\Phi^v(\tilde{A}/\tilde{X}) = \frac{S^v(\text{slow})}{S^v(\text{slow}) + S^v(\text{fast})},$$

where S^v is the area of the Gaussian function fitted to the designated components (fast or slow) in $P(E_{trans}^{CH_3})$ for the vibrational state v . The $\Phi^v(\tilde{A}/\tilde{X})$ data were plotted as a function of E_{avl} in Figure 4.8, indicating the larger production of $N(CH_3)_2(\tilde{A}^2A_1)$ as E_{avl} increased for both $v=0$ and $v_2=1$ states. The production of the $N(CH_3)_2$ in the \tilde{A}^2A_1 state was relatively favorable when the CH_3 co-product was generated in the $v=0$ state ($\Phi^{v=0}(\tilde{A}/\tilde{X}) > 0.5$). The $\Phi^{v=0}(\tilde{A}/\tilde{X})$ value was larger than $\Phi^{v_2=1}(\tilde{A}/\tilde{X})$ by $\sim 20\%$ over the E_{avl} range of 230–290 kJ/mol, implying a moderate preferential tendency for producing the vibrationally excited CH_3 products and the electronic de-excited $N(CH_3)_2$ counter-product.

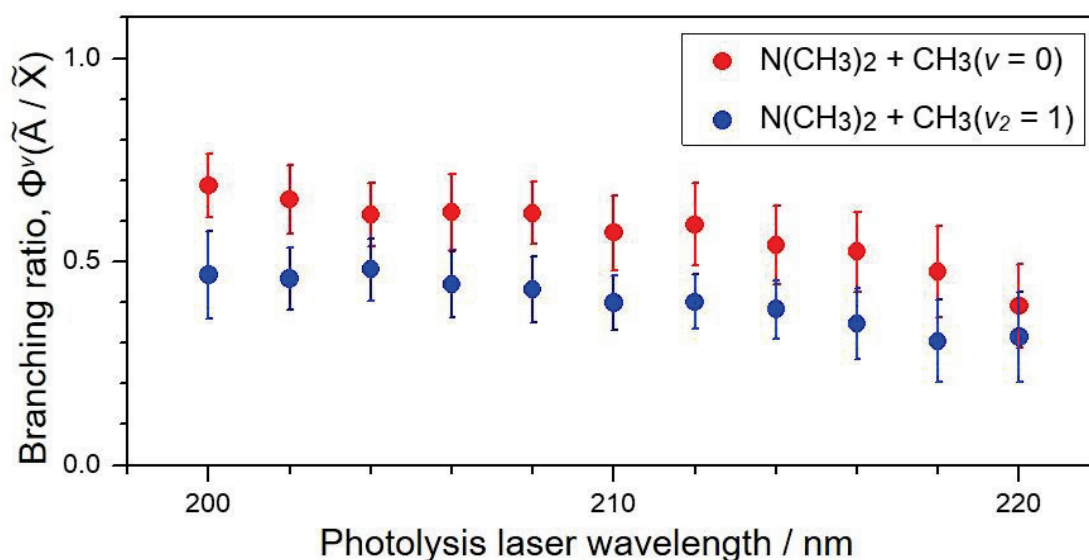


Figure 4.8 Available energy dependence of the branching ratio between the product pathways of $CH_3 + N(CH_3)_2(\tilde{A}^2A_1)$ and $CH_3 + N(CH_3)_2(\tilde{X}^2B_1)$. Red and blue points denote the branching ratio associated with the CH_3 final states of $v=0$ and $v_2=1$, respectively.

4.4 Discussion

4.4.1 Electronic Dynamics and Dissociation Dynamics

The REMPI spectra of the CH₃ fragments, which reflect the final-state distributions, were almost entirely invariant in the photolysis wavelength region of 200–224 nm, where the photoinitiated state changes from the S_2 state to the S_1 state. The CH₃ scattering distributions showed no significant difference in this energy region, where E_{avl} varied by 60 kJ/mol ($\sim 5000\text{ cm}^{-1}$) from 230 kJ/mol to 290 kJ/mol. These results indicate a single dissociation mechanism irrespective of the photoinitiated states, indicating fast electronic relaxation prior the N – C bond dissociation. Ultrafast and highly efficient internal conversion of TMA was suggested by Cardoza *et al.* with photoelectron spectroscopy;³² the S_2 state decayed to the S_1 state with a 2.9 ps time constant, and no signature of the S_1 state depletion was found until 10 ps (time window of the measurements). Our measurement results of the CH₃ product revealed that the photodissociation began after being populated in the S_1 states either by S_1 – S_0 photoabsorption or by the $S_2 \rightarrow S_1$ internal conversion, supporting the preceding electronic dynamics in the Franck-Condon region.

The N – C bond dissociation finally occurs on the σ_{N-C}^* PES. The coupling of the σ_{N-C}^* state to the $S_1(3s)$ state has not been theoretically proved for TMA. The quantum chemistry calculations of CH₃NH₂, which exhibited N – C bond photodissociation as well as TMA, illustrated the mixing of the σ_{N-C}^* orbital and the 3s Rydberg orbital to form the $S_1(3s/\sigma_{N-C}^*)$ PES with a barrier structure at the N – C bond length of $\sim 2\text{ \AA}$.^{18,19} This is

essentially identical to the $S_1(3s/\sigma_{\text{N-H}}^*)$ PES of NH_3 , whose barrier causes predissociation. If the $S_1(3s)$ PES of TMA has the predissociative structure of the NH_3 -derivative, the dissociation threshold determined in the Φ_{diss} measurement can be regarded as the barrier height of the $S_1(3s/\sigma_{\text{N-C}}^*)$ PES, which corresponds to the energy difference of 5000 cm^{-1} between the rise wavelength of the CH_3 product (235 nm, $42,500\text{ cm}^{-1}$) and the S_1 origin (266 nm). The value is similar to the theoretical barrier height of the $S_1(3s/\sigma_{\text{N-C}}^*)$ PES of CH_3NH_2 (4900 cm^{-1} and 8000 cm^{-1} without zero-point energy correction),^{18,19} supporting the N–C dissociation on the S_1 PES over the barrier.

TMA is a member of TAA, and analogous electronic structures are expected. Thompson *et al.* calculated the excited state PESs of *N,N*-dimethylisopropylamine, which is formed by substituting a CH_3 group of TMA with an isopropyl group ($-\text{CH}(\text{CH}_3)_2$), with high-level *ab initio* methods, revealing the mixing of the $3p$ orbital and the $\sigma_{\text{N-C}}^*$ orbital to form the $S_2(3p/\sigma_{\text{N-C}}^*)$ PES with a barrier structure.³¹ The theoretical calculations indicated that the $S_1(3s)$ PES was a bound state. At an elongated N–C bond length of $\sim 1.9\text{ \AA}$, the bound $S_1(3s)$ PES and the dissociative part of the $S_2(3p/\sigma_{\text{N-C}}^*)$ were predicted to have a crossing. Re-entering to the $S_2(3p/\sigma_{\text{N-C}}^*)$ after the $S_2 \rightarrow S_1$ internal conversion through the crossing was proposed for the dissociation mechanism of TAA.³¹ The predissociative $S_2(3p/\sigma_{\text{N-C}}^*)$ in contrast with the $S_1(3s/\sigma_{\text{N-C}}^*)$ PESs of smaller NH_3 -derivatives has not yet been established as a common electronic character to TAA; however, TMA is likely to have similar $S_2(3p/\sigma_{\text{N-C}}^*)$ and $S_1(3s)$ PESs on the basis of the analogous chemical bonds.

Assuming the bound $S_1(3s)$ PES and the $S_2(3p/\sigma_{N-C}^*)$ PES for TMA, the crossing region can be barrier-shaped along the dissociation coordinate, which effectively acts as the reaction barrier. We consider that the dissociation threshold determined in our experiments provides the energy of the $S_2(3p/\sigma_{N-C}^*)/S_1(3s)$ crossing as another possible interpretation, rather than the barrier height of the $S_1(3s/\sigma_{N-C}^*)$ PES, as discussed in the previous paragraph. Although the coupling preference of the σ_{N-C}^* orbital with either of the $3s$ or $3p$ Rydberg orbitals in simple amines, including TMA, was discussed by Taylor *et al.* in their theoretical study,⁴³ the details of the PES structure and the electronic characterization of the $S_2(3p)/S_1(3s)$ crossing were not clarified. Our experimental Φ_{diss} , which can be explained either by the S_2 or S_1 dissociation, provides an energy value at probable critical geometries: 5000 cm^{-1} for the barrier height in the $S_1(3s/\sigma_{N-C}^*)$ or $42\,500 \text{ cm}^{-1}$ for the energy of the crossing of $S_2(3p/\sigma_{N-C}^*)/S_1(3s)$.

We ascribe the dissociation threshold either to the barrier in the $S_1(3s/\sigma_{N-C}^*)$ PES or the crossing of $S_2(3p/\sigma_{N-C}^*)/S_1(3s)$ in the previous paragraph. The rising edge of Φ_{diss} corresponded well with the falling off wavelength of Φ_{flu} (Figure 4.4). If the S_2 PES was purely repulsive, the rising edge of Φ_{diss} would be interpreted as an onset of the S_2-S_0 band. Indeed, Cureton *et al.* analyzed the dual exponential fluorescence decay curve as a function of the wavelength in the S_2-S_0 and S_1-S_0 overlapping region to decompose the mixed absorption spectrum by plotting the ratio of fast (radiative) and slow (non-radiative) decay components.²³ The onset of the thus decomposed S_2-S_0 band (the S_2 origin) was coincident

with the appearance threshold in the present Φ_{diss} spectra ($42,500 \text{ cm}^{-1}$). Later, the S_2 origin was directly determined to be $44,290 \text{ cm}^{-1}$ (226 nm),^{32,44} so that the coincidence of the rise of the Φ_{diss} spectra in our measurement and the S_2 origin proposed in the previous study²³ should now be considered accidental. The dissociation threshold is located between the S_1 origin and the S_2 origin, and the Φ_{diss} monotonically increased toward the S_2 - S_0 absorption peak. These results reinforce the hypothesis that the $S_2 \rightarrow S_1$ internal conversion is highly efficient, whereas the direct dissociation in the S_2 PES is unlikely.

4.4.2 Anisotropy of the Scattering Distributions

The anisotropic angular distributions of the CH_3 fragment suggest that the photodissociation time constant is not much longer than the rotational period (τ_{rot}) of TMA. We performed ground state geometrical optimization using density functional theory (DFT/B3LYP) implemented in Gaussian09⁴⁹ with an aug-cc-pVQZ basis set to obtain the structural parameters of TMA, yielding $R(\text{C}-\text{H}) = 1.09 \text{ \AA}$, $R(\text{N}-\text{C}) = 1.45 \text{ \AA}$, $\alpha = 131^\circ$, and $\gamma = 122^\circ$, where α and γ denote the pyramidal angles for the ammonia-frame and methyl-frame, respectively. The pyramidal angle is defined as the angle between a bond and the bisector of other two bonds. The rotational constants calculated from the optimized structure ($A = B = 0.29 \text{ cm}^{-1}$ and $C = 0.16 \text{ cm}^{-1}$) yielded an approximate τ_{rot} value of 110 ps. This evaluation suggests that the CH_3 angular distribution can be anisotropic, unless the dissociation time scale is longer than order of 100 ps. Although the time evolution of TMA

in the S_1 state after 10 ps was not shown in the previous time-resolved photoelectron study,³² Thompson *et al.* experimentally demonstrated that three other TAA species in the S_1 state disappeared at ~ 100 ps.³¹ We consider that the dissociation time of 110 ps, which is comparable with τ_{rot} , can be a good estimate for TMA.

The positive β parameters determined for the photolysis wavelength region of 200–220 nm imply a small angle between the transition dipole moment (μ) and the dissociation bond direction. Our calculation yielded the angle between the N–C bond and the principal z -axis of TMA to be 73° . Assuming instantaneous dissociation following the $3p_{xy}$ photoexcitation, where the angle of the μ vector to the N–C bond is 17° , the upper limit of $\beta = 1.7$ was roughly obtained. The obtained β values were smaller than the hypothetical upper limit, supporting the reaction time scale of 110 ps, during which the angular distributions smeared. However, it is noted that the theoretical study by Cardoza *et al.* predicted that a large portion of absorbance at 200 nm was responsible for the $3p_z$ excited state,³² indicating negative β parameters (lower limit of $\beta = -0.7$) for the dissociation. The experimental β parameters (0.2–0.5) are more reasonably explained by comparable absorptions of the $3p_{xy}$ and $3p_z$ manifolds in the $S_2(3p)$ – S_0 absorption band.

4.4.3 Branching of the Product Pathways

In analogy with the NH_3 and CH_3NH_2 photodissociations, the $\sigma_{\text{N-C}}^*$ PES is presumably correlated to the pathway generating the electronic excited $\text{N}(\text{CH}_3)_2(\tilde{\text{A}}^2\text{A}_1)$ product, and the exit conical intersection causes the generation of the ground state $\text{N}(\text{CH}_3)_2(\tilde{\text{X}}^2\text{B}_1)$ product. Both $E_{\text{trans}}^{\text{CH}_3}$ and $\Phi^v(\tilde{\text{A}}/\tilde{\text{X}})$ values similarly increased with increasing E_{avl} (Figure 4.6 and Figure 4.8) irrespective to the final vibrational states of the CH_3 radical. These results suggest the non-adiabatic transition in the exit conical intersection region is less favorable with the higher $E_{\text{trans}}^{\text{CH}_3}$. Assuming that $E_{\text{trans}}^{\text{CH}_3}$ gives an effective velocity passing through the exit conical intersection based in a one-dimensional manner, the results imply that the non-adiabatic transition probability decreases with the higher velocity. This description is contradictory to a general property of non-adiabatic transitions, indicating that molecular ro-vibrational motions should be taken into account. Our measurements indicated that the fraction of E_{avl} to $E_{\text{trans}}^{\text{CH}_3}$ was $\sim 20\%$ with an increase of 40% from E_{avl} in the inspected energy region (Figure 4.6), where the internal energy distribution of the CH_3 products was unchanged (Figure 4.2). We speculate that the $\text{N}(\text{CH}_3)_2$ moiety is vibrationally excited when $\text{CH}_3-\text{N}(\text{CH}_3)_2$ visits the exit conical intersection, so that vibrational modes other than the $\text{N}-\text{C}$ bond coordinate influence the branching ratio between the $\text{CH}_3 + \text{N}(\text{CH}_3)_2(\tilde{\text{A}}^2\text{A}_1)$ and $\text{CH}_3 + \text{N}(\text{CH}_3)_2(\tilde{\text{X}}^2\text{B}_1)$ pathways.

The preferential combinations of the vibrationally excited CH_3 and the electronic ground $\text{N}(\text{CH}_3)_2$ product pair shown in Figure 4.8 may indicate a pyramidal structure for

the CH₃ group at the exit conical intersection. The degree of the ν_2 excitation in the REMPI spectra of the CH₃ fragments from TMA (black in Figure 4.1) and CH₃NH₂ (red in Figure 4.1) were remarkably contrasting. A planar CH₃ structure was theoretically predicted for the exit conical intersection of CH₃NH₂.¹⁹ Assuming that the trajectories to the product pathway with N(CH₃)₂ (\tilde{X}^2B_1) are restricted to visiting the exit conical intersection with a pyramidal CH₃ structure, the ν_2 out-of-plane mode of the CH₃ product, which is a planar molecule, is possibly excited after the passage. It is noted that the exit conical intersection of TMA was not theoretically illustrated, and our discussion is based on the established facts of the NH₃ photodissociation dynamics. Nevertheless, the experimental data must reflect dynamical outcomes of the TMA photodissociation, for which theoretical corroboration is still required.

4.5 Conclusion

The photodissociation dynamics of TMA following the S_2-S_0 and S_1-S_0 transitions were investigated by REMPI spectroscopy and state-resolved ion-imaging of the CH_3 product. The REMPI spectra exhibited the specific ν_2 (out-of-plane bending) excitation of the CH_3 photofragments up to $\nu_2 = 3$. The scattering images measured for the vibrational ground and ν_2 excited states displayed dual ring structures, which indicated two product pathways of $\text{CH}_3 + \text{N}(\text{CH}_3)_2(\tilde{\text{A}}^2\text{A}_1)$ and $\text{CH}_3 + \text{N}(\text{CH}_3)_2(\tilde{\text{X}}^2\text{B}_1)$. These dynamical features of the CH_3 fragments were qualitatively unchanged over the photolysis wavelengths in 200–236 nm, where the photoinitiated states interchange between the $S_2(3p)$ and $S_1(3s)$ states. The independence of the product state distributions on the photolysis wavelength was explained by distinct time scales of the $S_2 \rightarrow S_1$ internal conversion (3 ps) and the N–C bond dissociation (110 ps). The dissociation threshold was experimentally determined to be $42,500 \text{ cm}^{-1}$. Two possible interpretations for the measured threshold were discussed: the reaction barrier height of the $S_1(3s/\sigma_{\text{N-C}}^*)$ PES and the crossing of the predissociative $S_2(3p/\sigma_{\text{N-C}}^*)$ PES with the bound $S_1(3s)$ state. The present experimental results are inconclusive for uniquely specifying the interacting state of the dissociative $\sigma_{\text{N-C}}^*$ PES to either $3p$ or $3s$ state. Even if TMA has the $S_2(3p/\sigma_{\text{N-C}}^*)$ state, crossing to the bound $S_1(3s)$ state should have a barrier-type topology, whose height gives the dissociation threshold. In analogy with NH_3 , the $\sigma_{\text{N-C}}^*$ PES is likely to have a conical intersection with the ground state PES in the exit region, where the product pathway to $\text{CH}_3 + \text{N}(\text{CH}_3)_2(\tilde{\text{X}}^2\text{B}_1)$ is open. In the two

CH₃ velocity components, the faster one was regarded as the CH₃ product that had the N(CH₃)₂(\tilde{X}^2B_1) counter product. The E_{avl} -dependence of the branching ratio indicated a considerable contribution of the internal excitations to the non-adiabatic transition probability. We found a combination tendency between the vibrational excited CH₃ and electronically unexcited N(CH₃)₂. Although the electronic structure calculations of TMA are not fully available, we conjecture the pyramidal CH₃ geometry at the exit conical intersection based on the intensively investigated NH₃ photochemistry.

4.6 References

- 1 E. Kassab and E. M. Evleth, *The Rydberg Photophysics and Photochemistry of Amines. in The Role of Rydberg States in Spectroscopy and Photochemistry: Low and High Rydberg States*, edited by C. Sándorfy (Springer, Dordrecht, 1999), Vol. 20, p. 231.
- 2 M. N. R. Ashfold, G. A. King, D. Murdock, M. G. D. Nix, T. A. A. Oliver and A. G. Sage, *Phys. Chem. Chem. Phys.* **12**, 1218 (2010).
- 3 J. Biesner, L. Schnieder, J. Schmeer, G. Ahlers, X. Xie, K. H. Welge, M. N. R. Ashfold and R. N. Dixon, *J. Chem. Phys.* **88**, 3607 (1988).
- 4 J. Biesner, L. Schnieder, G. Ahlers, X. Xie, K. H. Welge, M. N. R. Ashfold and R. N. Dixon, *J. Chem. Phys.* **91**, 2901 (1989).
- 5 J. D. Rodríguez, M. G. González, L. Rubio-Lago and L. Bañares, *Phys. Chem. Chem. Phys.* **16**, 406 (2014).
- 6 J. Ma, C. Xie, X. Zhu, D. R. Yarkony, D. Xie and H. Guo, *J. Phys. Chem. A* **118**, 11926 (2014).
- 7 M. I. McCarthy, P. Rosmus, H.-J. Werner, P. Botschwina and V. Vaida, *J. Chem. Phys.* **86**, 6693 (1987).
- 8 M. N. R. Ashfold, C. L. Bennett and R. N. Dixon, *Chem. Phys.* **93**, 293 (1985).
- 9 M. N. R. Ashfold, R. Dixon, M. Kono, D. Mordaunt and C. Reed, *Philos. Trans. R. Soc. London, Ser. A* **355**, 1659 (1997).
- 10 D.-S. Ahn, J. Lee, J.-M. Choi, K.-S. Lee, S. J. Baek, K. Lee, K.-K. Baek and S. K. Kim, *J. Chem. Phys.* **128**, 224305 (2008).
- 11 D.-S. Ahn, J. Lee, Y. C. Park, Y. S. Lee and S. K. Kim, *J. Chem. Phys.* **136**, 024306 (2012).
- 12 M. H. Park, K.-W. Choi, S. Choi, S. K. Kim and Y. S. Choi, *J. Chem. Phys.* **125**, 084311 (2006).
- 13 S. J. Baek, K.-W. Choi, Y. S. Choi and S. K. Kim, *J. Chem. Phys.* **117**, 10057 (2002).
- 14 J. O. Thomas, K. E. Lower and C. Murray, *J. Phys. Chem. A* **118**, 9844 (2014).
- 15 J. O. Thomas, K. Lower and C. Murray, *J. Phys. Chem. Lett.* **3**, 1341 (2012).
- 16 G. C. G. Waschewsky, D. C. Kitchen, P. W. Browning and L. J. Butler, *J. Phys. Chem.* **99**, 2635 (1995).
- 17 C. L. Reed, M. Kono and M. N. R. Ashfold, *J. Chem. Soc., Faraday Trans.* **92**, 4897 (1996).
- 18 K. M. Dunn and K. Morokuma, *J. Phys. Chem.* **100**, 123 (1996).
- 19 H. Xiao, S. Maeda and K. Morokuma, *J. Phys. Chem. A* **117**, 5757 (2013).
- 20 M. Epshtein, A. Portnov and I. Bar, *Phys. Chem. Chem. Phys.* **17**, 19607 (2015).
- 21 R. Marom, T. Weiss, S. Rosenwaks and I. Bar, *J. Chem. Phys.* **132**, 244310 (2010).
- 22 Y. Onitsuka, K. Yamasaki, H. Goto and H. Kohguchi, *J. Phys. Chem. A* **120**, 8584 (2016).
- 23 C. G. Cureton, K. Hara, D. V. O'Connor and D. Phillips, *Chem. Phys.* **63**, 31 (1981).
- 24 A. M. Halpern, M. J. Ondrechen and L. D. Ziegler, *J. Am. Chem. Soc.* **108**, 3907 (1986).
- 25 K. Obi and Y. Matsumi, *Chem. Phys.* **49**, 95 (1980).
- 26 T. I. Sølling, C. Kötting and A. H. Zewail, *J. Phys. Chem. A* **107**, 10872 (2003).
- 27 Y. Zhang, H. Jónsson and P. M. Weber, *Phys. Chem. Chem. Phys.* **19**, 26403 (2017).

- 28 T. I. Sølling, T. S. Kuhlman, A. B. Stephansen, L. B. Klein and K. B. Møller, *ChemPhysChem* **15**, 249 (2014).
- 29 S. Deb, M. P. Minitti and P. M. Weber, *J. Chem. Phys.* **135**, 044319 (2011).
- 30 J. L. Gosselin, M. P. Minitti, F. M. Rudakov, T. I. Sølling and P. M. Weber, *J. Phys. Chem. A* **110**, 4251 (2006).
- 31 J. O. F. Thompson, L. B. Klein, T. I. Sølling, M. J. Paterson and D. Townsend, *Chem. Sci.* **7**, 1826 (2016).
- 32 J. D. Cardoza, F. M. Rudakov and P. M. Weber, *J. Phys. Chem. A* **112**, 10736 (2008).
- 33 L. B. Klein and T. I. Sølling, *Chem. Phys.* **442**, 62 (2014).
- 34 S. Deb, B. A. Bayes, M. P. Minitti and P. M. Weber, *J. Phys. Chem. A* **115**, 1804 (2011).
- 35 Y. Matsumi and K. Obi, *Chem. Phys.* **49**, 87 (1980).
- 36 E. Tannenbaum, E. M. Coffin and A. J. Harrison, *J. Chem. Phys.* **21**, 311 (1953).
- 37 A. M. Halpern and T. Gartman, *J. Am. Chem. Soc.* **96**, 1393 (1974).
- 38 M. Kawasaki, K. Kasatani, H. Sato, H. Shinohara, N. Nishi and T. Ibuki, *J. Chem. Phys.* **77**, 258 (1982).
- 39 N. R. Forde, M. L. Morton, S. L. Curry, S. J. Wrenn and L. J. Butler, *J. Chem. Phys.* **111**, 4558 (1999).
- 40 N. R. Forde, L. J. Butler, B. Ruscic, O. Sorkhabi, F. Qi and A. Suits, *J. Chem. Phys.* **113**, 3088 (2000).
- 41 N. R. Forde, L. J. Butler and S. A. Abrash, *J. Chem. Phys.* **110**, 8954 (1999).
- 42 P. Avouris and A. R. Rossi, *J. Phys. Chem.* **85**, 2340 (1981).
- 43 D. P. Taylor, C. F. Dion and E. R. Bernstein, *J. Chem. Phys.* **106**, 3512 (1997).
- 44 J. D. Cardoza and P. M. Weber, *J. Chem. Phys.* **127**, 036101 (2007).
- 45 R. O. Loo, H.-P. Haerri, G. E. Hall and P. L. Houston, *J. Chem. Phys.* **90**, 4222 (1989).
- 46 NIST, Data taken from <https://webbook.nist.gov/chemistry>.
- 47 M. J. Frisch, G. W. Trucks, H. B. Schlegel, G. E. Scuseria, M. A. Robb, J. R. Cheeseman, G. Scalmani, V. Barone, G. A. Petersson, H. Nakatsuji, X. Li, M. Caricato, A. Marenich, J. Bloino, B. G. Janesko, R. Gomperts, B. Mennucci, H. P. Hratchian, J. V. Ortiz, A. F. Izmaylov, J. L. Sonnenberg, D. Williams-Young, F. Ding, F. Lipparini, F. Egidi, J. Goings, B. Peng, A. Petrone, T. Henderson, D. Ranasinghe, V. G. Zakrzewski, J. Gao, N. Rega, G. Zheng, W. Liang, M. Hada, M. Ehara, K. Toyota, R. Fukuda, J. Hasegawa, M. Ishida, T. Nakajima, Y. Honda, O. Kitao, H. Nakai, T. Vreven, K. Throssell, J. A. Montgomery, Jr., J. E. Peralta, F. Ogliaro, M. Bearpark, J. J. Heyd, E. Brothers, K. N. Kudin, V. N. Staroverov, T. Keith, R. Kobayashi, J. Normand, K. Raghavachari, A. Rendell, J. C. Burant, S. S. Iyengar, J. Tomasi, M. Cossi, J. M. Millam, M. Klene, C. Adamo, R. Cammi, J. W. Ochterski, R. L. Martin, K. Morokuma, O. Farkas, J. B. Foresman, and D. J. Fox, GAUSSIAN 03, Revision D.01, Gaussian, Inc., Wallingford CT, 2016.

Chapter 5

General Conclusion

In this thesis, we have revealed the photodissociation dynamics of methylamine (CH_3NH_2) and trimethylamine ($\text{N}(\text{CH}_3)_3$, TMA) on the basis of ammonia photochemistry where a reaction barrier and a conical intersection play important roles. In Chapter 2, we explained experimental principles and methods for the pump-probe experiment under the condition controlling the reactant and product states. In Chapter 3, we identified the electronic state of the NH_2 product in the photodissociation of CH_3NH_2 with ion-imaging and dispersed fluorescence spectroscopy. The N–C bond fission of CH_3NH_2 photoexcited to the S_1 state proceeds on the S_0 surface after the $S_1 \rightarrow S_0$ internal conversion in which a conical intersection along the N–H bond cleavage coordinate acts as a funnel, resulting in the $\text{CH}_3(v=0) + \text{NH}_2(\tilde{\text{A}}^2\text{A}_1)$ and $\text{CH}_3(v_3=0-3) + \text{NH}_2(\tilde{\text{X}}^2\text{B}_1)$ pathways via the non-adiabatic transition in the vicinity of another conical intersection along the N–C bond dissociation direction. In Chapter 4, we investigated the energy dependence of the photodissociation dynamics of TMA over the S_2 and S_1 excited states. The dissociation threshold of the N–C bond rupture was found at $42,500 \text{ cm}^{-1}$, which is located between the S_1 and S_2 origins, and a switching from a fluorescent nature to a dissociative nature at the threshold was observed. The N–C bond dissociation generates the CH_3 radicals with slow and fast recoil-velocity which were ascribed to branching to the $\text{CH}_3 + \text{N}(\text{CH}_3)_2(\tilde{\text{A}}^2\text{A}_1)$ and $\text{CH}_3 + \text{N}(\text{CH}_3)_2(\tilde{\text{X}}^2\text{B}_1)$ pathways, respectively. The measured results suggested the pyramidal geometry for the CH_3 moiety at the exit conical intersection. The planarity of both NH_3 -frame and CH_3 moiety influences the non-adiabatic transition probability.

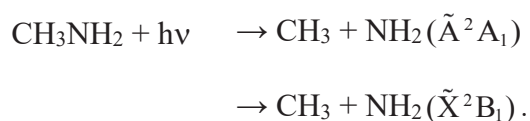
As mentioned in Chapter 1, amines are essential molecules in the organic and biological chemistry; therefore, the photodissociation dynamics of CH_3NH_2 and TMA discussed in this thesis will be useful for understanding the photochemistry of larger amines such as neurotransmitters. In addition, the experimental knowledge established in the present study will significantly contribute to further development of theoretical studies for reaction dynamics.

Appendix

Development of LIF Detection System

A.1 Introduction

In photodissociation of polyatomic molecules, the energy disposal and the state distribution of the nascent all products retain information for the dissociation dynamics. The energy disposal can be measured by state-resolved ion-imaging technique on the basis of the energy conservation law as explained in Chapter 2 and employed in Chapters 3 and 4. The state distributions of products are associated with the product nuclear motions such as stretching and bending motions; therefore, the measurements of the final state distributions of the all dissociation products are desirable for understanding the photodissociation mechanism. In the photodissociation of CH_3NH_2 , the nascent state-distribution of the CH_3 fragment and the preferential population in the $K_a = 0$ state of $\text{NH}_2(\tilde{\text{A}}^2\text{A}_1)$ were revealed, respectively, with resonantly enhanced multiphoton ionization (REMPI) spectroscopy and emission spectroscopy. These results indicated the branching of the product pathways on the S_0 surface as discussed in Chapter 3:



The branching of the product pathways is caused by the non-adiabatic dynamics around an exit conical intersection along the N–C bond dissociation coordinate. The adiabatic dissociative-trajectory to the $\text{CH}_3 + \text{NH}_2(\tilde{\text{X}}^2\text{B}_1)$ products may proceed far from the crossing point of the conical intersection on the S_0 surface. Determination of the final state-distribution of the $\text{NH}_2(\tilde{\text{X}}^2\text{B}_1)$ product is required for further identification of the N–C

bond fission dynamics. NH_2 radicals are unsuitable for ionization detection such as REMPI scheme. Laser-induced fluorescence (LIF) spectroscopy which is complementary method with REMPI spectroscopy is widely applied to detection of the $\text{NH}_2(\tilde{X}^2\text{B}_1)$ radicals.¹⁻⁶

Molecules and radicals of interest in the excited electronic state prepared with laser excitation emit spontaneously photons as fluorescence, and then relax to the ground electronic state. In LIF measurement, the fluorescence signal is detected with a photon detector such as a photomultiplier tube (PMT). The schematic diagram for LIF spectroscopy is illustrated in Figure A.1. A LIF excitation spectrum is obtained by recording the total fluorescence signal as a function of the excitation laser wavelength. A spectral line arises when the molecule in the lower state is excited resonantly to the upper state; therefore, the LIF spectrum of the nascent NH_2 fragment in the $\tilde{X}^2\text{B}_1$ state is linked to the final state distribution.

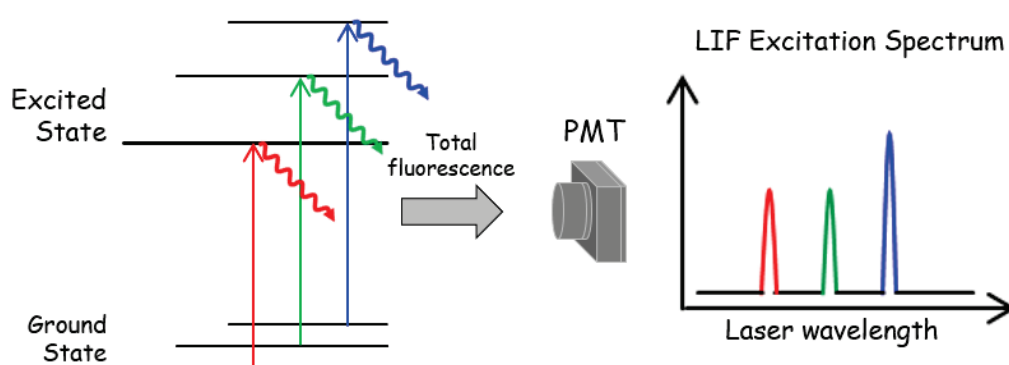


Figure A.1 Schematic diagram for the basic concept of LIF measurement. Molecules in the ground state are excited resonantly to the excited state by laser radiation, and the emitted fluorescence is monitored by a PMT with respect to the excitation laser wavelength.

One needs to carry out the experiment under the collision-free condition for measurements of the product state-distributions because a collision of the products causes the rotational and vibrational relaxations which smear the nascent state distributions of interest. The collision-free condition is generally achieved by maintaining a very low background pressure inside the experimental apparatus (e.g. a molecular beam experiment), so-called *spatial isolation*, since the mean free path of the particles is inversely proportional to the pressure. The LIF detection of nascent products in photodissociation under the molecular beam condition is suitable, but difficult due to low number density of the products and much lower detection efficiency of LIF spectroscopy than REMPI spectroscopy. The collision-free condition is also satisfied by *temporal isolation* where one ensures that the mean time between collisions is longer than the time required to make a measurement. Namely, products with the nascent state distribution are detected prior to collisions. The mean time is also inversely proportional to the pressure; therefore, we designated the reaction cell, whose inner pressure is adjustable, combined with pump-probe experimental technique which controls the time between the photolysis and probing.

Here, we explain roughly the relation of the pressure and the mean time between collisions. When a particle (atom or molecule), whose diameter is d , moves as illustrated in Figure A.2, the cross section (σ) for collision can be expressed by

$$\sigma = \pi d^2. \tag{A.1}$$

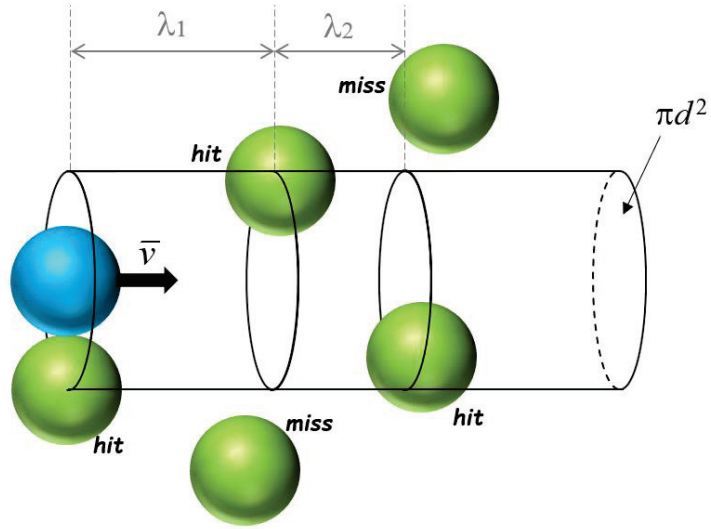


Figure A.2 Simple collision model. Only one particle (blue) moves with the average velocity \bar{v} , while the other molecules are frozen. The diameter of particles is d , and then the cross section for collision is πd^2 . The distance from i th collision to $(i + 1)$ th collision is λ_i .

To describe the average collision, the mean free path (λ) is defined by averaging a distance between collision (λ_i); therefore, the volume of a collisional cylinder, V , in Figure A.2 is

$$V = \sigma\lambda = \pi d^2\lambda. \quad (\text{A.2})$$

Namely, there is one atom in the volume, V ; therefore, the number density of the particle, ρ , is derived:

$$\rho = \frac{N}{V} = \frac{1}{\pi d^2\lambda}. \quad (\text{A.3})$$

On the other hand, the number density is also given from an ideal gas equation of state ($PV = N_A k_B T$):

$$\rho = \frac{N_A}{V} = \frac{P}{k_B T} \quad (\text{A.4})$$

where P and T denote the pressure and temperature, respectively. N_A is the Avogadro constant, and k_B is the Boltzmann constant. From Eqs. (A.3) and (A.4), we obtained the relation between the mean free path and pressure:

$$\lambda = \frac{k_B T}{\pi d^2 P}. \quad (\text{A.5})$$

If all particles, except one which is moving with the average velocity (\bar{v}), is frozen, the mean free path can be written by using the number of collisions (n) in a given time (Δt):

$$\lambda = \frac{\bar{v} \Delta t}{n} = \frac{\bar{v}}{z} \quad (\text{A.6})$$

where z is the collisional frequency ($z = n/\Delta t$) whose unit is s^{-1} . Assuming that the velocity distribution of the moving particle is a Boltzmann distribution, the averaged velocity (\bar{v}) is given as follows:

$$\bar{v} = \sqrt{\frac{8k_B T}{\pi m}} \quad (\text{A.7})$$

in which m is a mass of the atom. By substituting Eqs. (A.5) and (A.7) into Eq. (A.6),

$$\begin{aligned} \frac{k_B T}{\pi d^2 P} &= \sqrt{\frac{8k_B T}{\pi m}} \times \frac{1}{z} \\ z &= d^2 P \sqrt{\frac{8\pi}{mk_B T}} \end{aligned} \quad (\text{A.8})$$

is obtained. The mean time between collisions (τ_{col}) is

$$\tau_{\text{col}} = \frac{1}{z} = \frac{1}{d^2 P} \sqrt{\frac{mk_B T}{8\pi}}. \quad (\text{A.9})$$

The relation between the mean time (τ_{col}) and the pressure (P) for N_2 molecule at 298 K, whose diameter is approximately 4 \AA , is plotted in Figure A.3.

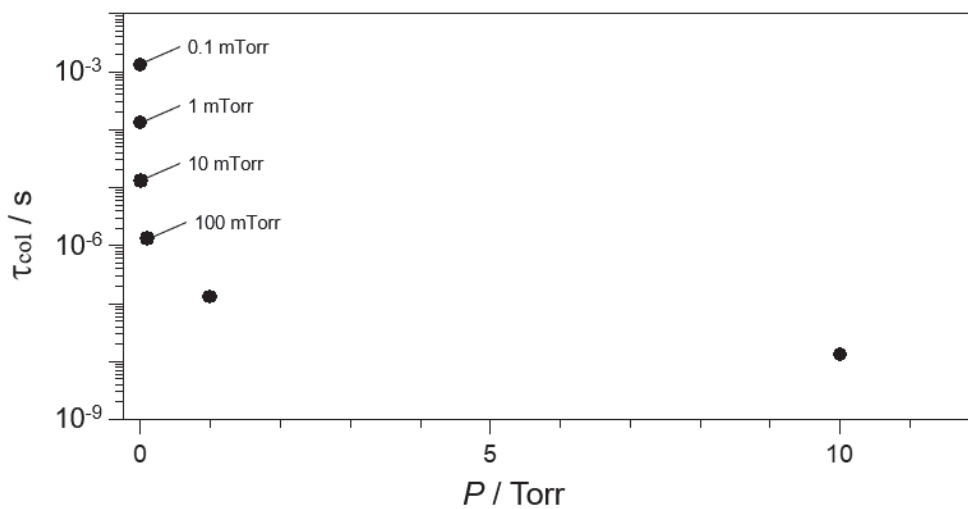


Figure A.3 Dependence of the mean time (τ_{col}) between collisions on the pressure (P). The values of τ_{col} were evaluated from Eq. (A.9) for N_2 molecule at room temperature (298 K), where the diameter of N_2 molecule was assumed to be 4 \AA .

A.2 Design of LIF Measurement Cell

The gas cell developed for the LIF detection of the nascent NH_2 fragments in the photodissociation of CH_3NH_2 is shown in Figure A.4: (a) 2D drawing in the XZ plane and (b) in the YZ plane, in which X, Y, and Z axes correspond to the directions of gas flowing, laser propagation, and detection axes, respectively. The chamber whose volume is approximately $5 \times 10^3 \text{ cm}^3$, was composed of three assemblies: a valve to adjust the inner pressure, pump, and a detector. The chamber was evacuated by either a turbomolecular pump (PTM 5150, Alcatel) or a rotary pump (Model-2010C, Alcatel). The chamber can be adapted for LIF measurement under the gas cell condition and also under the free jet condition; the turbo molecular pump evacuated the chamber at the background pressure of 10^{-7} Torr order for the free jet experiment, while the rotary pump evacuated at 10^{-4} Torr order for the gas cell experiment. The pulsed valve (General valve series 9, Parker Hannifin Corporation) operated by a pulse valve driver (IOTA ONE, Parker Hannifin Corporation) was mounted in the chamber. During valve operation, the pressure of the chamber was monitored by a pressure gauge (WIT-G1, ULVAC or 122AA, MKS Baratron). The unfocused pump and probe laser beams, which were aligned in the counter-propagating direction, irradiated molecules of interest at a 24 mm distance from the valve. Fluorescence from fragments photoexcited by the probe laser beam was focused on a photoelectric surface of a photomultiplier tube (PMT, R374, Hamamatsu) by a quartz lens ($f = 40 \text{ mm}$). Optical filters were used to reduce scattered light signal as required.

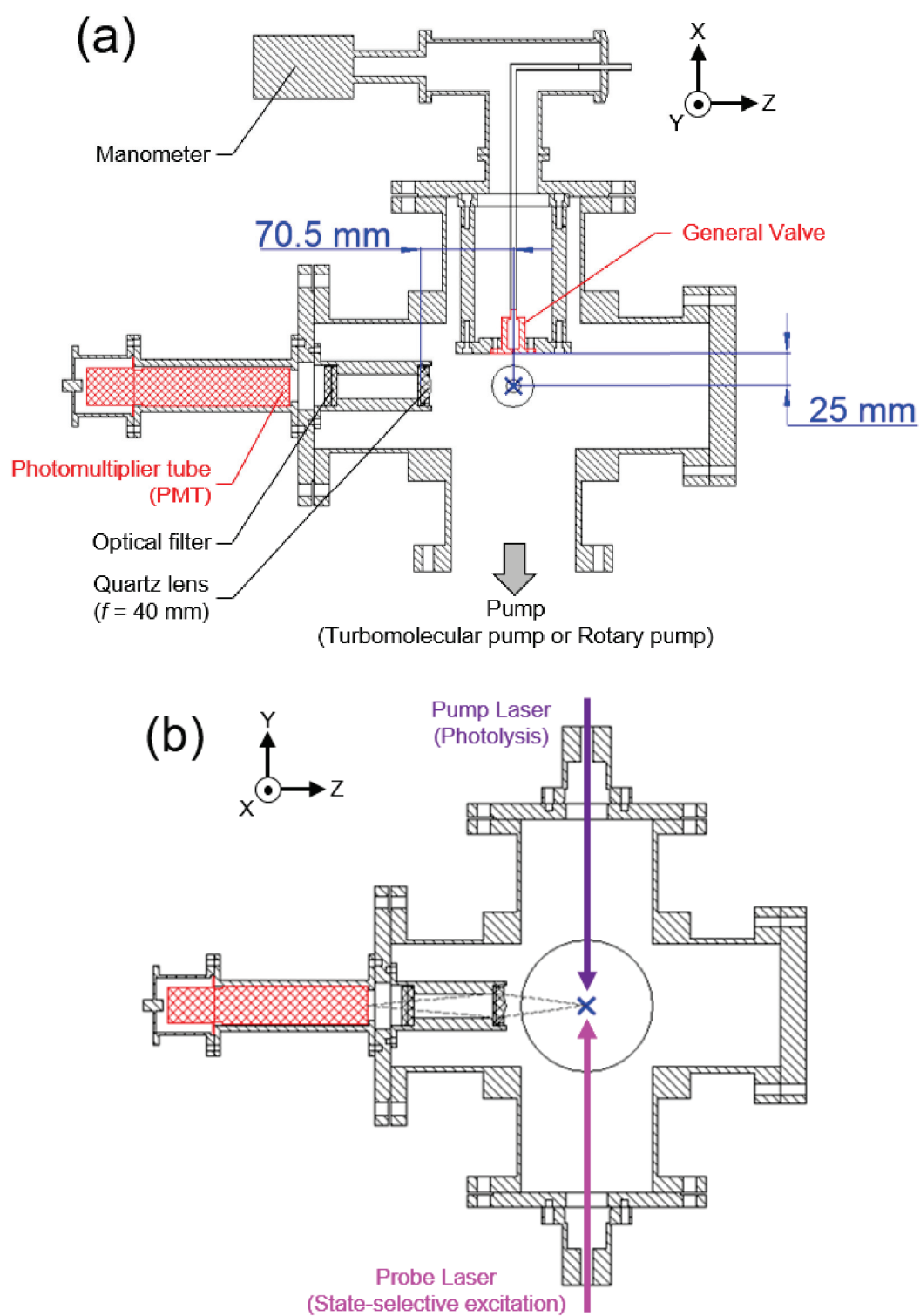


Figure A.4 2D drawing of the LIF chamber: (a) in XY plane and (b) in YZ plane. Blue cross marks denote the intersection position of pump and probe laser beams.

A.3 Performance Evaluation

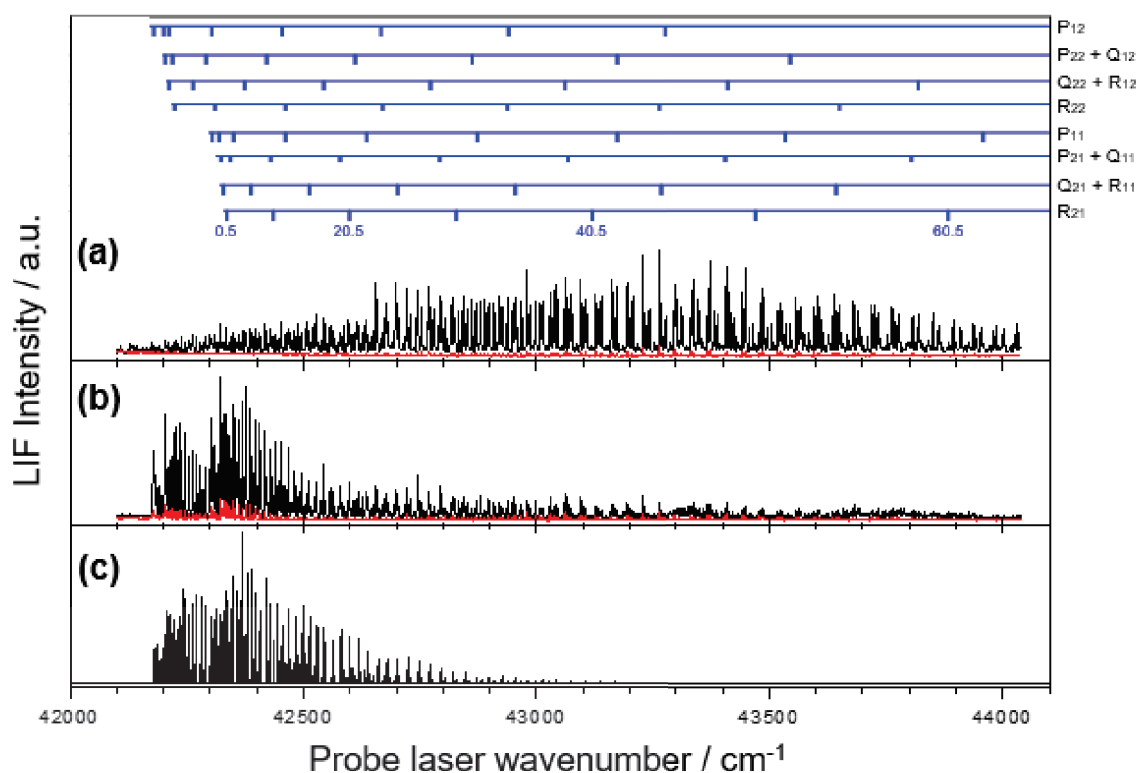


Figure A.5 LIF spectra of the NO ($\nu = 1$) fragment generated in the photodissociation of CH₃ONO measured at various total pressure, P_{total} : (a) $P_{\text{total}} = 100$ mTorr and (b) 5 Torr. Black lines correspond to two color (pump-probe) signal, while red ones are probe one-color spectrum. For comparison, (c) the simulated spectrum assumed the Boltzmann distribution with a rotational temperature of 1000 K is also shown.

A performance evaluation for the LIF detection of the nascent photofragments was carried out for the photodissociation of methyl nitrite (CH₃ONO). The photodissociation of CH₃ONO following the $S_2 - S_0$ excitation at 213 nm generates NO ($\nu = 0-3$) fragments with inverted rotational state-distribution.⁷ The LIF spectrum of NO ($\nu = 1$) photofragment was observed under the gas cell condition (298 K) and the free jet condition. Figure A.5 shows the LIF spectra under the gas cell condition at total inner pressure of (a) 100 mTorr and (b)

5 Torr. A gas mixture containing 10 % of CH₃ONO in He carrier gas was used. The delay time of the pump and probe laser pulses was 600 ns, and the pulse energy of the pump and probe lasers was 800 μJ/pulse and ~30 μJ/pulse, respectively. One-color spectra, in which the photodissociation of CH₃ONO and the photoexcitation of the nascent NO fragments occurs simultaneously in the same probe pulse, are also plotted by red lines. The simulation spectrum of NO ($v = 1$) assuming the Boltzmann distribution with a rotational temperature of 1000 K is shown in Figure A.5 (c) for comparison. The spectral appearance depended drastically on the inner pressure; the highly rotational-excited NO with inverted state-distribution was detected at lower pressure, while the statistical NO with Boltzmann type distribution was detected at 5 Torr. This difference arises from the collisional relaxation of the rotational state. In the laser delay time of 600 ns, the NO photoproduct is detected without collision at inner pressure of 100 mTorr where the mean time between collision is ~1 μs; therefore, the spectrum is identical with the REMPI spectrum⁷ measured under the collision free condition as displayed in Figure A.6. This result shows that the nascent state distribution in the photodissociation of CH₃ONO can be approximately observed at inner pressure of 100 mTorr without collisional relaxation. On the other hand, the LIF spectrum measured at 5 Torr results from the NO fragment with statistically rotational state-distribution after collisions due to the mean time of ~20 ns.

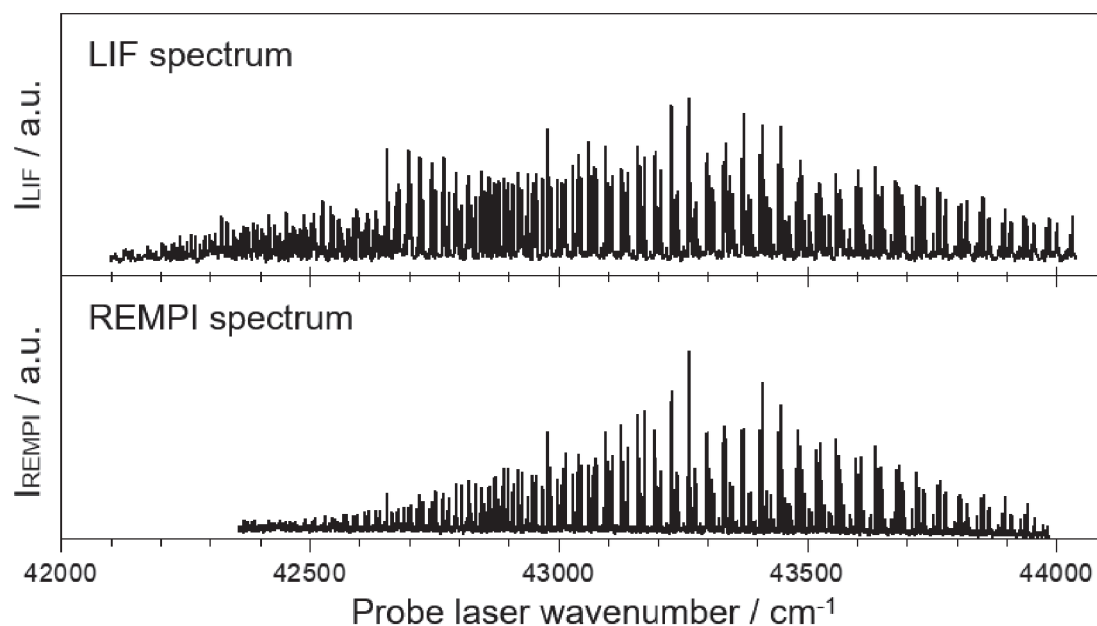


Figure A.6 LIF spectrum (100 mTorr) and REMPI spectrum of the nascent NO ($\nu = 1$) fragment generated in the photodissociation of CH_3ONO at the photolysis wavelength of 213 nm. LIF spectrum (upper) is measured at total pressure of 100 mTorr. REMPI one observed under the molecular beam experiment is taken from Ref. 7.

Figure A.7 shows the LIF spectrum of NO ($\nu = 1$) observed under the free jet condition, and one-color spectrum are shown by red line. In the free jet condition, the operations of the pulse valve, and the two laser (pump and probe) pulses were synchronously controlled by digital pulse generator with a repetition of 10 Hz. The pulse energies of the pump and probe laser beams were, respectively, 800 $\mu\text{J}/\text{pulse}$ and 70 $\mu\text{J}/\text{pulse}$, and the delay time between pump and probe laser pulses was 400 ns. During valve operation, the inner pressure was kept in order of 10^{-5} Torr. The state-distribution of the nascent NO fragment is significantly different from the REMPI spectrum measured by Sumida *et al.*⁷ (see Figure A.6 bottom); the NO photoproduct detected under the free jet condition populated also the low rotational

state around $42000\text{--}42400\text{ cm}^{-1}$. The LIF spectra of the NO ($\nu = 1$) fragment were observed at various timing of the valve operation with respect to the laser pulse timing; however, the no significant difference of the state-distribution was found. This result indicates the insufficient evacuation and/or the short distance between the valve and the reaction point at which CH_3ONO is irradiated by the pump and probe lasers for the photolysis and the detection, respectively. The separation of the source chamber and detection chamber with the differential evacuation and/or the extension of the distance between the valve and the reaction point are required for the measurement of the nascent state-distribution of photofragments under the free jet condition.

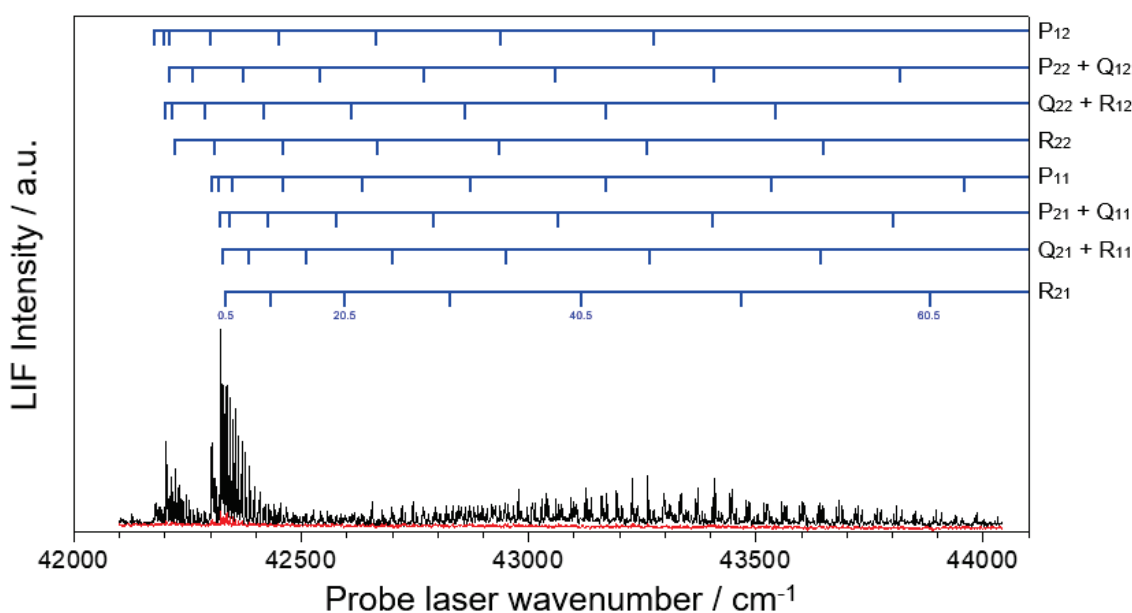


Figure A.7 LIF spectrum of the NO ($\nu = 1$) product in the photodissociation of CH_3ONO measured under the free jet condition. Black and red lines correspond to the two-color (pump-probe) and one-color (probe) spectra, respectively. The rotational state-distribution is widely spread out from the low J ($42200\text{--}42500\text{ cm}^{-1}$) and the high J ($42500\text{--}44000\text{ cm}^{-1}$) regions.

A.4 LIF Measurement in the CH₃NH₂ Photodissociation

The LIF chamber was applied to detection of the NH₂(\tilde{X}^2B_1) product in the CH₃NH₂ photodissociation at 213 nm under the gas cell condition at various inner pressure. The nascent NH₂(\tilde{X}^2B_1) photoproduct would be generated in the highly excited rovibrational-state, which is expected from the imaging result as seen in Figure A.8. On the basis of the energetic consideration, the NH₂(\tilde{X}^2B_1) product at the photolysis wavelength of 213 nm can populate the highly vibrational excited-state up to $\nu_{1 \text{ or } 3} = 5$ or $\nu_2 = 11$, where the ν_1 and ν_3 modes correspond, respectively, to the totally symmetric NH stretch vibration (3219.4 cm⁻¹) and the asymmetric NH stretch one (3301.1 cm⁻¹), and the ν_2 mode is the bending vibration (1497.2 cm⁻¹). The probe laser wavelength was scanned in the visible region (580–650 nm) which covers the excitation of the NH₂(\tilde{X}^2B_1) in the entire rovibrational state.⁴ The observed spectrum shown in Figure A.9 displays the structureless broad feature; therefore, we cannot assign to any transitions of the NH₂ radical. Assuming that the signal arises from the NH₂ radicals, the broad spectrum may be caused by overlapping the fluorescence lines from the various rovibrational states in the \tilde{X}^2B_1 state. The state-selectively detection of the nascent NH₂(\tilde{X}^2B_1) products demands improvement of the LIF chamber toward the dispersed LIF measurement.

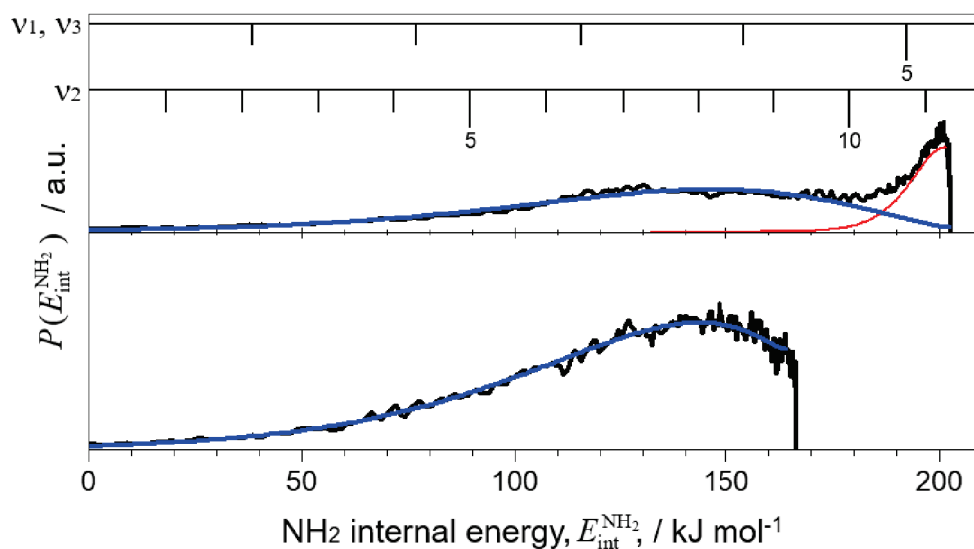


Figure A.8 Internal energy distributions for the nascent NH_2 counter-product of the CH_3 product in the $v = 0$ state (upper) and $v_3 = 1$ state (bottom) generated in the photodissociation of CH_3NH_2 at the photolysis wavelength of 213 nm. The internal energy distributions were obtained through the counter-product analysis of the imaging data, and the blue fitting curves correspond to the $\text{NH}_2(\tilde{X}^2\text{B}_1)$ photofragment. The energy positions of each vibrational mode (v_1 , v_2 , and v_3) are displayed.

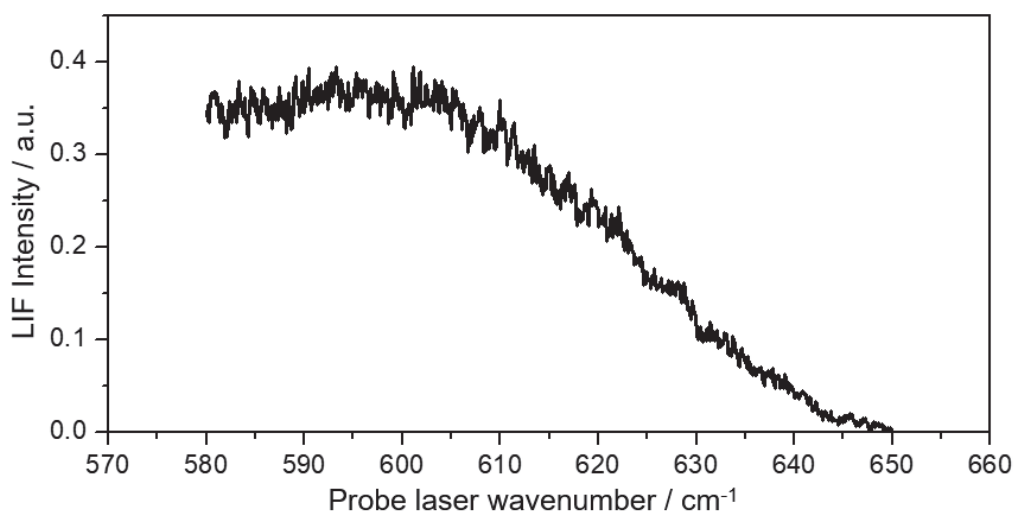


Figure A.9 Structureless LIF spectrum observed in the photodissociation of CH_3NH_2 at the photolysis wavelength of 213 nm. During the measurement, the probe laser power was monitored with a photodiode and was kept at $100 \mu\text{J}/\text{pulse}$.

The detection of the NH($a^1\Delta$) fragments generated in the CH_3NH_2 photodissociation at 213 nm was carried out under the gas cell condition. The pump and probe laser pulse energies were $800 \mu\text{J/p}$ and $0.6\text{--}1.2 \text{ mJ/pulse}$, respectively. The pump-probe delay time was 100 ns. During the measurements, the total pressure in the LIF chamber were kept at 500 mTorr where the mean time between collisions is ~ 200 ns. The observed spectrum for the NH ($a^1\Delta, v = 0$) is shown in Figure A.10. The spectral features were assigned to the $a^1\Delta, v = 0 \rightarrow c^1\Pi, v = 0$ transition of NH fragments based on literature source.⁸ The splitting of the peaks corresponding to high J'' is due to the Λ doubling of the $c^1\Pi$ state. The corresponding Λ doubling of the $a^1\Delta$ state⁸ is much too small to be resolved with our

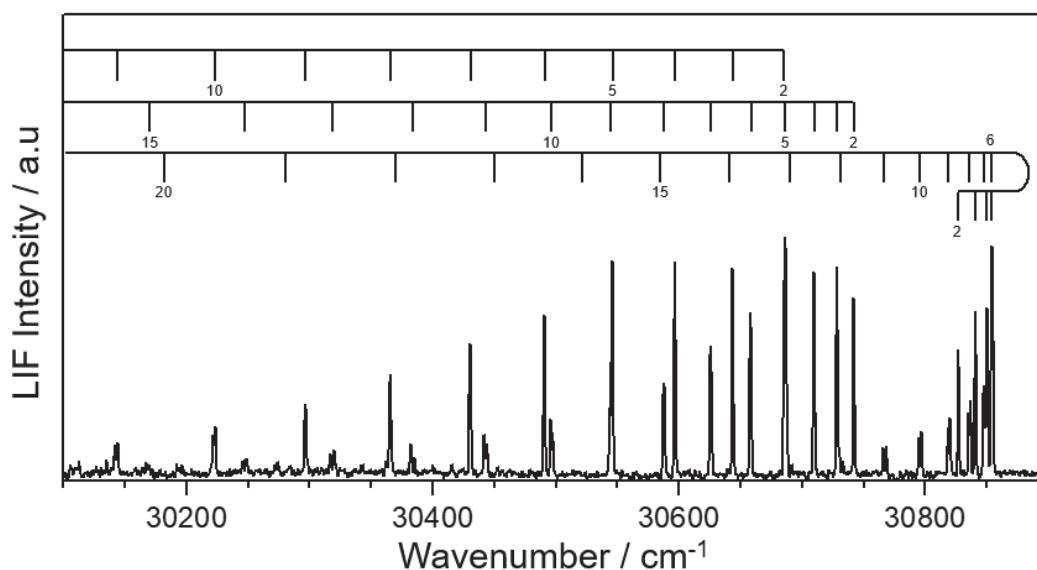


Figure A.10 LIF excitation spectrum for NH ($a^1\Delta, v = 0$) generated in the 213 nm photolysis of CH_3NH_2 at total inner-pressure of 500 mTorr. Emission detected on the $a^1\Delta, v = 0 \rightarrow c^1\Pi, v = 0$ transition of the NH fragments. Spectral assignments referred to Ref. 8. The apparent splitting of lines with $J'' \geq 7$ is due to Λ doubling in the upper $c^1\Pi$ state. The pulse energies of the pump and probe laser beams were $800 \mu\text{J/pulse}$ and 0.6 mJ/pulse , respectively.

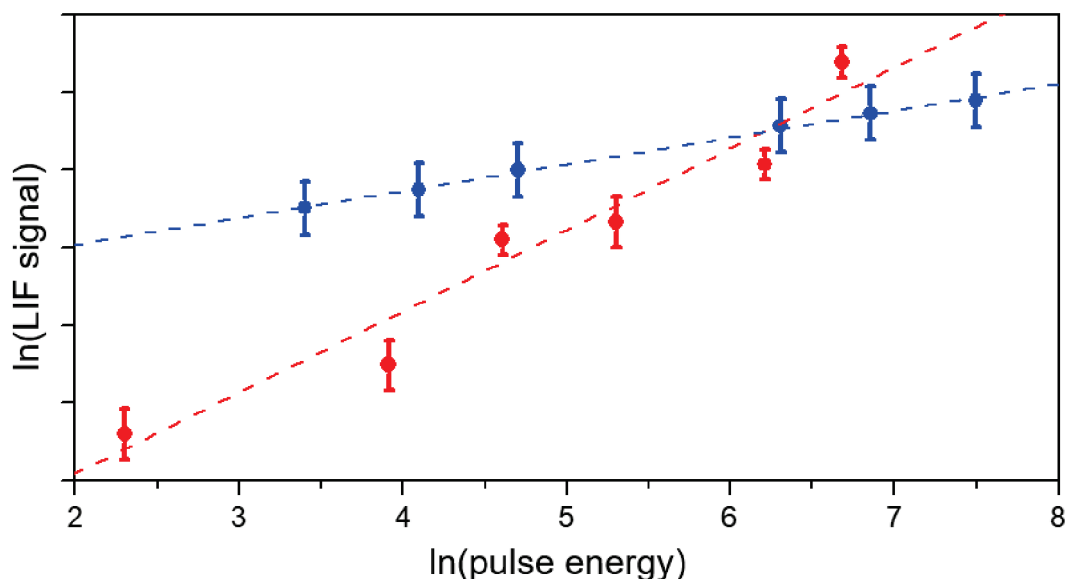


Figure A.11 LIF signal dependence on photolysis (red) and probe (blue) laser pulse energies; the gradients are 1.05 ± 0.14 and 0.34 ± 0.01 , respectively. The pulse energy was varied in the range of 10–800 $\mu\text{J}/\text{pulse}$ (photolysis) and 30–1800 $\mu\text{J}/\text{pulse}$ (probe).

apparatus. The signal of the vibrationally excited $\text{NH}(a^1\Delta)$ fragment was not observed. The LIF signal dependence on the pump and probe laser pulse energies are shown in Figure A.11, where the gradients were determined by the least-squares method. The LIF signal showed a clear linear dependence (1.05 ± 0.14) on the photolysis laser pulse energy. This dependency allows an exclusion of multi-photon photodissociation of CH_3NH_2 and secondary photodissociation of the nascent products by pump laser pulse. On the other hand, the gradient for the probe laser dependence (0.34 ± 0.01) was much small due to the quite large oscillator strength of the $a^1\Delta, v=0 \rightarrow c^1\Pi, v=0$ transition. In addition, since the $\text{NH}(a^1\Delta, v=0)$ fragment in the CH_3NH_2 photolysis was not observed in the ionization detection with REMPI spectroscopy as mentioned in Chapter 3, the possibilities for the secondary photodissociation of the NH_2 and/or CH_3NH photoproducts still remain.

A.5 Extension toward Dispersed LIF Measurement

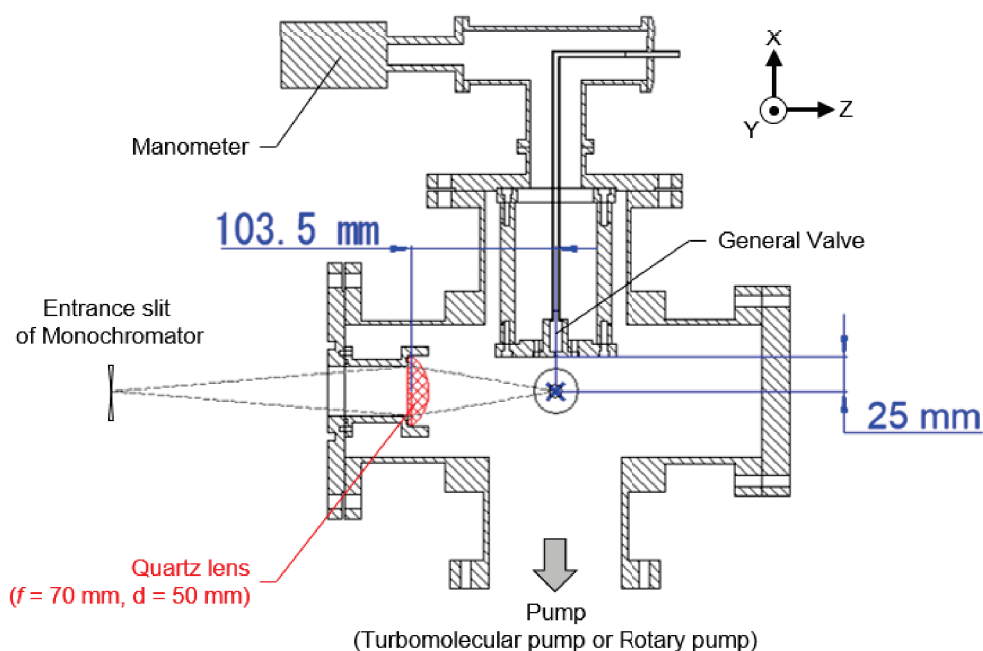


Figure A.12 2D drawing of the LIF chamber in XY plane. Blue cross marks denote the reaction point where molecule of interest is dissociated, and the nascent fragment is electronically excited for detection.

The setup for the dispersed LIF (DF) measurement was almost same as that for the LIF excitation measurement except the detector assembly. The 2D drawing in the XZ plane is shown in Figure A.12. A quartz lens ($f = 70$ mm) with a diameter of 50 mm was mounted at the distance of 103.5 mm from the reaction point. Emission from the reaction point was focused with the lens on the entrance slit of a grating monochromator ($f = 300$ mm, MC-30N with 75 grooves/mm blazed at 500 nm, Ritsu Oyo Kogaku Co. Ltd.). The emission dispersed by the grating was monitored as a function of the monochromator wavelength with a photomultiplier tube (931B, Hamamatsu). Generally, the signal intensity in the dispersed LIF measurement is much weaker than that in the LIF excitation spectrum, leading

to the photon-counting level in the limiting case. The design and development of the pulse-counting circuit are currently conducted.

A.6 References

1. S. V. Filseth, J. Danon, D. Feldmann, J. D. Campbell and K. H. Welge, *Chem. Phys. Lett.* **63**, 615 (1979).
2. G. S. Selwyn, G. T. Fujimoto and M. C. Lin, *J. Phys. Chem.* **86**, 760 (1982).
3. T. Wen, M. F. Golde, G. H. Ho and A. M. Moyle, *J. Chem. Phys.* **87**, 1045 (1987).
4. K. Yamasaki, A. Watanabe, T. Kakuda, A. Itakura, H. Fukushima, M. Endo, C. Maruyama and I. Tokue, *J. Phys. Chem. A* **106**, 7728 (2002).
5. K. Yamasaki, A. Watanabe, A. Tanaka, M. Sato and I. Tokue, *J. Phys. Chem. A* **106**, 6563 (2002).
6. C. Brackmann, B. Zhou, P. Samuelsson, V. A. Alekseev, A. A. Konnov, Z. S. Li and M. Aldén, *Spectrochi. Acta A* **184**, 235 (2017).
7. M. Sumida, S. Masumoto, M. Kato, K. Yamasaki and H. Kohguchi, *Chem. Phys. Lett.* **674**, 58 (2017).
8. W. Ubachs, G. Meyer, J. J. TerMeulen and A. Dymanus, *J. Mol. Spectrosc.* **115**, 88 (1986).

公表論文

- (1) Detection of the Excited-State $\text{NH}_2(\tilde{\text{A}}^2\text{A}_1)$ in the Ultraviolet Photodissociation of Methylamine
Yuuki Onitsuka, Katsuyoshi Yamasaki, Hiroki Goto, Hiroshi Kohguchi
J. Phys. Chem. A **120**, 8584 (2016).

- (2) Energy dependence of photodissociation dynamics of trimethylamine over the S_2 and S_1 excited states
Yuuki Onitsuka, Yuki Kadowaki, Atsuya Tamakubo, Katsuyoshi Yamasaki, Hiroshi Kohguchi
Chem. Phys. Lett. **716**, 28 (2019).

参考論文

- (1) Multiple Intersystem Crossing Pathways in Cinnamate-Based UV-B Sunscreens

Kaoru Yamazaki, Yasunori Miyazaki, Yu Harabuchi, Tetsuya Taketsugu, Satoshi Maeda, Yoshiya Inokuchi, Shin-nosuke Kinoshita, Masataka Sumida, Yuuki Onitsuka, Hiroshi Kohguchi, Masahiro Ehara, Takayuki Ebata
J. Phys. Chem. Lett. **7**, 4001 (2016).

- (2) Different photoisomerization routes found in the structural isomers of hydroxy methylcinnamate

Shin-nosuke Kinoshita, Miyazaki, Masataka Sumida, Yuuki Onitsuka, Hiroshi Kohguchi, Yoshiya Inokuchi, Nobuyuki Akai, Takafumi Shiraogawa, Masahiro Ehara, Kaoru Yamazaki, Yu Harabuchi, Satoshi Maeda, Tetsuya Taketsugu, Takayuki Ebata
Phys. Chem. Chem. Phys. **20**, 17583 (2018).

